THE JOURNAL OF PHYSICAL CHEMISTRY A

pubs.acs.org/JPCA

Article

OH-Initiated Reactions of *para*-Coumaryl Alcohol Relevant to the Lignin Pyrolysis. Part II. Kinetic Analysis

Jason M. Hudzik, Mohamad Barekati-Goudarzi, Lavrent Khachatryan, Joseph W. Bozzelli, Eli Ruckenstein, and Rubik Asatryan*

Cite This: J. Phys. Chem. A 2020, 124, 4875−4904

Read Online

ACCESS | Metrics & More | Article Recommendations | Supporting Information

ABSTRACT: Monolignols are precursor units and primary products of lignin pyrolysis. The currently available global (lumped) and semidetailed kinetic models, however, are lacking the comprehensive decomposition kinetics of these key intermediates in order to advance toward the fundamentally based detailed chemical-kinetic models of biomass pyrolysis. *para*-Coumaryl alcohol (HOPh−CH═CH−CH_2OH, *p*-CMA) is the simplest of the three basic monolignols containing a typical side-chain double bond and both alkyl and phenolic type OH groups. The two other monomers additionally contain one and two methoxy groups, respectively, attached to the benzene ring. Previously, we developed a detailed fundamentally based mechanism for unimolecular decomposition of *p*-CMA (as well as its truncated allyl and cinnamyl alcohol models) and explored its reactivity toward H radicals generated during pyrolysis. The reactions of *p*-CMA with pyrolytic OH radicals is another set of key reactions particularly important for understanding the formation mechanisms of a wide variety of oxygenates in oxygen-deficit (anaerobic) conditions and the role of the lignin side groups in pyrolysis pathways. In Part I of the current study (*J. Phys. Chem. A*, **2019**, *123*, 2570−2585), we reported a detailed potential energy (enthalpy) surface analysis of the reaction OH + *p*-CMA with suggestions for a variety of chemically activated, unimolecular, and bimolecular reaction pathways. In Part II of our work, we provide a detailed kinetic analysis of the major reaction channels to evaluate their significance and possible impacts on product distributions. Temperature- and pressure-dependent rate constants are calculated using the quantum Rice−Ramsperger−Kassel method and the master equation analysis for falloff and stabilization. Enthalpies of formation, entropies, and heat capacities are calculated using density functional theory and higher-level composite methods for stable molecules, radicals, and transition-state species. A significant difference between well depths for the chemically activated adduct radicals, [*p*-CMA-OH]*, is found for the α- and β-carbon addition reactions to generate the 1,3- and 1,2-diol radicals, respectively. This is due to the synergistic effect from conjugation of the proximal radical center with the aromatic ring and the strong H-bonding interaction between vicinal OH groups in the β-adduct (1,2-diol radical). Both adducts undergo isomerization and low-energy transformations, however, with different kinetic efficiencies because of the difference in stabilization energies. Reaction pathways include dissociation, intramolecular abstraction, atom and group transfers, and elimination. Of particular interest is a roaming-like low-energy dehydration reaction to form O-centered intermediate radicals. The kinetic analysis demonstrated the feasible formation of various products detected in pyrolysis experiments, suggesting that the gas-phase reactions of OH radicals can be a key process to form major products and complex oxygenates during lignin pyrolysis. Our preliminary experiments involving pyrolysis of the vaporized monomers support this basic statement. A novel mechanism for the formation of benzofuran, identified in experimentation, is also provided based on the potential conversions of hydroxyphenylacetaldehyde and corresponding isomers, which are kinetically favored products.

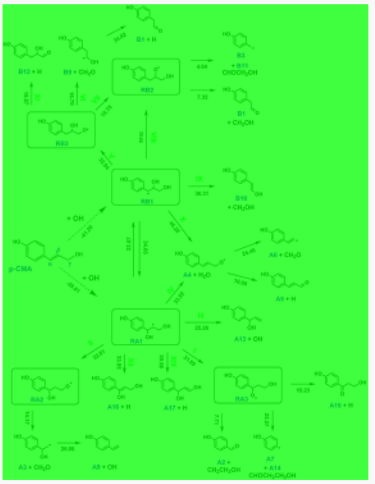

1. INTRODUCTION

Lignin, a major component of lignocellulose, is a highly cross-linked macromolecule produced by radical polymerization of three phenylpropanoid monomers (monolignols), the cinnamyl alcohol (CnA) derivatives (Figure 1): *p*-coumaryl alcohol (*p*-CMA), coniferyl alcohol (CFA), and sinapyl alcohol (SPA).[1−3] These monolignols are connected through a complex network of ether and carbon−carbon bonds, primarily via β-O-4, α-O-4, 4-O-5, 5−5, and β−β linkages, as well as benzodioxocin and spirodionene units.[4−6] Depending on the origin of lignin macromolecules, three types of aromatic nuclei are distinguished to define various types of lignin: 4-hydroxyphenyl (H), syringyl (S, 3,5-dimethoxy-4-hydroxyphenyl), and guaiacyl (G,

Received: December 25, 2019
Revised: May 20, 2020
Published: May 20, 2020

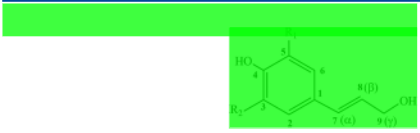

Figure 1. Structure of monolignols and abbreviations utilized in this analysis: *p*-CMA: $R_1 = R_2 = H$, CFA: $R_1 = H$, $R_2 = OCH_3$, SPA: $R_1 = R_2 = OCH_3$, CnA: no additional ring substituents, AA: no ring, side chain only.

4-hydroxy-3-methoxyphenyl) derived from the above monolignols. Although lignin comprises almost 30% of wood (by weight) and is an important resource of renewable fuels, precursor for high-value chemicals, and renewable feedstock for production of aromatic compounds, its robust and irregular structure poses many challenges for its utilization.[8−14]

Pyrolysis is a major depolymerization technique to process lignin. Two main classes of reactions are common to consider for lignin pyrolysis as a function of temperature: (a) primary processes, which typically occur between 200 and 350 °C to produce volatile compounds and char components and (b) secondary processes, involving a variety of isomerization/decomposition and bimolecular reactions. At temperatures above 400−450 °C, methoxy group-related reactions are emerging, where catechols are formed at 550−600 °C (perhaps, mostly from G- and S-lignins bearing both phenolic hydroxyl and methoxy groups), accompanied by increased gasification (formation of noncondensable gases such as CO and CO_2).[13,16] At elevated temperatures above 700 °C, various conjugated polycyclic aromatic hydrocarbons are generated with most phenols and *o*-cresols still being stable.

Monolignols are the most important primary products of lignin pyrolysis.[2,14,15,17−20] Their primary formation and decomposition are currently the dominating view on the decomposition mechanisms and depolymerization of lignin during fast pyrolysis.[9,15,18−33] This makes the pyrolysis of monolignols a very challenging process to be studied kinetically. A fundamentally based pyrolysis mechanism of these key intermediates is necessary to develop detailed kinetic models of lignin pyrolysis so as to accomprehend the kinetic models of biomass pyrolysis because the pyrolysis kinetics of other two biomass components, viz., cellulose and hemicellulose is much more developed (see, e.g., refs 34−36).

There are several kinetic models in the literature for lignin depolymerization, primarily involving empirical lumped-reaction schemes and rate estimation rules, as well as a few semidetailed kinetic models incorporating fundamentally based submechanisms.[2,37−43] To the best of our knowledge, there is no first-principle-methods-based kinetic model for lignin pyrolysis, as opposed to the simpler cellulose and hemicellulose models, not to mention the highly developed kinetic models for traditional fuel components.

Detailed kinetic models for substituted phenols seem to be the most relevant submodels for lignin pyrolysis.[6] For instance, the recent model by Ranzi and co-workers[42] includes various phenols substituted by methyl, methoxy, and aldehyde groups—the anisole, catechol, benzaldehyde, guaiacol, salicylaldehyde, and the largest one—vanillin containing both methoxy and aldehydic groups. Note that primarily considered sets of products formed at temperatures near 600 °C did not include more intricate low temperature intermediates—oxygenates. On the other hand, the addition of monolignols, containing a large reactive side chain attached to the phenol moiety, to this list, advocated by Norinaga and co-workers,[24,41] is an important step toward the development of a fundamentally based kinetic model of biomass. These partial improvements already included some of the recently emerged fundamental mechanistic results on pyrolysis of monolignols and low-energy pathways.

The prevailing formation of monolignols during primary pyrolysis is also validated by the similarity of the pyrolysis products from hardwood lignin at 200−350 °C with those from the pyrolysis of G- and H-monomers (here, CFA and SPA derived from the G-lignin and S-lignin, respectively).[15,18−20] However, the detection of these compounds is not straightforward because they undergo secondary transformations or repolymerize to contribute to the char formation. Other researchers also suggested the initial formation of monomers. Earlier, Evans et al.[44] have found that the *para*-coumaryl alcohols (along with vinyl phenol) are the most abundant volatile products of herbaceous biomass.

An alternative hypothesis[22,45] considers a thermal ejection mechanism for the lignin pyrolysis and suggests the formation of the liquid intermediate phase at the early stage of lignin pyrolysis and subsequent vaporization of the oligomeric compounds as aerosols, known as "pyrolytic lignin" (thus oligomers might be considered to be primary pyrolysis products). Based on the high dissociation energies of the lignin structural units (even the weakest C−O etheric interunit bonds) and in support of the primary formation of monomers during pyrolysis, Yang et al.[29] suggested that the formation of aromatic compounds during pyrolysis primarily occurs from light hydrocarbons, rather than directly from original aromatic lignin structures.

To additionally verify our calculation results involving also chemically activated processes, which typically occur in gas-phase conditions, with no solid-phase or solvent effects included, we have started a series of experiments where the monolignol reagent is in vaporized conditions. The preliminary results are generally consistent with previous conventional and fractional pyrolysis data quoted here, refs 21 and 23.

Primary pyrolysis of lignin (typically from 200 to 400 °C) produces characteristic low-molecular mass compounds, mostly phenolics.[11,13,15−17,37,46−56] Aromatic compounds produced during the primary pyrolysis of G-lignins, for instance, are predominantly 4-substituted guaiacols (2-methoxy phenols), whereas S-lignins are represented by syringol (2,6-dimethoxiphenol) derivatives.[11,13,15−17,37,46−56] The primary pyrolysis reactions, mainly studied on dimer models, are believed to occur via homolytic bond cleavage processes followed by secondary radical reactions, as well as concerted decomposition pathways such as Maccoll and retroene pericyclic intramolecular-type rearrangements.[9,13,21−23,57−66] Other alternative routes have not been ruled out, such as the one noted by Elder and Beste[50] for dimer models containing aliphatic γ-OH groups (see also a series of works by Kawamoto reviewed in ref 15). Further complications of decomposition patterns and product distributions arise from the highly reactive side groups.[15,16,18,21−23]

The propanoid side groups of the monolignols' allyl alcohol (AA) moiety ($-CH{=}CHCH_2OH$), combined with phenolic OH and variably present methoxy groups, are also common features in lignin end groups typically accounting for diversity of the pyrolysis products. Hence, a detailed exploration of the pyrolysis reactions of monomers, their thermochemical properties, including the stability of intermediate species, and detailed chemical kinetics is important to provide mechanistic insights

https://dx.doi.org/10.1021/acs.jpca.9b11894
J. Phys. Chem. A 2020, 124, 4875−4904

into lignin depolymerization and valorization. There is also a recondensation (repolymerization) tendency, often to form diverse species with novel functionalities, which further diversifies the role of the side groups in lignin pyrolysis.[8,14,16,52]

The characteristic features of *para*-coumaryl alcohol (*p*-CMA, Figure 1) also allow it to serve as a relevant model for biologically important unsaturated alcohols involving aromatic groups and polyhydric moieties to generate a variety of oxygenates abundant in nature.

The typical light ("pool") radicals, H, OH, CH_3, and CH_3O, are believed to be largely generated during lignin pyrolysis to trigger chain reactions and to modify ("enrich" by hydrogen and oxygen) the intermediate products of the "hydrogen-lean" and "oxygen-deficit" side groups.

Our recent fundamentally based theoretical and low-temperature-matrix-isolation−electron paramagnetic resonance spectroscopy (LTMI-EPR) studies of various CnAs highlighted the role of propanoid side chain reactivity in diversity of pyrolysis products.[21−23,27] We also presented a network of the chemically activated H + *p*-CMA reactions to explain the formation of key products and regeneration of radical species in pyrolysis of *p*-CMA.[21] Because the highly reactive hydroxyl radicals generated during pyrolysis can also trigger a cascade of free-radical pathways, we developed a detailed potential energy (enthalpy) surface (PES) for the reactions of hydroxyl radicals with *p*-CMA in Part I of this study.[27] Various density functional theory (DFT) and *ab initio* protocols were employed with a focus on addition−elimination reactions of the side chain double bond in *p*-CMA, including isomerization through hydrogen atom shifts, dehydration, and formation of various open- and closed-shell products.

In this Part II of our study, we continue the exploration of the pyrolysis mechanisms of lignin models and provide a comprehensive kinetics analysis of the reactivity of *p*-CMA toward hydroxyl radicals, which can be a key issue in the formation and interconversions of oxygenated compounds during lignin pyrolysis—in anaerobic conditions. Our previous PES for the OH + *p*-CMA system has been expanded and updated with refined energies of stationary points at a higher CBS-QB3 level of theory.

The readers are referred to Part I of our study[27] (and preceding papers[21−23]) for a detailed overview and discussion of *p*-CMA reactivity and pyrolysis reactions, as well as the experimental and theoretical analysis of the pyrolysis of other relevant models, including widely studied dimers containing primarily *α*-O-4 and *β*-O-4 linkages (see also refs 13,16,19,20,31−33,37,49−51,55,57−79). A few important points are highlighted below.

1.1. Contracted Models. Detailed analyses of the reactivities of contracted lignin models, including *ortho*-quinone methide (QM),[32,72,80,81] anisole,[82] and catechol,[83−88] which are believed to be intermediates in lignin thermolysis and char formation, are available in the literature for comparisons. There are also a variety of studies on the reactions of OH radicals with simple alkenes and unsaturated model compounds such as C_2H_4,[89−91] acrolein (CH_2=CH−CHO),[92] enols (albeit more focused on further combustion reactions),[93,94] styrene,[95] aldehydes,[96−98] and unsaturated alcohols[96−100] to represent the side-chain double bond of the lignin and monolignols.

The most authentic model of the hydroxypropenyl side groups of monolignols is AA (CH_2=$CHCH_2OH$). The reaction of AA with OH radicals is well explored[101−103] particularly in our most recent theoretical study.[102] Various isomerization and unimolecular decomposition channels have also been studied by Zhang et al.[101] at the G3MP2 level of theory, involving the formation and decomposition of 1,3- and 1,2-diol radical adducts of the OH addition to the double-bonded carbon atoms of the substrate. Bond fissions of the radicals are found to be the most affordable reactions. Kinetic analysis revealed that the bimolecular H-abstraction reactions can prevail only at high temperatures, whereas the formation of the $CH_2^{\bullet}CH(OH)CH_2OH$ adduct (1,2-diol radical) from collisional stabilization is dominant at 200−400 K temperatures and atmospheric pressure.[101] That contrasts with the conclusions from Atkinson and co-workers,[104] who considered a bimolecular H-abstraction of *α*-hydrogen of AA by OH radicals to form water and *α*-hydroxyl radicals (analogous to the monolignol radical A4 presented in Figure 2) as an only pathway to generate the main product acrolein. Because no potential product formation channels were explored in ref 101, including dehydration of activated radical adducts, we further provided a detailed mechanistic analysis of this reaction (which also relates to the roaming phenomenon in chemically activated processes) and proposed a low-energy roaming dehydration mechanism for energized adducts, leading to key products.[102] Taking into consideration that bimolecular reaction channels dominate only at elevated temperatures, as noted above,[101] the roaming of OH radicals (reactions via roaming-like TS) in chemically activated diol radical intermediates[102] could be considered the only alternative to explain the low-energy formation of the main detected product acrolein observed by Atkinson et al.[104]

The functional groups of side chains, primarily hydroxyl groups, provide strong electronic and steric effects on the reactivity of lignin.[31,68,105,106] The effect of OH substituents at *α*- and *γ*-carbon positions (see Figure 1) of lignin model dimers has been particularly assigned to a stabilization via an initial hydrogen bonding.[106] In addition, the two isolated OH groups can be involved in low-energy dehydration reactions through roaming, as follows from Part I of this study.[27]

It is also known that the rate coefficients of the OH + unsaturated alcohol reactions are only weakly dependent on the chain length of the alcohol.[99] De Bruycker[100] reported a significant reactivity difference in the C=C double bond in the *β*- and *γ*-positions to the hydroxyl group for the pyrolysis and oxidation processes for the unsaturated prenol and *iso*-prenol alcohols. Prenol also represents a relevant model of lignols because it includes an extended AA moiety of the *p*-CMA, albeit with two H atoms of the C3-terminal position that are replaced by two CH_3 groups.

As noted above, the side-chain double bonds in monomers, intermediates, and the major products such as 4-vinylphenol can also account for the repolymerization processes, along with generated monomeric radicals[14,107] (Kawamoto particularly suggested a vinyl-condensation-type mechanism for repolymerization[107]).

Few studies have been completed on the polymerization of monolignols, unlike its dimerization. A transition-state structure for dimerization of *p*-CMA via the *p*-quinone methide intermediate has been proposed by Shigematsu et al.[32] The activation enthalpy of 9.8 kcal/mol, calculated at the semi-empirical PM5 level, appears to be close to the activation energies of radical polymerization of common vinyl polymers (7−8 kcal/mol for propagation of vinyl monomers for polystyrene[97]) as opposed to the activation energies for decomposition of common radical initiators, which are much

https://dx.doi.org/10.1021/acs.jpca.9b11894
J. Phys. Chem. A 2020, 124, 4875−4904

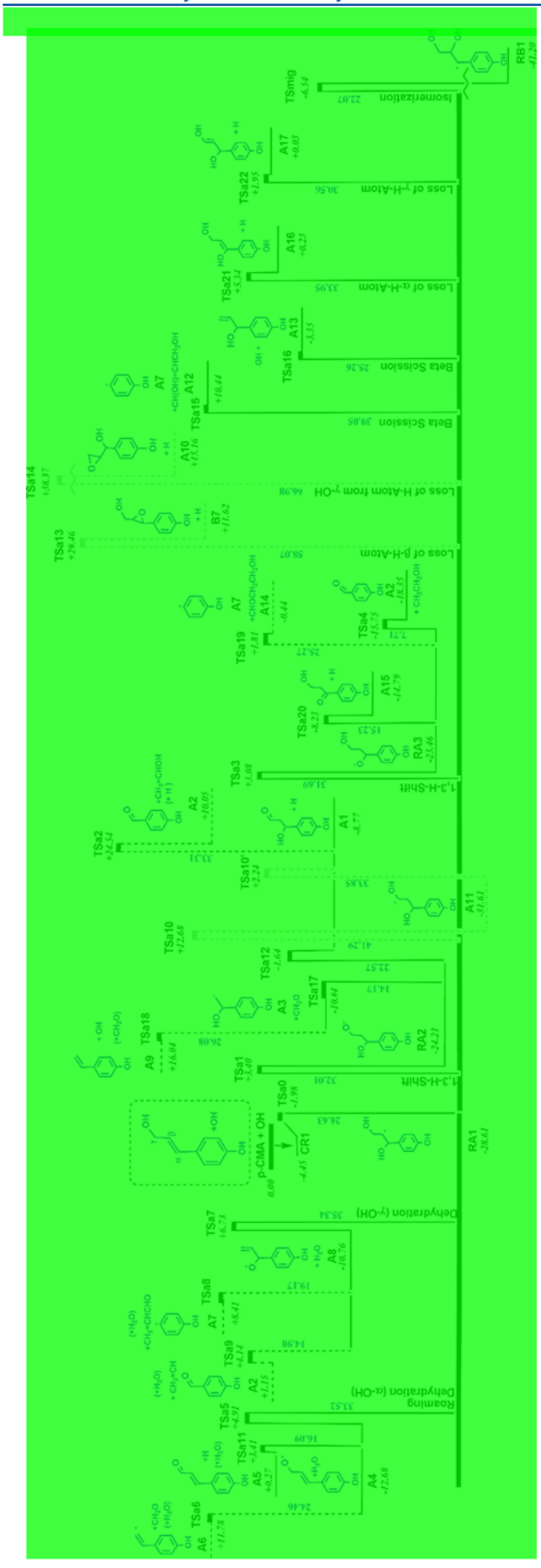

Figure 2. Enthalpy diagram (kcal/mol) for OH addition to the C7(α)-center of the side-chain double bond in *p*-CMA (Figure 1—boxed outline), calculated at the CBS-QB3 level. Solid lines represent most important (mostly low-energy) pathways. Black dashed lines represent pathways that were shown by chemical activation analysis to be important at high temperatures and pressure. Gray dashed lines are pathways shown to not be significant by chemical analysis.

higher energy (e.g., 26−34 kcal/mol for 2,2′-azo-bis-isobutyronitrile and benzoyl peroxide[22]). More advanced theoretical approaches were also utilized to explore the coupling of monolignols and relevant models.[22,68−71,108]

1.2. Monolignols. The pyrolysis of monolignols as aromatic nuclei, mimicking the primary products of the lignin pyrolysis as well as the structural motifs of the lignin side groups, is actively explored only in recent years.[13,15,18−20,24−31,77] In our previous studies, we have shown that the pyrolysis of *p*-CMA and its bare model CnA generates a large variety of phenolic compounds and benzene derivatives such as phenol, *p*-cresol, 4-vinylphenol, indene, styrene, benzaldehyde, 1-propynyl benzene, and 2-propenyl benzene and corresponding *para*-hydroxy-derivatives depending on pyrolysis conditions by utilizing both conventional and fractional pyrolysis approaches.[13,15,18−25] Remarkably, the yields of a small set of phenolics in low-temperature fractional pyrolysis of *p*-CMA constitute as high as 70% of the total gas-phase products.[24]

The conventional pyrolysis of the solid *p*-CMA reagent, performed by Akazawa et al.[24,25] at 600 °C, also showed products of phenol, *p*-cresol, 4-vinylphenol, (*E*)-4-(1-propenyl) phenol, and dihydro-*p*-coumaryl alcohol, as the major identified products. Notably, observed in this study is 4-vinylphenol, which has not been detected in the fractional pyrolysis experiments.[24] This was explained by possible further polymerization processes during fractional pyrolysis conditions similar to what occurs with monolignols (because of the higher reactivity of the vinyl group of the 4-vinylphenol in fractional pyrolysis conditions) and to contribute to the char formation and to end-up in the solid residues. Perhaps, at higher temperatures and resident times, 4-vinyl derivatives also can participate in chemically activated addition−elimination reactions such as the one discussed below. Notably, the reaction of OH + styrene is shown to proceed via addition of OH to the vinyl carbons of the styrene molecule to further support chain development by alkyl radical additions.[95]

Aldehydes are another set of abundant products in pyrolysis of monolignols.[13,21−23] The dominant formation of cinnamaldehyde was detected by Khachatryan et al.[22] during the conventional pyrolysis of CnA, along with significant amounts of dihydro- and vinyl-derivatives, as well as complex oxygenates and dimers at temperatures below 400 °C. The formation of cinnamaldehyde supported our initial proposal on the involvement of the certain free radicals, particularly O-linked conjugated radicals detected experimentally using the LTMI-EPR technique in low-temperature pyrolysis.[22] The radical processes are essential for monomer-aldehyde formation because the alternative concerted dehydrogenation of CnA forming cinnamaldehyde is a high-energy demanding process with an activation barrier as high as 79 kcal/mol.[22]

The monomer-aldehydes are also major products in pyrolysis at 400−600 °C of other phenylpropanols studied by Akazawa et al.,[24] including basic cinnamyl, sinapyl, and CFAs. Masuku[109] and Harman-Ware[29] also reported the dominant formation of

https://dx.doi.org/10.1021/acs.jpca.9b11894
J. Phys. Chem. A 2020, 124, 4875−4904

coniferyl aldehyde (CFA-aldehyde) in pyrolysis of CFA at 200−275 and 650 °C, respectively. Kawamoto et al.,[18] on the other hand, reported that the cinnamaldehyde is a major product formed during pyrolysis of CFA at typical conditions for lignin primary-pyrolysis conditions (temperature range 200−400 °C).[15,18]

Intriguingly, no *p*-coumaraldehyde [A5, 3-(4-hydroxyphenyl)-2-propenal] was detected in our fractional pyrolysis experiments;[21] this is explained by its possible rapid secondary transformations typical for fractional pyrolysis. However, the similar phenomenon has been observed by Akazawa at (400−600 °C) temperatures from conventional pyrolysis of *p*-CMA.[24,25] Notably, *p*-coumaraldehyde was not detected also from the lignin pyrolysis itself, unlike other vastly present monomer-aldehydes such as CFA-aldehyde and SPA-aldehyde and substituted benzaldehydes.[11,15,17,46,47,52−54] Thus, the detection of *p*-CMA-aldehyde is challenging, and a more detailed analysis, including kinetics, is necessary.

Akazawa et al.[24,25] postulated some tentative reaction schemes to explain their experimental results, assuming that the homolytic bond cleavages and tentative (albeit only bimolecular H-abstraction) reactions of H and OH radicals are dominant processes.

A detailed fundamentally based PES analysis was performed by Asatryan et al.[21] and they proposed a set of reaction pathways for unimolecular decomposition of *p*-CMA and its chemically activated reactions with pyrolytic H radicals. The rate constants for a few selected channels from this set of reactions were evaluated by Norinaga and co-workers,[26] along with additional rate constants for decomposition of three lignin pyrolysis products and intermediates **HHPP**, **HPPD**, and **HPP** advocated by Hough et al.[49] (*vide infra*).[14,43,47] Selected from ref 21, channels for *p*-CMA included the elimination of terminal CH_2OH group and an allylic H atom at C9, as well as H addition to C7 forming a *β*-carbon radical with further elimination of CH_2OH group to form 4-vinylphenol (*p*-hydroxystyrene).[21] However, the latter process is energetically feasible and can occur at low temperatures, as discussed in ref 21; the direct cleavages of C8−C9 and terminal H−O bonds, leading eventually to the phenol formation via hydroxystyryl radical, are energy-demanding processes, which can hardly occur at mild conditions, hence, the alternative pathways revealed in ref 21 and further developed here should be included.

It is interesting to highlight the *ipso* addition (an intriguing issue in reactivity of phenols[108,110]) of H radical to the C4-carbon center of **HPP** followed by elimination of the phenolic hydroxyl group provided by Furutani et al.[26] (channels 40, 41 in ref 21 analogous to the H ↔ OH exchange in phenols[111,112]), which appears to be remarkably feasible here, as it occurs through the barriers of only 9 and 19.8 kcal/mol heights, respectively. This pathway can serve as an important source of the OH radicals during lignin pyrolysis alongside with some other channels reported in this paper to further justify the necessity to explore our titled reaction system OH + *p*-CMA.

OH radicals can be easily generated by the removal of phenolic hydrogen to form a resonance-stabilized (quinoidal) radical O═Ph═CH−CH•−CH_2OH (analogous to breaking of a *β*-O-4 linkage in lignin), which simply decomposes into conjugated char component O═Ph═CH−CH═CH_2 and OH radicals.

Dehydration is one of the key yet not well explored processes in biomass pyrolysis.[38,102,113−116] Dehydration caused by nascent hydroxyl radicals could be expected to occur via a direct H-abstraction of the alkyl/phenolic hydroxyl groups or a skeletal carbon atom of the lignols. However, as noted above, the direct H-abstraction is not sufficiently fast and typically occurs at higher temperatures (above 500 K). This is particularly shown for the OH + AA model reaction[101] and well known for reactions of OH radicals with simple alkenes,[117−119] as opposed to some other reactions.[120]

It is also noteworthy that the H-abstraction of phenolic hydroxyl groups generates quinoidal intermediates, leading to the formation of the conjugated and fused products.[13,21−23,73,111,121] These products typically end up in the residual pyrolysis fractions, and thus, their origins are not well studied and are beyond the scope of this paper. Most of them are energy-demanding processes, such as the seemingly affordable pathway involving *β*-scission of the energized adduct, leading to the QM formation as largely quoted in the literature. We find that this requires an activation energy as high as ca 18 kcal/mol above the entrance channel. Therefore, the main focus of the current paper is on the formation mechanisms of the observed major products, primarily phenolics. For the same reason, the *ipso* OH addition to the benzene ring of *p*-CMA leading to the ring opening processes and formation of linear-conjugated compounds, shown particularly in our previous studies on pyrolysis of catechol models,[87,88] is also not explored.

On the other hand, OH addition to the double bond of the unsaturated alcohols opens up a variety of alternative low-energy reaction channels because of the chemical activation, as shown in Part I.[27] In the same vein, we have recently introduced a novel roaming-like mechanism for the low-energy dehydration of diol radicals,[102] which could account for the generation of certain C- and O-centered intermediate radicals and products. This mechanism was further confirmed in the case of the more complex reaction of OH + *p*-CMA in Part I of this study;[27] however, the kinetic significance of this novel mechanism remains to be examined and is addressed in the current paper.

To summarize, there is a variety of OH-initiated reaction pathways to generate reactive intermediates and relevant products, particularly complex oxygenates during pyrolysis of *p*-CMA. To evaluate their relative contributions and kinetic significance, one needs to systematize and analyze the pressure and temperature-dependent rate coefficients of the corresponding pathways.

The paper at hand combines a modified version of the PES for the chemically activated reactions of *p*-CMA with OH-radicals, previously developed to study the reactivity of the side-chain double bond of *p*-CMA, and incorporates a detailed kinetic analysis of the major reaction channels. It involves OH addition to both carbon centers of the double bond in *p*-CMA and compares various isomerization and product formation pathways, particularly those leading to the major products observed in both conventional and fractional experiments and generally confirmed by vaporized monolignols pyrolysis experiments.

2. METHODOLOGY

A detailed analysis of the *p*-CMA + OH PES is performed initially using the *ω*B97XD[122] dispersion- and long-range corrected hybrid DFT method from the Head-Gordon group with the moderate Pople-type basis set 6-31+G(d,p) augmented with diffuse and polarization functions.[123,124] All stationary points are reoptimized with the extended triple-*ξ*

https://dx.doi.org/10.1021/acs.jpca.9b11894
J. Phys. Chem. A 2020, 124, 4875−4904

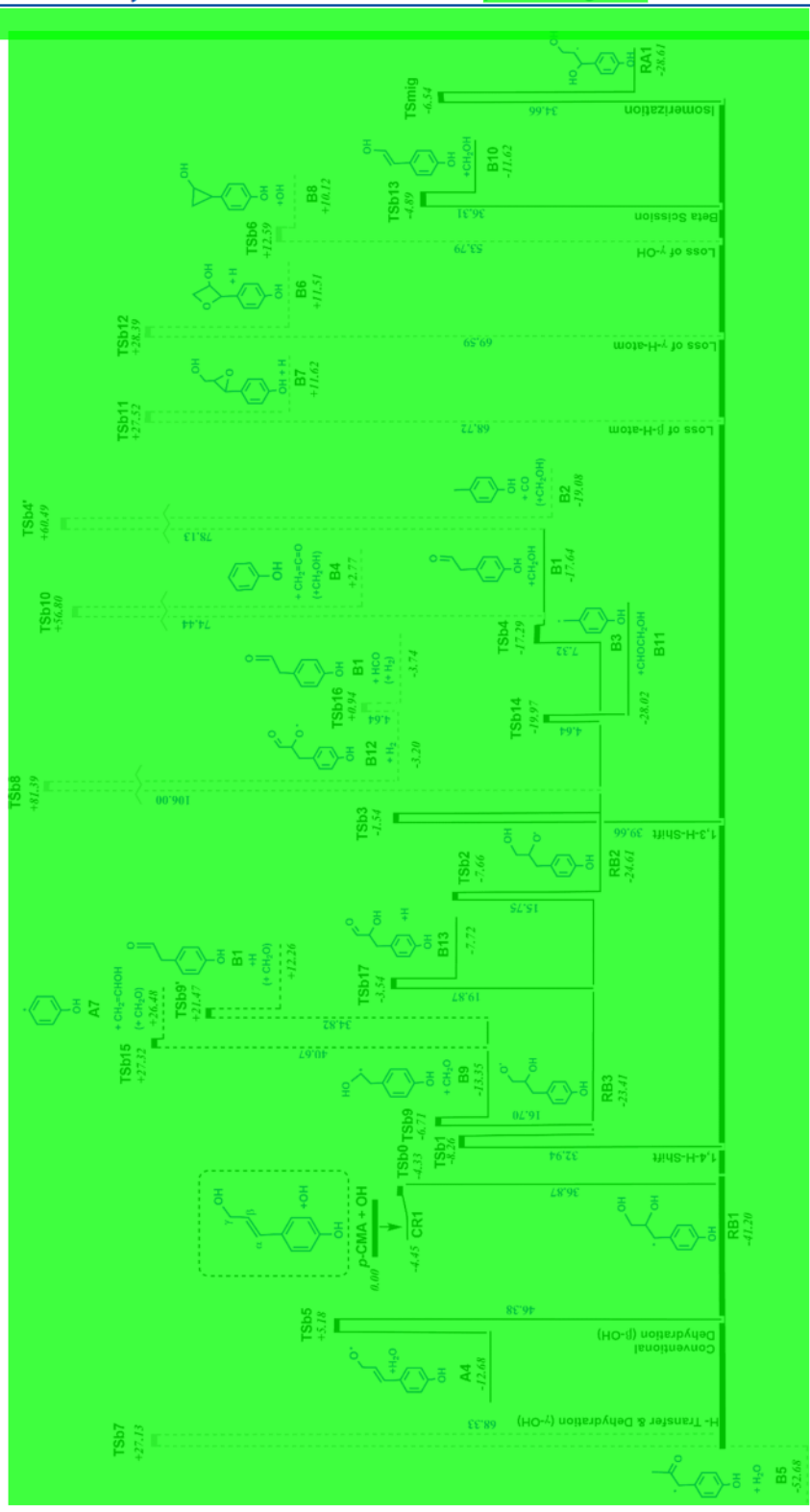

Figure 3. Enthalpy diagram (kcal/mol, ZPE-corrected electronic energies) for OH addition to the C8(β)-center of the side-chain double bond in *p*-CMA (Figure 1) calculated at the CBS-QB3 level. Solid lines represent most important low-energy pathways. Black dashed lines represent pathways that were shown by chemical activation analysis to be important at high temperatures and pressure. Gray dashed lines are pathways shown to not be significant by chemical analysis.

def2-TZVP basis set[125] where transition states have one characteristic negative eigenvalue of Hessian (force constant) matrices. The absence of this imaginary frequency verifies that the structure is at a true minimum. GaussView was utilized to visualize the intrinsic reaction coordinate analysis, which is performed at the ωB97XD/def2-TZVP level, and to verify the mode of vibrations. To ensure the connectivity of stationary points, the final point geometries at both sides of the TS were additionally optimized. Optimized geometry parameters, as well as moments of inertia and vibrational frequencies from the

https://dx.doi.org/10.1021/acs.jpca.9b11894
J. Phys. Chem. A 2020, 124, 4875−4904

ωB97XD/def2-TZVP level of theory, are presented in the Supporting Information.

High-level CBS-QB3[126,127] composite calculations are performed for all species identified on the PES to obtain more accurate energies. This method uses geometries and frequencies from the B3LYP/6-311G(2d,d,p) level with additional single-point energy calculations at the CCSD(T), MP4SDQ, and MP2 levels and a final CBS extrapolation. It also combines a correction for spin contamination (proportional to $\langle S^2 \rangle$) and a size-consistent higher-order empirical correction to predict molecular energies to around 1−3 kcal/mol accuracy (±3 kcal/mol for enthalpies of formation reported by Simmie from benchmark analysis against the Active Thermochemical Tables, refs 128 and 129). All PES calculations are performed using the Gaussian 16 program (Revision A.03).[130]

For the calculation of $\Delta H^{\circ}_{f\,298}$ values, atomization reactions from higher-level CBS-QB3 calculations are utilized where only the balancing of the target species with its constituent atoms is necessary (see ref 131 for methodological details). The reference $\Delta H^{\circ}_{f\,298}$ gas-phase values are accurately known and are 171.29 ± 0.11,[132] 52.103 ± 0.001,[132] and 59.567 ± 0.0005[133] kcal/mol for C, H, and O atoms, respectively. These CBS-QB3 calculated $\Delta H^{\circ}_{f\,298}$ values are then utilized to calculate the barrier heights in Figures 2 and 3 and are within close proximity to our previous ωB97XD results reported in Part I.[27]

As pointed out previously, all employed methods in our analysis are well tested in the literature, including our previous studies on various open-shell and molecular systems.[15,92,108,120,123,134−138] Notably, the same ωB97XD/6-31+G(d,p) method has been successfully utilized by Matsugi[136] recently for the evaluation of the roaming dynamics in dissociation of C_2H_5 radicals, a phenomenon also pertinent to our systems (*vide infra*). He also calculated the reaction energy and reverse barrier heights for the $C_2H_5 \rightarrow C_2H_3 + H_2$ reaction similar to those predicted by QCISD(T) at the complete basis set (CBS) limit. The minimally augmented basis set (equivalent to Karlsruhe def2-SVP and ma-SVP) employed above has also been recommended by Truhlar et al. as the best affordable basis set for the exploration of reaction barriers in large molecular systems.[139]

Because the next level models of the highly irregular lignin structures include even larger molecules—dimers and oligomers, the selection of a relatively simple and reliable method is essential here (quoted above comprehensive analysis by Simmie[127,128] can be well recommended for the choice of reliable methods and molecule size/method scaling and the number of calculations to be performed). For comparison purposes, the well depths of the OH addition to the double bond of *p*-CMA are additionally calculated using other well-tested DFT functionals, M06-2X[139,140] and B3LYP,[141,142] with results being fairly close to each other.

Entropy and heat capacities are calculated using the rigid-rotor harmonic-oscillator approximation for contributions from translations, vibrations, and external rotations using the Statistical Mechanics for Heat Capacity and Entropy (SMCPS) program.[143] This program includes input parameters for geometry, vibrations, and moments of inertia from the ωB97XD/def2-TZVP calculations as well as mass, electronic degeneracy, symmetry, and number of optical isomers for each species. Visual inspection of each molecule in GaussView was used for determining the symmetry and optical isomers. Zero-point vibration energies are scaled by 0.975 as recommended by Alecu et al.[144]

Single-bond internal rotations are calculated using the B3LYP[141,142] method with the 6-31+G(d,p) basis set. Potential energy (PE) curves for these rotations are created and those which fall below 5 kcal/mol are replaced with corrections to internal rotor torsional frequencies from the program ROTATOR.[145] This program expands the hindrance potential in a Fourier series, calculates the Hamiltonian matrix in the basis of wave functions of free internal rotor, and finally calculates energy levels by direct diagonalization of the Hamiltonian matrix. A truncated Fourier series calculates the internal rotor potential at discrete torsion angles

$$V(\varphi) = a_0 + \sum a_i \cos(i\varphi) + b_i \sin(i\varphi),$$

$$\text{where } i = 1 - 7$$

where the coefficients (a_0, a_i, and b_i) are calculated to provide the minima and maxima of the torsion potentials with allowance for a shift of the theoretical extreme angular positions. The summation of the SMCPS and ROTATOR contributions provide the total entropy and heat capacities for each species.

High-pressure rate constants, $k(T)$, are calculated for the 300−2000 K temperature range using the canonical transition-state theory, where degeneracy is considered in the symmetry of reactants and products:

$$k(T) = \frac{k_B T}{h} \exp\left(\frac{\Delta S_c^{\ddagger}}{R}\right) \exp\left(\frac{-\Delta H^{\ddagger}}{RT}\right) \left(\frac{RT}{P^0}\right)^{\Delta n^{\ddagger}}$$

The rate constants were corrected utilizing the Eckart asymmetric model[146−148] for tunneling and then fitted to a modified form of the Arrhenius equation to determine elementary rate parameters (A', n, E_a)

$$k(T) = A' T^n \exp\left(\frac{-E_a}{RT}\right)$$

For positions involving the C9 hydrogens, such as **A4** → **A5** + H_2O, the rates were doubled to account for the equivalent hydrogens at that location.

Temperature- and pressure-dependent rate constants are calculated using the multichannel, multifrequency quantum Rice−Ramsperger−Kassel (QRRK) analysis for $k(E)$ with master equation for falloff and stabilization as implemented in the CHEMASTER code.[149,150] The code also includes input parameters for temperature and pressure ranges, mass of the species, Lennard-Jones transport parameters for the collider molecule, third-body bath gas, reactants, and a reduced set of three representative vibrations and their degeneracies. To correctly account for product distribution from chemically activated reactions, energy dependence of the rate constant, $k(E)$, must be considered. The steady-state assumption is applied to the energized adduct where both forward and reverse reaction paths are calculated. In comparison, the formation of products is not reversible, only adjacent product formation is considered, and subsequent unimolecular dissociations are handled separately.

3. RESULTS AND DISCUSSION

Representations of the species in this study are provided in Figures 1 and 4, as well as the PE diagrams (enthalpy profiles) in Figures 2 and 3. Calculated $\Delta H^{\circ}_{f\,298}$ values from CBS-QB3

https://dx.doi.org/10.1021/acs.jpca.9b11894
J. Phys. Chem. A 2020, 124, 4875−4904

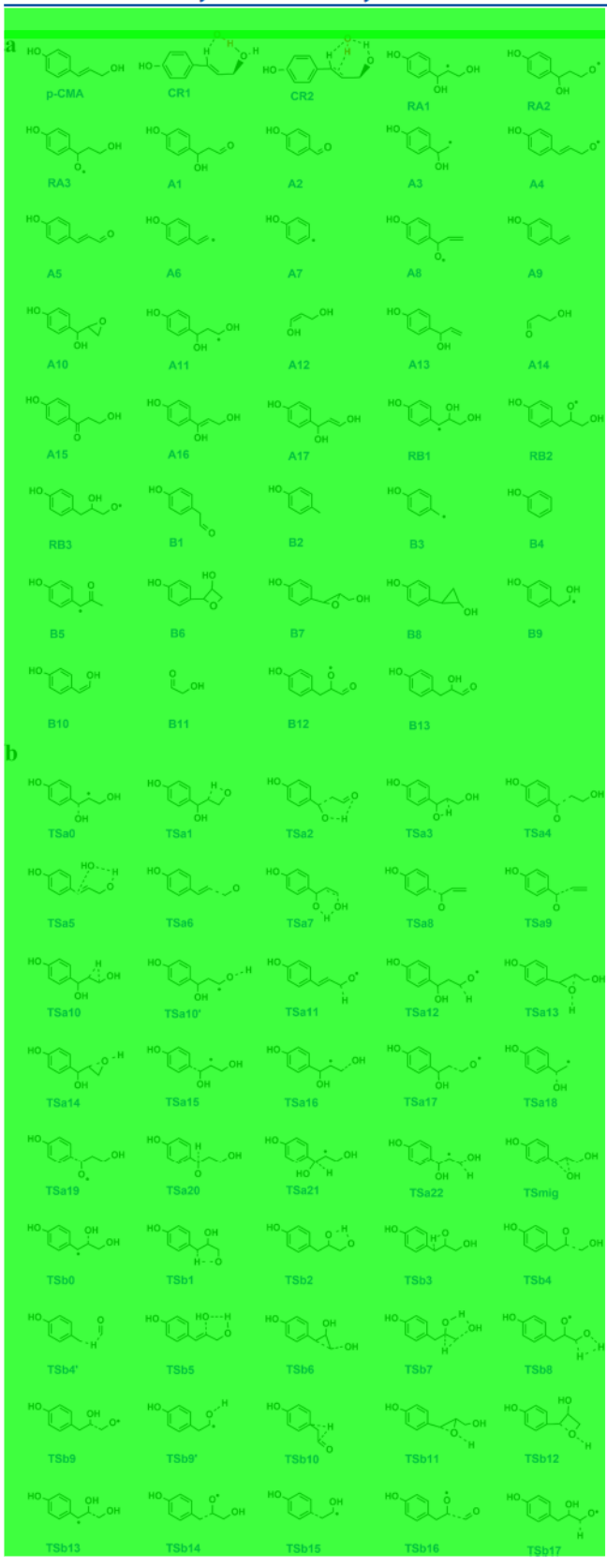

Figure 4. (a) Structures of reagents, complex reactants, and products in the *p*-CMA + OH system. (b) Structures of transition states in the *p*-CMA + OH system.

and S°_{298}, and $C_p(T)$, for $300 \leq T \leq 1500$ K, from ωB97XD/def2-TZVP calculations are presented in the Table S3. Entropy and heat capacities values are the combination of the contributions from the translations, vibrations, and external rotations with corrections for single bond rotations with barriers below 5 kcal/mol. Optimized geometries, moments of inertia, and vibrational frequencies are included in the Supporting Information. Other employed small species not calculated in this study, such as H, H_2, OH, H_2O, CO, CH_2O, HCO, CH_2=CH, CH_2OH, CH_2=C=O, CH_2=CHOH, CH_2CH_2OH, and CH_2=CHCHO, are also listed in Table S3, taken primarily from Goldsmith et al.,[151] NIST-JANAF Thermochemical Tables,[152] and Active Thermochemical Tables (ATcT).[153]

3.1. Addition of OH Radicals to the Double Bond. Hydroxyl addition to *p*-CMA generates chemically activated adduct radicals which can further isomerize, decompose to form products, or become stabilized through collisions, as it occurs with simpler reactions of OH radicals,[13,15,91,92,100,102] thus to create also some of the polyhydric alcohols found in nature. Scheme 1 shows these reactions considered in our current analysis, where corresponding energetic diagrams are depicted from CBS-QB3 energies in Figures 2 and 3. Structures of the reagents, products, and transition states are shown in Figure 4.

Addition at the *ipso*-carbon position of the benzene-ring could lead to ring-opening products such as dienones,[15,87,88] but our current analysis does not consider this scenario because the aromatic ring is conserved in the major phenolic products both under our fractional[21] and conventional[24] pyrolysis conditions. The same also occurs during the pyrolysis of CFA, which follows from our initial results on pyrolysis of vaporized reagents, as well as from those reported by Kawamoto et al.[18] and Masuku[109] at primary pyrolysis temperatures and by Harman-Ware et al.[29] at 650 °C.

A prereaction complex can form before reactions of *p*-CMA + OH occur. Even though knowledge of the exact nature of the prereaction complex is not essential from a kinetic point of view, its identification is necessary to understand the mechanism of the addition reactions.[154−157] The prereaction complexes involve weak intermolecular forces which stabilize and lower the energies before the reaction takes place. This is similar to results observed in the model OH + AA precursor reaction.[102] Prereaction complexes for hydroxyl addition to the double bond are known not only for AA[101,102] but also for model reactions with vinyl alcohol[94] and imidazole.[158]

Our analysis considered the reaction of *p*-CMA and hydroxyl radicals as an initial two-step reaction utilizing the method proposed by Alvarez-Idaboy et al.,[154,155] which has been implemented in similar reactions.[94,101,158,159] As seen in Scheme 1, the bimolecular reaction quickly forms an equilibrium, with a forward (k_1) and reverse (k_{-1}) rate constant and a complex reactant (CR) followed by the irreversible formation for the products, k_2 rate constant. This allows for the following relationship

$$k = \frac{k_1 k_2}{k_{-1}} = K_c k_2$$

where $K_c = k_1/k_{-1}$ is defined as the equilibrium constant between the *p*-CMA and OH reactants and the individual complex reactants (**CR1** and **CR2**). Subsequent reactions from these complex reactants produce products, including **RA1** and **RB1**, which will then each have an individual rate constant, denoted k_2.

For the addition of OH to *p*-CMA, two types of prereaction complexes are identified in this work, **CR1** and **CR2**. They both

https://dx.doi.org/10.1021/acs.jpca.9b11894
J. Phys. Chem. A 2020, 124, 4875−4904

Scheme 1. Reaction Pathways Triggered by OH-Addition to the C7(α)- and C8(β)-Atoms of the Double Bond in *p*-CMA, Calculated at the CBS-QB3 Level[a]

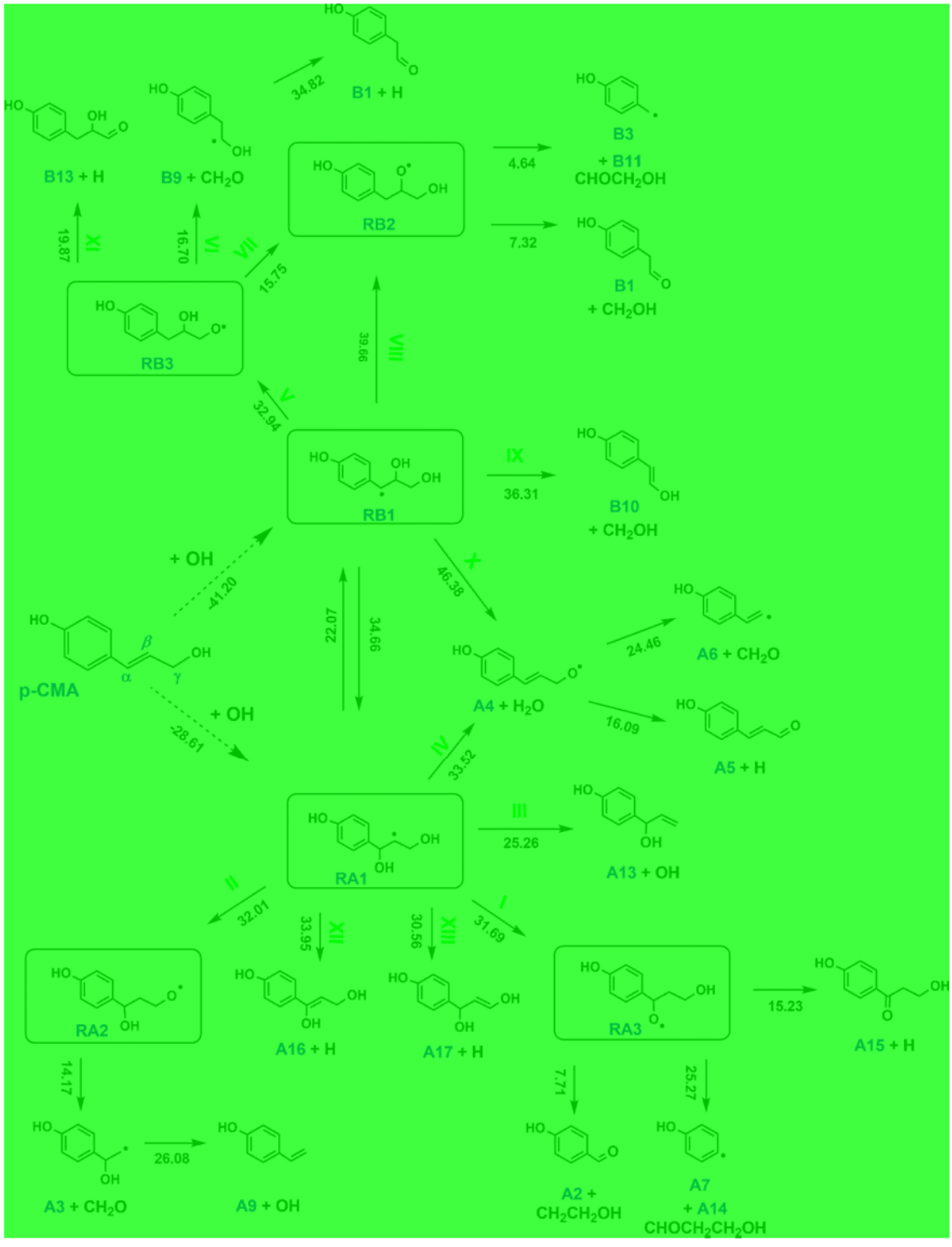

[a]Data on arrows represent corresponding enthalpy barrier heights in kcal/mol. Reaction Channel (*Ch*N) notation is given in Roman Numerals (for N).

involve interactions between O and H atoms of the nascent OH radical with H and O atoms of the terminal OH group, as well as the π-cloud of the double bond, respectively, using the unrestricted ωB97XD/6-31G(d,p) method. However, only one of those is an actual CR (*vide infra*, Figure 3a,b).

The first complex, CR1, involves two classical H-bonding interactions. One bond occurs between the hydroxyl group and a hydrogen on C7 while a second bond occurs between the hydroxyl radical and the terminal oxygen of the hydroxyl group on C9. The second complex, denoted as CR2, involves a single hydrogen bond between the hydroxyl radical and the hydrogen of the terminal hydroxyl group on C9. A second interaction also exists between the proton of the OH radical and π-electrons of the double bond between C7 and C8. In Part III, our analysis

https://dx.doi.org/10.1021/acs.jpca.9b11894
J. Phys. Chem. A 2020, 124, 4875−4904

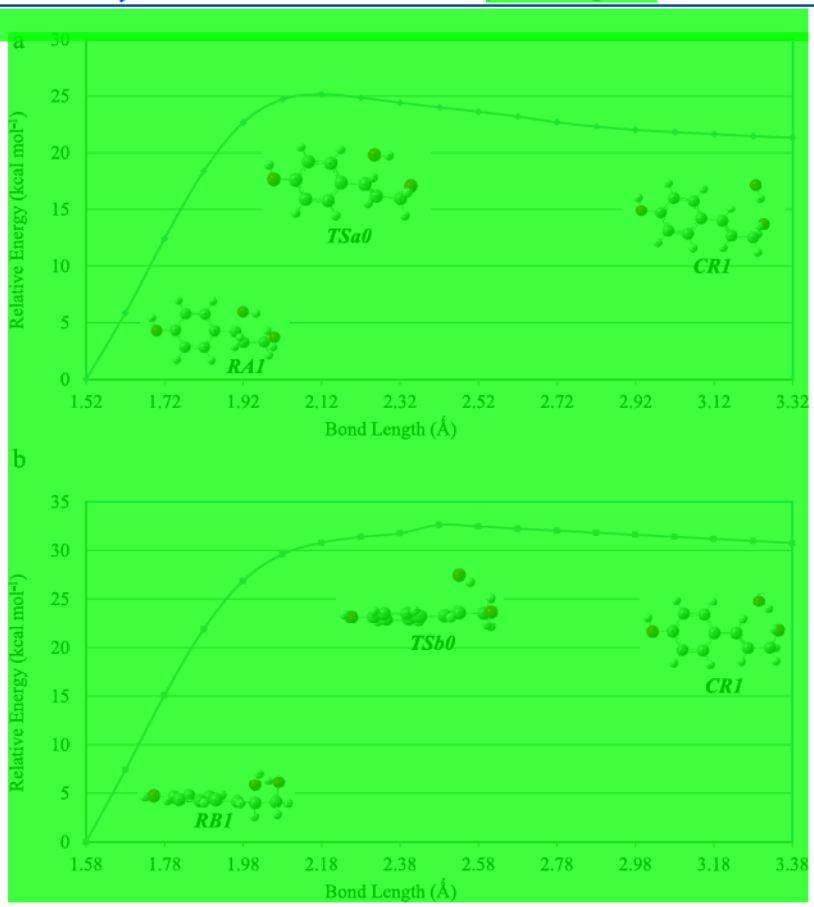

Figure 5. (a) Bond scan of CR1 to RA1 via TSa0. (b) Bond scan of CR1 to RB1 via TSb0.

will focus on chemical kinetics of H-abstractions from *p*-CMA where we will detail more H-abstraction prereaction complexes.[160]

Bond length relaxed scans are performed, Figure 5a,b, from the more stable and directional **CR1** complex to both **RA1** and **RB1** adducts over distances of 1.52−3.32 and 1.58−3.38 Å, respectively. These scans located corresponding transition states, denoted as **TSa0** for OH addition to C7(α) and **TSb0** for OH addition to C8(β), to the adduct using ωB97XD with the moderate 6-31G(d,p) basis set. Geometries were reoptimized at ωB97XD/def2-TZVP, converging on bond lengths from OH to C7(α) and C8(β) of 2.12 (**TSa0**) and 2.76 Å (**TSb0**), respectively. The **TSa0** bond length of 2.12 Å is in line with transition states determined for OH addition to the double bond in AA,[101] vinyl alcohol,[94] and styrene[95] at distances of 2.03−2.25 Å. **TSb0** has a longer bond length because of the proximity and interaction of the terminal hydroxyl group while the hydrogen bond created from the hydrogen of the hydroxyl group added and the terminal oxygen of the hydroxyl group are at 2.14 Å.

The well depths for OH + *p*-CMA to form **RA1** and **RB1** calculated in Part I (ωB97XD/def2-TZVP values) were 27.3 and 39.7 kcal/mol compared with CBS-QB3 values of 28.6 and 41.2 kcal/mol, respectively, provided here. As mentioned above, these values are consistent with well depths of 30.7 and 42.0 kcal/mol and 31.1 and 42.2 kcal/mol, respectively, evaluated with the ωB97XD and M06-2X methods with the minimally augmented basis set 6-31+G(d,p). It is noteworthy that in all cases, the chemically activated **RB1** adduct is preferred thermodynamically to **RA1** by approximately 12 kcal/mol, regardless of the method employed. The preferred formation of the α-radical adduct can be explained by the synergistic effect of the conjugation with the aromatic ring proximal radical center along with the strong H-bonding interaction between vicinal OH groups of the β-adduct (1,2-diol radical). A consistent result from the composite method further verifies applying DFT methods for these types of reactions.

In addition to all of the species described in Part I, 27 novel transition states and 17 stable species were also added into our analysis to depict this system more accurately, as shown in Figures 2 and 3. Some of these transition states were determined to replace single-step dissociation limits utilized in Part I with the exception of **RA1** to **A1** and **RB3** to **B1** + CH_2O + H. In these cases, a single-step TS could not be located; thus, multiple steps were employed. β-Scission reactions (**TSa15**, **TSa16**, **TSb13**) and the hydroxyl group transfer from **RA1** to **RB1** (**TSmig**) are now included in our analysis.

However, for further kinetic analysis, only the most affordable (lowest energy) pathways were selected and analyzed (defined by solid lines in Figures 2 and 3). Our analysis was focused on the formation mechanisms of more intricate oxygenated products observed in different experiments. This includes initial results on vaporized reagents pyrolysis, particularly producing increased amounts of benzofuran (**BF**) and acetophenone derivatives understudied in the literature (partly in catalytic processes[161]), in addition to the typical major products formed from conventional and fractional pyrolysis of *p*-CMA described above (provided in refs 38 and

https://dx.doi.org/10.1021/acs.jpca.9b11894
J. Phys. Chem. A 2020, 124, 4875−4904

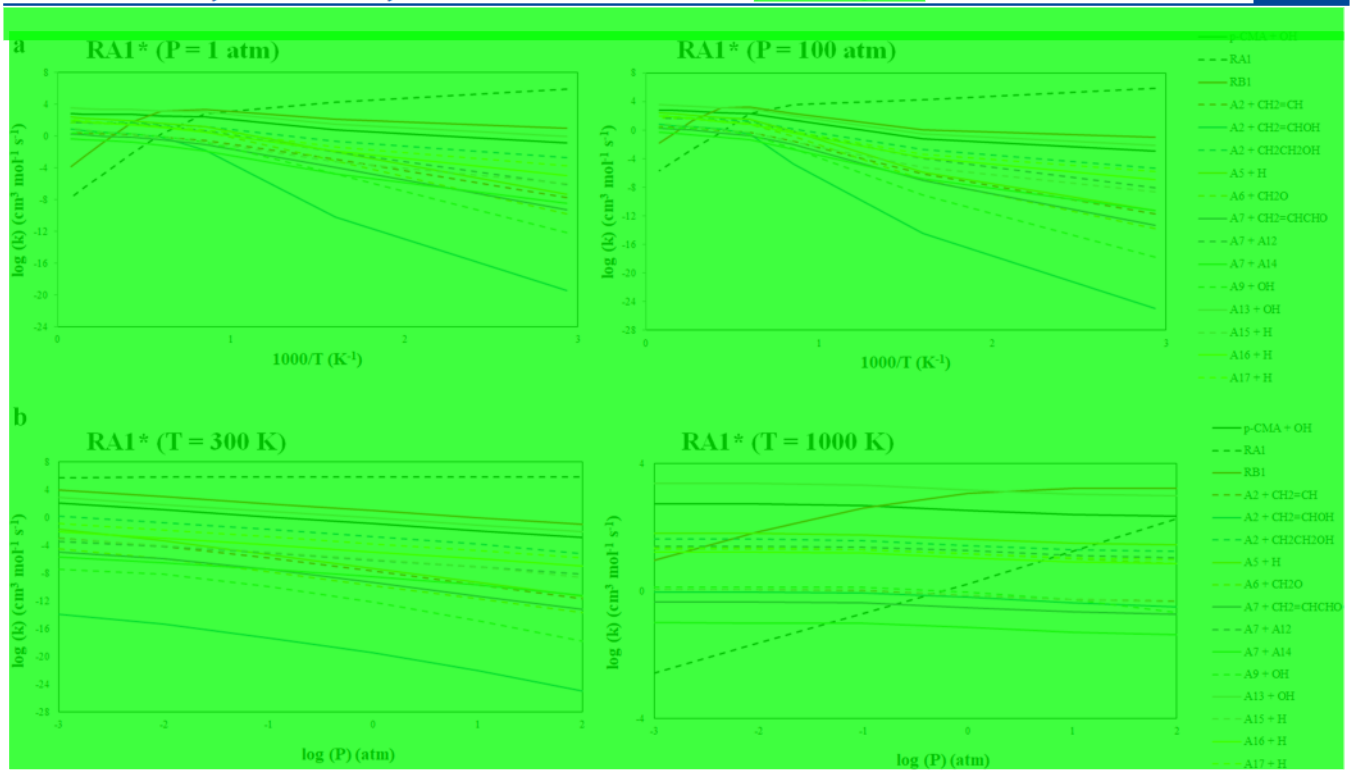

Figure 6. (a) Chemical activation rate constants vs temperature for the RA1* radical at pressures of 1 and 100 atm. (b) Chemical activation rate constants vs pressure for the RA1* radical at temperatures of 300 and 1000 K.

41), such as phenol, *p*-cresol, 4-vinylphenol, dihydro-*p*-CMA, and *p*-CMA-aldehyde.

3.1.1. Addition−Elimination and Isomerization Reactions at C_α. From the PE (enthalpy) diagrams, the addition of OH radical to the Cα atom of the double bond forms an energized adduct **RA1*** (Figure 2) with a well depth of 28.61 kcal/mol. The * (star) denoting an activated state is mostly omitted in further discussions for brevity. The **RA1*** radical can be further converted into other intermediates and products through different channels. In Figures 2 and 3, the relative energy barriers for the energized adducts, chemically activated by hydroxyl addition to *p*-CMA, are generally affordable, producing a variety of isomerization and decomposition products. We hopefully provide the important pathways in this analysis.

Two simple 1,3-hydrogen shift reactions constitute channels I and II, shown in Scheme 1, leading to the generation of two main isomers of the **RA1** adduct, viz., **RA2** and **RA3**. Scheme 1 has the reaction channel (*Ch*N) notation where the pathway (N) is given in Roman Numerals.

Channel I: The first pathway in Scheme 1 is for **RA1** to undergo a 1,3-hydrogen shift to convert to **RA3** over a 31.69 kcal/mol barrier for TSa3 given in eq 1.

$$\mathbf{RA1} \rightarrow \mathbf{RA3} \tag{1}$$

RA3 is then able to further react via several other pathways

*Ch*Ia: A low-energy β-scission over TSa4 (7.71 kcal/mol) to form one of the main pyrolysis products hydroxy-benzaldehyde (**A2**) and generate the CH_2CH_2OH radical (eq 1a). These products sit at −18.35 kcal/mol below the initial entrance channel.

$$\mathbf{RA3} \rightarrow \mathrm{HOPhHCO}\ (\mathbf{A2}) + \mathrm{CH_2CH_2OH} \tag{1a}$$

*Ch*Ib: β-Scission in **RA3** to eliminate a H atom at C7 (eq 1b) to form a complex oxygenate hydroxymethyl−hydroxyphenyl ketone, **A15** (Figure 4a), over TSa20 (15.23 kcal/mol).

$$\mathbf{RA3} \rightarrow \mathrm{HOPhC(=O)CH_2CH_2OH}\ (\mathbf{A15}) + \mathrm{H} \tag{1b}$$

A15 represents one of key lignin pyrolysis products **HHPP** (*vide infra*).[14,43,47] **A15** consists of an acetophenone core amended by a CH_2OH group at the methyl terminus.

*Ch*Ic: A bond dissociation over TSa19 (25.27 kcal/mol) forms hydroxyphenyl radical ($HOPh^\bullet$, **A7**), a precursor of the various substituted C1-phenols, along with hydroxypropional-dehyde ($CHOCH_2CH_2OH$, **A14**) better known as the antimicrobial compound reuterin (eq 1c).

$$\mathbf{RA3} \rightarrow \mathrm{HOPh^\bullet}\ (\mathbf{A7}) + \mathrm{CHOCH_2CH_2OH}\ (\mathbf{A14}) \tag{1c}$$

Channel II: The isomerization of **RA1** radical to **RA2** radical intermediate occurs via H-transfer from the γ-OH group through the barrier of TSa1 of 32.01 kcal/mol height (eq 2 and Figure 2).

$$\mathbf{RA1} \rightarrow \mathbf{RA2} \tag{2}$$

This TSa1 barrier is also somewhat (3.40 kcal/mol) higher than the energy of the free reactants (entrance channel), used as a reference level. The **RA2** isomer radical is stable—approximately at the same well depth of **RA1** at −24.21 kcal/mol.

*Ch*IIa: A low-energy (14.17 kcal/mol) pathway generates products CH_2O and **A3** intermediate carbon-cantered radical (eq 2a) from **RA2**. It further decomposes into a main pyrolysis product 4-vinylphenol (**A9**, aka hydroxystyrene) and OH requiring ca. 26 kcal/mol energy in eq 2b.

$$\mathbf{RA2} \rightarrow \mathrm{HOPhCH(OH)C^\bullet H_2}\ (\mathbf{A3}) + \mathrm{CH_2O} \tag{2a}$$

https://dx.doi.org/10.1021/acs.jpca.9b11894
J. Phys. Chem. A 2020, 124, 4875−4904

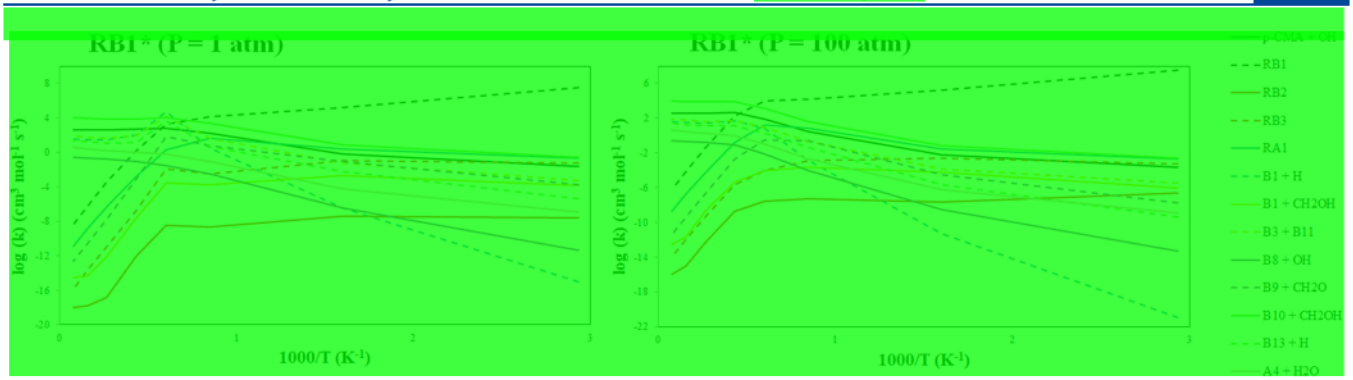

Figure 7. Chemical activation rate constants vs temperature for the **RB1*** radical at pressures of 1 and 100 atm.

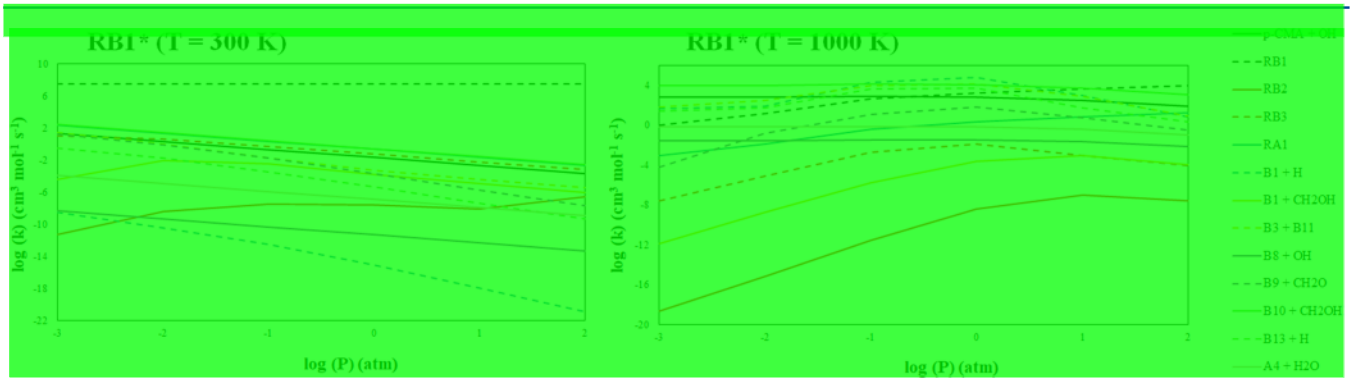

Figure 8. Chemical activation rate constants vs pressure for the **RB1*** radical at temperatures of 300 and 1000 K.

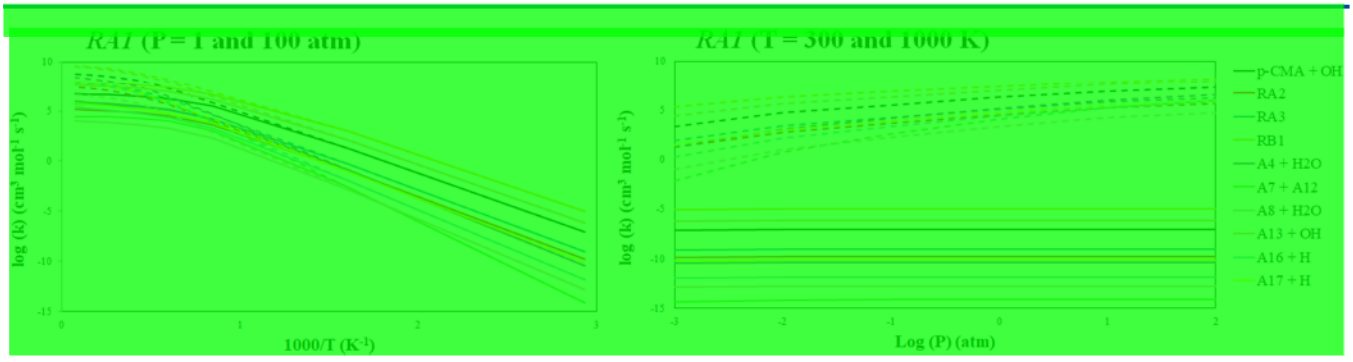

Figure 9. Rate constants vs pressure (1 and 100 atm, solid and dashed lines, respectively) and vs temperature (300 and 1000 K, solid and dashed lines respectively) for **RA1** isomerization and dissociation reactions.

$$\mathbf{A3} \rightarrow \mathrm{HOPhCH{=}CH_2}\ (\mathbf{A9}) + \mathrm{OH} \qquad (2b)$$

*Ch*IIb: The loss of a H atom from the Cγ-position of **RA2** (eq 2d) generates an α-hydroxy-isomer of coumaraldehyde (**A1**) ($\Delta E^{\#}$ = 22.57 kcal/mol while still below the entrance level). It also contributes to the regeneration of H atoms, one of the reactive "pool radicals."

$$\mathbf{RA2} \rightarrow \mathrm{HOPhCH(OH)CH_2CHO}\ (\mathbf{A1}) + \mathrm{H} \qquad (2c)$$

*Ch*IIc: A barrier energy of 33.31 kcal/mol representing the Cα−Cβ bond breaking to form the **A2** product with the CH_2=CHOH radical in eq 2d.

$$\mathrm{HOPhCH(OH)CH_2CHO}\ (\mathbf{A1}) \rightarrow \mathrm{HOPhHCO}\ (\mathbf{A2}) + \mathrm{CH_2{=}CHOH} \qquad (2d)$$

Channel II′: A secondary pathway, eqs 3 and 3a, to generate the same products as in eq 2c involves **RA1** with an initial H atom transfer from the Cγ-position to the Cβ-position over a 41.29 kcal/mol energy barrier height (via **TSa10**), leading to the formation of $HOPhCH(OH)CH_2C^{\bullet}HOH$ (**A11**) γ-radical species approximately 3 kcal/mol lower in energy than **RA1**. **A11** can then lose the H atom from the γ-OH group over a 33.85 kcal/mol energy barrier to form OH-substituted hydroxyphenyl α-hydroxy propionaldehyde **A1** and H atom (eq 3a).

$$\mathbf{RA1} \rightarrow \mathrm{HOPhCH(OH)CH_2C^{\bullet}HOH}\ (\mathbf{A11}) \qquad (3)$$

$$\mathbf{A11} \rightarrow \mathrm{HOPhCH(OH)CH_2CHO}\ (\mathbf{A1}) + \mathrm{H} \qquad (3a)$$

Channel III: A more favorable and lower energy pathway (eq 4) exists for β-scission of the terminal OH group of Cγ, creating 4-(1-hydroxy-2-propenyl)phenol (**HPP**), HOPhCH(OH)-CH=CH_2 (**A13**), and α-hydroxy isomer of *p*-CMA (Figure 4).

$$\mathbf{RA1} \rightarrow \mathrm{HOPhCH(OH)CH{=}CH_2}\ (\mathbf{A13}) + \mathrm{OH} \qquad (4)$$

The formation of **A13** + OH via β-scission of **RA1** (eq 4) is one of the lowest barrier pathways (25.26 kcal/mol barrier over

https://dx.doi.org/10.1021/acs.jpca.9b11894
J. Phys. Chem. A 2020, 124, 4875−4904

TSa16)—the second lowest energy only to RB1 formation over TSmig, 22.07 kcal/mol. Chemical activation (Section 3.2.1) and the isomerization and dissociation of RA1 (Figure 9) both show the importance of this pathway with the only initial barrier below the entrance level by 3.35 kcal/mol. Figure 9 also depicts how dominating these pathways are, including the reformation of *p*-CMA + OH, for RA1 isomerization and dissociation.

Channel IV: The activation of readily available hydroxyl groups in lignin and lignols can particularly provide opportunities for the intramolecular dehydration processes. Although molecular dehydration (even that catalyzed by water[8]) is an energy-demanding process,[8,14,114−116] the dehydration of intermediate radicals is more favorable energy-wise[27,102] to generate various radical intermediates and products. Dehydration by nascent OH radicals can involve both alkyl and phenolic types of OH groups, as well as skeletal H atoms (eq 5).

$$\mathbf{RA1} \rightarrow \mathrm{HOPhCH{=}CHCH_2CH_2O^{\bullet}}\ (\mathbf{A4}) + \mathrm{H_2O} \qquad (5)$$

*Ch*IVa and *Ch*IVb: Dehydration involving α-OH of RA1 via roaming-like TSa5 (located 4.91 kcal/mol above the entrance channel) produces O-centered radical intermediate A4 (eq 5), which decomposes further to form *p*-CMA-aldehyde (A5) and H atom (eq 5a, *Ch*IVa) or, alternatively, A6 + CH_2O (eq 5b, *Ch*IVb). Chemical activation shows that A5 formation is favorable at <500 K. A6 can add up an H atom from a donor to form an abundant pyrolysis product 4-vinylphenol, whereas its dissociation is of higher energy and requires 44.0 kcal/mol energy (eq 5c).[27]

$$\mathbf{A4} \rightarrow \mathrm{HOPhCH{=}CHCH_2CHO}\ (\mathbf{A5}) + \mathrm{H} \qquad (5a)$$

$$\mathbf{A4} \rightarrow \mathrm{HOPhCH{=}CH^{\bullet}}\ (\mathbf{A6}) + \mathrm{CH_2O} \qquad (5b)$$

$$\mathbf{A6} \rightarrow \mathrm{HOPh^{\bullet}}\ (\mathbf{A7}) + \mathrm{C_2H_4}\ (44.0\ \mathrm{kcal/mol}) \qquad (5c)$$

A4 is a key radical intermediate identified in our earlier study on H + *p*-CMA, denoted as R(O9),[24] to generate the controversial (for *p*-CMA, *vide supra*) product A5 representing *p*-CMA-aldehyde.

One of the major focal points of Part I of our analysis was the OH roaming-like dehydration transition states and their ability to offer lower energy barriers for *p*-CMA + OH reactions. A roaming-like dehydration mechanism was proposed previously while analyzing the OH + AA model reaction and how it provides a low-energy dehydration pathway to explain various experimental data.[102] A low-energy roaming pathway was also identified in Part I for the reaction of OH with *p*-CMA monomer (TSa5).[27]

In Part I of our analysis, the pure DFT ωB97X-D/def2-TZVP level, which additionally involves corrections for dispersion and long-range interactions, predicted a roaming-like transition state (TSa5), generating a barrier energy of 25.54 kcal/mol which was the lowest energy pathway from RA1, being 1.73 kcal/mol below the entrance level. In contrast, in our current analysis, we note that the roaming dehydration pathway does not provide the lowest energy barrier originating from the RA1 adduct using the CBS-QB3 methodology utilizing the B3LYP functional for geometry optimizations with modest characterization of dispersion interactions. The transition states for both 1,3-H shift reactions (viz., TSa1 and TSa3 in Figure 2) are located 1−2 kcal/mol lower than TSa5. TS for β-scission of OH radical (TSa16) to form A13 is even lower at *ca.* 3.35 kcal/mol below the entrance channel.

The comparison of the corresponding TSa5 geometries by two DFT-based methods, however, does not show significant differences. Both resemble H-abstraction TSs; however, because of the flatness of the PES region, a full downward optimization leads to the 1,3-diol adduct rather than the isolated reagents, as would be expected for a classical bimolecular reaction. This is similar to what was observed for the OH + AA model reaction.[102] In the meantime, a group of DFT methods involving Grimme's D3-dispersion corrections (such as B97D3, BP86-D3, and N11-D3) predict a saddle point with typical roaming features (loose structures, the energies below the reagents asymptote, etc.).

In contrast to the primarily DFT-based results in smaller model OH + AA analysis (see the Supporting Information in ref 102 for an extended discussion), a typical roaming-like TS structure was identified also at MP2[102] *ab initio* level for OH + *p*-CMA system on a flat PE surface region.

The roaming features in OH + AA and OH + *p*-CMA are similar to that found for the CH_2CH_2OH adduct of the OH + C_2H_4 reaction by Kamarchik et al.,[39] based on a large series of comprehensive experimental and theoretical studies.

Dehydration can also occur via direct H-abstraction by H atoms generated during pyrolysis. The kinetics of all possible H-abstraction reactions (direct dehydration channels as well as other abstraction via pool radicals) will be detailed in a separate publication on kinetics, including analysis of a prereaction complex (CRs) formation. Comparisons to available resulting products including 4-vinylphenol (A9), HPP, O=Ph=CH−CH=CH_2, and A4 will be discussed.

Channel XII: The β-Scission of RA1 adduct leads to the formation of 1,3-diol molecule (A16) + H via TSa21. In fact, this is an exchange of the α-H atom of *p*-CMA by nascent OH radical (eq 6a).

$$[p\text{-CMA} + \mathrm{OH}] \rightarrow \mathbf{RA1} \rightarrow \mathrm{HOPhC(OH){=}CHCH_2OH}\ (1,3\text{-diol},\ \mathbf{A16}) + \mathrm{H} \qquad (6a)$$

The overall process is almost thermoneutral (exothermic by only 0.23 kcal/mol, Figure 2), however, there is a substantial barrier located above the entrance channel by 5.34 kcal/mol for the formation of A16. On the other hand, the barrier for OH + *p*-CMA addition is located below the entrance level via the formation of a prereaction complex (*vide supra*). The relatively low dissociation barrier is due to the formation of a strong hydrogen bond in the resulting diol molecule. Because dissociation is favored by entropy, the analysis of the kinetics of this reaction in detail is important (see, Section 3.2).

Channel XIII: β-Scission of the RA1 adduct leads also to the formation of an unsaturated 1,3-diol molecule (A17) + H via TSa22 and the loss of a γ-H atom from RA1 (eq 6b).

$$\mathbf{RA1} \rightarrow \mathrm{HOPhC(OH)CH{=}CHOH}\ (\text{unsaturated 1, 3-diol},\ \mathbf{A17}) + \mathrm{H} \qquad (6b)$$

The overall process is, again, thermoneutral (endothermic with an overall product energy of 0.03 kcal/mol) with an energy barrier, TSa22, of 30.56 kcal/mol height.

Channel XIV′: Some higher-energy pathways leading to the key pyrolysis products, as well as species determined to be important through chemical activation analysis such as phenol radical (A7) and RA1 dehydration product HOPhCH($O^{\bullet}$)-CH=CH_2 (A8), are also analyzed.

https://dx.doi.org/10.1021/acs.jpca.9b11894
J. Phys. Chem. A 2020, 124, 4875−4904

*Ch*XIV′: The phenol radical (A7) can be directly generated through β-scission of **RA1** over **TSa15** (+39.05 kcal/mol) to additionally form CH(OH)=CHCH$_2$OH (**A12**) according to eq 7.

$$\mathbf{RA1} \rightarrow \mathrm{HOPh}^{\bullet}\ (\mathbf{A7}) + \mathrm{CH(OH)}{=}\mathrm{CHCH_2OH}\ (\mathbf{A12}) \quad (7)$$

Channel XIV″: *Ch*XIV″a: Conventional dehydration through **TSa7** (35.34 kcal/mol) involving the γ-OH group (eq 8) to form **A8** followed by bond cleavage over **TSa8** (19.17 kcal/mol) to generate **A7** radicals to contribute to the main product phenol formation + acrolein, CH$_2$=CHCHO (eq 8a).

$$\mathbf{RA1} \rightarrow \mathrm{HOPhCH(O^{\bullet})CH{=}CH_2}\ (\mathbf{A8}) + \mathrm{H_2O} \quad (8)$$

$$\mathbf{A8} \rightarrow \mathrm{HOPh}^{\bullet}\ (\mathbf{A7}) + \mathrm{CH_2{=}CHCHO} \quad (8a)$$

*Ch*XIV″b: **A8** can also split into benzaldehyde (hydroxy-derivative, **A2**) via **TSa9** (eq 8b).

$$\mathbf{A8} \rightarrow \mathrm{HOPhHCO}\ (\mathbf{A2}) + \mathrm{CH_2{=}C^{\bullet}H} \quad (8b)$$

Note that a lower energy competitive reaction via **TSa4** to form **A2** + CH$_2$CH$_2$OH is also available to produce **A2** (*Ch*I, eq 1a).

3.1.2. Addition−Elimination and Isomerization Reactions at C_β. The addition of OH radical to the C_β generates **RB1*** to trigger a variety of chemically activated pathways:

Channel V: Isomerization of **RB1*** is most energetically favored channel via **TSb1** located 8.26 kcal/mol below the entrance level to form **RB3** intermediate radicals (eq 9)

$$\mathbf{RB1} \rightarrow \mathbf{RB3} \quad (9)$$

Further reactions form **RB3** via *Ch*V are, however, somewhat complicated because of the variety of other emerging pathways described further as *Ch*VI, *Ch*VII, and *Ch*XI channels.

There is an entropically favored option for direct decomposition of the **RB3** isomer via β-scission. A straightforward pathway to form **B1** involving concerted H-elimination of the OH group at Cβ (eq 9a) requires only 35.67 kcal/mol energy (*Ch*VI). There is an alternative to the stepwise decomposition (eq 9b) through transition-state **TSb9** and **B9** intermediates.

$$\mathbf{RB3} \rightarrow \mathrm{HOPhCH_2CHO}\ (\mathbf{B1}) + \mathrm{CH_2O} + \mathrm{H} \quad (9a)$$

$$\mathbf{RB3} \rightarrow \mathrm{HOPhCH_2C^{\bullet}HOH}\ (\mathbf{B9}) + \mathrm{CH_2O} \rightarrow \mathrm{HOPhCH_2CHO}\ (\mathbf{B1}) + \mathrm{H}\ (+\ \mathrm{CH_2O}) \quad (9b)$$

RB3 can also isomerize to **RB2** via **TSb2** (eq 9c), to make available low-energy pathways via **TSb4** and **TSb14** (*vide infra*, *Ch*VII).

$$\mathbf{RB3} \rightarrow \mathbf{RB2} \quad (9c)$$

The final pathway is for H atom elimination on the C9 position of the **RB3** radical over **TSb17** forming **B13** (*Ch*XI, eq 9d).

$$\mathbf{RB3} \rightarrow \mathrm{HOPhCH_2CH(OH)CHO}\ (\mathbf{B13}) + \mathrm{H} \quad (9d)$$

Channel VI: *Ch*VIa: The C8−C9 bond in **RB3** is broken during the first step over **TSb9** at an energy cost of 16.70 kcal/mol. This creates formaldehyde and HOPhCH$_2$C$^{\bullet}$HOH (**B9**) intermediate radical, which then further reacts over a larger 34.82 kcal/mol energy barrier (**TSb9′**), representing the loss of the H atom from the terminal hydroxyl group creating **B1** (eq 9b).

B9 can also undergo another β-scission (eq 9e) to form *para*-hydroxy phenyl radicals (**A7**) and vinyl alcohol (CH$_2$=CHOH) over **TSb15** with a higher energy requirement of 40.67 kcal/mol.

$$\mathbf{B9} \rightarrow \mathrm{HOPh}^{\bullet}\ (\mathbf{A7}) + \mathrm{CH_2{=}CHOH} \quad (9e)$$

Channel VII: *Ch*VIIa: As was pointed out in Part I of our analysis, an alternative to straightforward **B1** formation (*vide infra*), the isomerization of **RB3** to **RB2** can occur over **TSb2** (15.75 kcal/mol height)—almost isoenergetic to the **TSb9** transition state, followed by a small 7.32 kcal/mol energy barrier **TSb4** for Cβ−Cγ bond fission to form 4-hydroxyphenylacetaldehyde (**B1**) as seen in eq 10a.

$$\mathbf{RB2} \rightarrow \mathrm{HOPhCH_2CHO}\ (\mathbf{B1}) + \mathrm{CH_2OH} \quad (10a)$$

*Ch*VIIb: An even faster process triggered by **RB2** can occur over the remarkably low-energy barrier **TSb14** (4.64 kcal/mol height), leading to the formation of **B3** (eq 10b), the radical precursor of *p*-cresol, one of the most abundant products of *p*-CMA pyrolysis, and **B11**.

$$\mathbf{RB2} \rightarrow \mathrm{HOPhC^{\bullet}H_2}\ (\mathbf{B3}) + \mathrm{CHOCH_2OH}\ (\mathbf{B11}) \quad (10b)$$

*Ch*VIIc: Direct decomposition (β-scission) of the **RB2** isomer also is a straightforward pathway to form **B1** via H-elimination of OH group at the terminal Cγ-atom. This kinetically favored pathway also requires a low energy of 36.87 kcal/mol (eq 10c).

$$\mathbf{RB2} \rightarrow \mathrm{HOPhCH_2CHO}\ (\mathbf{B1}) + \mathrm{CH_2O} + \mathrm{H} \quad (10c)$$

Channel VIII: There is an alternative isomerization channel for the **RB1** adduct to form **RB2** radicals via (eq 11) to play an important role following a direct decomposition and two low-barrier product formation pathways.

$$\mathbf{RB1} \rightarrow \mathbf{RB2} \quad (11)$$

Isomerization of **RB1*** to form **RB2** (eq 11) over the 39.66 kcal/mol energy barrier (1.54 kcal/mol below the entrance level) for **TSb3** is an energetically favored process. Further reaction pathways (*Ch*VIIIa,b) overlap with the *Ch*VIIa,b, leading to two low-energy barrier reactions via **TSb4** and **TSb14** according to eqs 10a and 10b.

Channel IX: β-Scission of **RB1** between the Cβ-Cγ bond (eq 11) has a barrier height of 36.31 kcal/mol over **TSb13** to create HOPhCH=CHOH (**B10**) and an active radical CH$_2$OH, which can further develop the chain reactions. This is the most energetically preferred reaction initiated from **RB1** with the barrier below the entrance channel by 4.89 kcal/mol, while also being entropically preferred. The chemical activation analysis shows that these products are the fastest reaction triggered by **RB1*** across the temperatures and pressures considered (see Section 3.2.2).

$$\mathbf{RB1} \rightarrow \mathrm{HOPhCH{=}CHOH}\ (\mathbf{B10}) + \mathrm{CH_2OH} \quad (11)$$

The β-scission reaction of **RB1** over **TSb13** has a barrier height similar to that of **RA1** formation over **TSmig**. **B10** formation is shown to be the fastest triggered by the **RB1** reaction, although the isomerization to **RA1** is close, but as the temperature and pressure increases, the **B10** formation dominates overall.

Channel X: As was seen with **RA1**, dehydration reactions are kinetically important to the *p*-CMA + OH reaction scheme presented. The conventional dehydration of **RB1** to form **A4** + H$_2$O via **TSb5** is located 5.18 kcal/mol above the entrance

https://dx.doi.org/10.1021/acs.jpca.9b11894
J. Phys. Chem. A 2020, 124, 4875−4904

Table 1. Summary of Elementary High-Pressure Rate Parameters for Reactions Studied in the *p*-CMA + OH System[a]

	forward			reverse		
reactions	A'	n	E_a	A'	n	E_a
p-CMA + OH → RA1	2.71×10^{-9}	3.43	−8.1	1.45×10^{12}	0.37	27.1
RA1 → RA2	2.84×10^{8}	1.17	28.7	2.84×10^{8}	1.35	24.3
RA1 → RA3	1.40×10^{9}	1.10	28.3	1.54×10^{8}	1.49	23.2
RA1 → RB1	2.98×10^{10}	0.86	22.2			
RA1 → A4 + H_2O	1.52×10^{9}	1.45	31.8	7.22×10^{-2}	3.55	14.9
RA1 → A7 + A12	4.42×10^{14}	0.06	39.7			
RA1 → A8 + H_2O	5.32×10^{8}	1.14	33.4	4.81×10^{-1}	2.97	14.6
RA1 → A10 + H	2.14×10^{9}	1.16	65.5			
RA1 → A11	9.16×10^{5}	2.01	37.2	1.19×10^{6}	2.06	40.1
RA1 → A13 + OH	7.75×10^{10}	0.89	25.5			
RA1 → A16 + H	5.34×10^{6}	2.09	32.6			
RA1 → A17 + H	8.54×10^{5}	2.22	28.9			
RA1 → B7 + H	1.57×10^{8}	1.39	56.2			
RA2 → A1 + H	6.63×10^{9}	1.31	21.8	6.18×10^{7}	1.71	6.5
RA2 → A3 + CH_2O	1.80×10^{12}	0.44	14.7	1.67×10^{-1}	3.16	−1.4
RA3 → A2 + CH_2CH_2OH	6.02×10^{11}	0.49	7.9			
RA3 → A7 + A14	8.57×10^{11}	0.65	24.7			
RA3 → A15 + H	4.02×10^{6}	2.04	13.6			
A1 → A2 + CH_2=CHOH	5.39×10^{6}	1.72	31.0			
A3 → A9 + OH	4.30×10^{9}	1.15	25.5			
A4 → A5 + H	4.48×10^{6}	1.86	14.4			
A4 → A6 + CH_2O	2.01×10^{12}	0.46	25.0			
A8 → A2 + CH_2=CH	8.58×10^{11}	0.47	15.0			
A8 → A7 + CH_2=CHCHO	1.12×10^{12}	0.61	19.4			
A11 → A1 + H	6.14×10^{8}	1.42	32.1	4.16×10^{6}	1.95	9.4
p-CMA + OH → RB1	5.17×10^{-11}	3.97	−10.9	2.02×10^{12}	0.44	37.4
RB1 → RB2	1.02×10^{4}	2.67	35.0	3.21×10^{3}	2.99	18.3
RB1 → RB3	2.35×10^{3}	2.51	27.9	6.62×10^{2}	2.69	10.1
RB1 → RA1	2.43×10^{12}	0.40	35.2			
RB1 → B5 + H_2O	1.61×10^{8}	1.25	66.9			
RB1 → B6 + H	2.81×10^{3}	2.49	64.8			
RB1 → B7 + H	5.77×10^{8}	1.28	66.9			
RB1 → B8 + OH	1.46×10^{11}	0.56	53.7			
RB1 → B10 + CH_2OH	2.07×10^{10}	1.40	35.9			
RB1 → A4 + H_2O	7.24×10^{3}	2.56	41.5			
RB2 → B1 +CH_2OH	9.04×10^{11}	0.56	7.5	2.55×10^{-1}	3.01	−0.6
RB2 → B3 + B11	4.97×10^{11}	0.51	4.8			
RB2 → B12 + H_2	6.98×10^{4}	2.65	101.7	2.19×10^{1}	3.06	80.2
RB3 → RB2	1.08×10^{8}	1.24	12.0	1.25×10^{8}	1.38	13.1
RB3 → B9 + CH_2O	3.48×10^{12}	0.34	17.3	1.65×10^{2}	2.43	6.3
RB3 → B13 + H	4.23×10^{9}	1.32	19.2			
B1 → B2 + CO	1.71×10^{4}	2.93	73.4			
B1 → B4 + CH_2=C=O	4.28×10^{10}	0.63	74.7			
B9 → B1 + H	2.12×10^{7}	2.06	32.5			
B9 → A7 + CH_2=CHOH	6.56×10^{12}	0.38	41.0			
B12 → B1 + HCO	1.26×10^{12}	0.55	4.3			

[a]Units: A' (mol cm^{-3} s^{-1}), E_a (kcal mol^{-1}).

level. Subsequent further decomposition of A4 into A5 and H atom, as seen in RA1 dehydration, could then occur (see *Ch*IV).

The dehydration barrier (TSb5, 46.38 kcal/mol) is higher than that from RA1 (TSa5, 33.52 kcal/mol). This energy difference can be explained by the formation of a strained five-membered ring TSs in the TSb5 structure, leading to increased activation energy, unlike in the case of the 1,3-dehydration in RA1, which involves a more relaxed six-membered ring TSa5. The effect of TS ring-size on barrier heights is also observed and analyzed in the simpler OH + AA model reaction.[102]

Channel XI: A low-energy process from RB3, see *Ch*VI and *Ch*VII, can occur via elimination of the allylic hydrogen (at C9) to form an experimentally significant product B13: $HOPhCH_2CH(OH)C(=O)H$ (eq 12). BDE for this reaction is only 15.68 kcal/mol, whereas the barrier height constitutes 19.87 kcal/mol ($\Delta E^{\#}_{rev}$ = 4.18 kcal/mol)

$$\text{RB3} \rightarrow HOPhCH_2CH(OH)C(=O)H\ (\text{B13}) + H \quad (12)$$

Channel XV′: The last important (although potentially insignificant) reaction pathway for RB1* at mild conditions is loss of the γ-OH over TSb6 with an energy barrier of 53.79

https://dx.doi.org/10.1021/acs.jpca.9b11894
J. Phys. Chem. A 2020, 124, 4875−4904

Table 2. CHEMASTER Input Rate Constant Parameter Modifications for Well Species for the *p*-CMA + OH System[a]

reactions	original A′	modified A′	notes
A1 + H → RA2	6.18×10^{7}	1.00×10^{0}	lower A′
A1 → A2 + CH_2=CHOH	5.39×10^{6}	5.07×10^{6}	C_p ratio = 0.94
A3 → A9 + OH	4.30×10^{9}	3.61×10^{9}	C_p ratio = 0.84
A4 → A5 + H	4.48×10^{6}	3.94×10^{6}	C_p ratio = 0.88
A4 → A6 + CH_2O	2.01×10^{12}	1.77×10^{12}	C_p ratio = 0.88
A8 → A2 + CH_2=CH	8.58×10^{11}	7.55×10^{11}	C_p ratio = 0.88
A8 → A7 + CH_2=CHCHO	1.12×10^{12}	9.86×10^{11}	C_p ratio = 0.88
A1 + H → A11	4.16×10^{6}	1.00×10^{0}	lower A′
B12 + H_2 → RB2	2.19×10^{1}	1.00×10^{0}	lower A′
B9 + CH_2O → RB3	1.65×10^{2}	1.00×10^{0}	lower A′
B1 → B2 + CO	1.71×10^{4}	1.35×10^{4}	C_p ratio = 0.79
B1 → B4 + CH_2=C=O	4.28×10^{10}	3.38×10^{10}	C_p ratio = 0.79
B9 → B1 + H	2.12×10^{7}	1.80×10^{7}	C_p ratio = 0.85
B9 → A7 + CH_2=CHOH	6.56×10^{12}	5.58×10^{12}	C_p ratio = 0.85
B12 → B1 + HCO	1.26×10^{12}	1.15×10^{12}	C_p ratio = 0.91

[a]Units: A' (mol cm^{-3} s^{-1}).

kcal/mol to form **B8** with a cyclopropane side chain. The structure of **TSb6** forming a three-membered ring is the reason for the high energy barrier, but in comparison to the three- and four-membered oxygen containing ring (oxirane and oxetane, respectively) formed in **TSb11** and **TSb12** with an accompanying 15 kcal/mol energy increase, this is feasible. However, further transformations to form such structures are not ruled out.

3.2. Kinetic Analysis. Reactions of the chemically activated **RA1*** and **RB1*** adducts, formed from *p*-CMA + OH association, at their initial formation have approximately 29 and 41 kcal/mol of excessive energy from the new bond formed, respectively. These adducts can undergo isomerization and dissociation reactions or become deactivated through collisional stabilization. The elementary high-pressure rate parameters for the forward and reverse reactions studied in the *p*-CMA + OH system are listed in Table 1. The calculated rate constants, as a function of temperature for all reactions, are given in the Supporting Information.

Temperature- and pressure-dependent rate constants are calculated using the multichannel, multifrequency QRRK analysis for $k(E)$ with master equation for falloff and stabilization as implemented in the CHEMASTER code.[149] Each well species has a calculated reduced set of three representative vibrations, derived from the full set of $3n - 6$ vibrations, that reproduces the calculated heat capacity, including one external rotation, and they have been shown to compare well to direct count methods.[162] These reduced vibrations, as well as other specific CHEMASTER input parameters, are listed in the Tables S5 and S6.

For correct input into the CHEMASTER program, several well species had to be modified to accurately model the chemical activation product distribution. Table 2 has the modifications made to the high-pressure rate parameters for these well species. In these cases, the well species formed are products (**A1**, **A3**, **A4**, **A8**, **B1**, **B9**, and **B12**), but the cyclic components undergo further reactions to additional products (H, H_2, H_2O, CH_2O, and CH_2OH). Because the cyclic portions of these well species are losing a portion of their available energy, the A′ factor has been decreased by the average difference of the heat capacities, from 300 to 1500 K, of the individual cyclic species to the combined sum of the cyclic component and product in these wells. A detailed description of the procedure for calculating the heat capacity ratio for each of the seven well species is provided in the Supporting Information. Also as seen in Table 2, the A′ factors for the reverse reactions, which are relatively low as seen in Table 1, were set at 1.00×10^{0} to ensure that the reverse reaction would be unfavorable to better represent the chemical activation product distribution. No modifications were done to the n or E_a parameters.

3.2.1. Chemically Activated Processes Involving the RA1 Adduct.* Chemical activation rate constants versus pressure (1 and 100 atm.) and temperature (300 and 1000 K) for generation, isomerization, and dissociation of the **RA1*** chemically activated adduct formed from the combination of the *p*-CMA + OH reagents (Figure 2) are illustrated in Figure 6. Because of the large number of species included in the **RA1** chemical activation analysis, several less favorable species or species whose products are important at elevated temperatures or pressures (pathways represented by dashed lines in Figure 2), including **RA2**, **RA3**, **A1** + H, **A3** + CH_2O, **A4** + H_2O, **A8** + H_2O, **A10** + H, **A11**, and **B7** + H, were removed for clarity. As seen in Figure 2, these channels have relatively high energy barriers. Although there are higher energy barriers, they are entropy-controlled pathways, which are included in Figure 6 such as the formation of **A2**, **A6**, **A7**, and **A9**. These formations become more favorable at increasing temperatures and pressures. The Supporting Information includes the rate constants versus temperature and pressure for all chemical activation **RA1*** species.

Results of the chemically activated kinetic calculations for **RA1*** suggest several favored product formation channels, discussed in Sections 3.1.1 and 3.1.2. In general, for the species included in Figure 6, more favorable conditions are observed at higher temperatures (e.g., 1000 K) across the 0.001−100 atm compared with 300 K with some deviations also being reflected in these figures.

Of the 25 potential products in this **RA1*** chemical activation analysis, the most favorable 16, because of the closeness in the rate constants for several species <500 K, are listed in Tables 3 and 4 for the different temperature ranges. Three separate temperature ranges are considered, <500, 500−1000, and >1000 K at a pressure of 1 and 100 atm because temperature variation showed preference for different species formation. All

https://dx.doi.org/10.1021/acs.jpca.9b11894
J. Phys. Chem. A 2020, 124, 4875−4904

Table 3. Favorable Product Species of RA1* Chemical Activation Reactions Based on Their Calculated Rate Constants (cm^3 mol^{-1} s^{-1}) at a Pressure of 1 atm

<500 K[a]		500−1000 K[b]		>1000 K[c]	
log(k)	species	log(k)	species	log(k)	species
5.860	RA1	3.170	A13 (+OH)	3.373	A13 (+OH)
0.973	RB1	3.080	RB1	2.685	*p*-CMA (+OH)
−0.104	A13 (+OH)	2.535	*p*-CMA (+OH)	2.144	A5 (+H)
−0.914	*p*-CMA (+OH)	1.688	A5 (+H)	1.981	A17 (+H)
−2.734	A2 (+CH_2CH_2OH)	1.462	A17 (+H)	1.728	A2 (+CH_2CH_2OH)
−3.483	A17 (+H)	1.436	A2 (+CH_2CH_2OH)	1.625	A16 (+H)
−3.540	RA2	1.261	A7 + A12	1.608	A7 + A12
−3.671	A4 (+H_2O)	1.049	A16 (+H)	1.345	A6 (+CH_2O)
−4.224	A3 (+CH_2O)	0.951	A6 (+CH_2O)	0.499	A15 (+H)
−4.980	A16 (+H)	0.228	RA1	0.481	A2 (+CH_2=CHOH)
−5.774	A8 (+H_2O)	−0.026	A9 (+OH)	0.316	A9 (+OH)
−6.016	A15 (+H)	−0.133	A2 (+CH_2=CH)	0.258	A2 (+CH_2=CH)
−6.130	A7 + A12	−0.147	A15 (+H)	−0.017	A7 (+CH_2=CHCHO)
−6.798	RA3	−0.182	A2 (+CH_2=CHOH)	−0.607	A7 + A14
−7.008	A5 (+H)	−0.512	A7 (+CH_2=CHCHO)	−0.755	RB1
−7.210	A1 (+H)	−1.150	A7 + A14	−4.526	B7 (+H)

[a]Rate constants provided are from 300 K. [b]Rate constants provided are from 1000 K. [c]Rate constants provided are from 1500 K.

temperature and pressure ranges for chemical activation are presented in the Supporting Information.

The calculated rate constants at representative temperatures of 300, 1000, and 1500 K for these temperature ranges are provided to gauge the important products. As seen in Tables 3 and 4, *p*-CMA (+OH), **RA1**, **RB1**, **A2** (+CH_2CH_2OH), **A5** (+H), **A7 + A12**, **A13** (+OH), **A15** (+H), **A16** (+H), and **A17** (+H) are important products over all of the temperature and pressure conditions analyzed. In general, the chemical activation analysis shows that *p*-CMA (+OH) and the *β*-scission product from **RA1**, **A13** (+OH), are the most important products formed, and these also increase in importance with increasing temperature. The formation of **A2** (+CH_2CH_2OH), via **RA1** and **RA3**, is also another very important route which also shows a slight increase in importance with temperature. **RB1** is another important product. It shows a maximum between 800 and 1000 K at 1 atm but slightly decrease in importance with increasing temperature. The formation, in general, depicts a decrease and general increase, for 300 and 1000 K, respectively, between the 0.001 and 100 atm pressure range. The **A5** (+H) formation via **A4** (roaming dehydration) from **RA1** increases rapidly up through 1000 K. The *β*-scission **RA1** products of **A7 + A12** as well as the products formed from H atom loss from **RA1** and **RA3**, of **A15**, **A16**, and **A17**, increase with temperature to about middle of the list in Tables 3 and 4. **RA1**, as would be expected, shows drastic decreases at 1 atm. compared to 100 atm primarily because of the increasing importance of subsequent products formed from **RA1**. Also, as seen in Figure 6, the formation of **RA1** across the 0.001−100 atm pressure range is favored at the lowest considered temperature (300 K). As will be shown later, the same also occurs in **RB1*** analysis for **RB1**. These products in the *p*-CMA + OH are the most favorable in the chemical activation analysis.

Different species become favorable at points across the three temperature ranges considered. These include **RA2**, **RA3**, **A1** (+H), **A3** (+CH_2O), **A4** (+H_2O), and **A8** (+H_2O) that are also seen to be important under 500 K. As the temperature increases up to 1000 K, **A4** (+H_2O), although decreasing with increasing temperature, is still important, while **A2** (+CH_2=CH, + CH_2=CHOH), **A6** (+CH_2O), **A7** (+CH_2=CHCHO), and **A9** (+OH) are now favorable. Above 1000 K, **A7 + A14** and **B7** (+H) only at 100 atm are at the low levels of the important species. **A11** formation is only favorable below 500 K at 100 atm.

The kinetic analysis is primarily focused on the most important products and intermediates (formed at lowest energies) with an emphasis on the variety of oxygenated compounds resulting from the OH addition, as described in Sections 3.1.1 and 3.1.2. The relevant experimental data are discussed in the context of their kinetic significance.

The main species of interest from experimental data on pyrolysis of *p*-CMA at different conditions mentioned above are gas-phase phenolics, particularly phenol (**B4**, or its precursor radical **A7** in PES), *p*-cresol (**B2**, or its precursor radical **B3**), hydroxy-styrene, aka 4-vinylphenol (**A9**, or its radical **A6**), aldehydes (primarily benzaldehyde, **A2**, and *p*-CMA-aldehyde, **A5**), and various alkyl- and alkenyl-phenols. More complex oxygen-rich compounds, such as 4-(1-hydroxy-2-propenyl)-phenol (**A13**)—an isomer of *p*-CMA, as well as acetophenone, propiophenone, and **BF** derivatives related to **A15**, **A16**, **A17**, **B1**, and **B10** species, are also important in the experimental data. The discussed **BF** formation pathways are also considered.

It should be emphasized that, formation mechanisms of a significant amount of other understudied products are challenging—among others, a variety of oxygenated species, such as 2,3-dihydrodibenzofuran (8.1% at 325 °C), ethanone, 2-(2-hydroxyphenoxy)-1-(3-methylphenyl) (3.6%), acetophenone derivative ethanone, 1-(2,5-dimethylphenyl) (0.7%), and substituted benzopyren (1.2%), PES analysis of the OH + *p*-CMA reaction could explain the formation of some of the nontraditional products—mostly oxygenates. Additional experiments are underway to provide data for the determination of gas-phase elementary reaction mechanisms and identify actual reaction intermediates; these will use shorter resident times and vaporized reagent pyrolysis approach.

3.2.1.1. Chemical Activation Channels (Product Distribution).

https://dx.doi.org/10.1021/acs.jpca.9b11894
J. Phys. Chem. A 2020, 124, 4875−4904

Table 4. Favorable Product Species of RA1* Chemical Activation Reactions Based on Their Calculated Rate Constants (cm^3 mol^{-1} s^{-1}) at a Pressure of 100 atm

<500 K[a]		500−1000 K[b]		>1000 K[c]	
log(k)	species	log(k)	species	log(k)	species
5.860	RA1	3.220	RB1	3.370	A13 (+OH)
−1.027	RB1	3.001	A13 (+OH)	2.683	*p*-CMA (+OH)
−2.104	A13 (+OH)	2.359	*p*-CMA (+OH)	2.143	A5 (+H)
−2.914	*p*-CMA (+OH)	2.278	RA1	1.979	A17 (+H)
−4.877	RA3	1.505	A5 (+H)	1.727	A2 (+CH_2CH_2OH)
−5.285	A2 (+CH_2CH_2OH)	1.278	A17 (+H)	1.622	A16 (+H)
−5.459	RA2	1.259	A2 (+CH_2CH_2OH)	1.605	A7 + A12
−5.483	A17 (+H)	1.043	A7 + A12	1.330	A6 (+CH_2O)
−5.671	A4 (+H_2O)	0.851	A16 (+H)	1.246	RB1
−6.979	A16 (+H)	0.656	A6 (+CH_2O)	0.497	A15 (+H)
−7.769	A8 (+H_2O)	−0.328	A2 (+CH_2=CH)	0.484	A2 (+CH_2=CHOH)
−8.016	A3 (+CH_2O)	−0.340	A15 (+H)	0.255	A2 (+CH_2=CH)
−8.129	A7 + A12	−0.509	A2 (+CH_2=CHOH)	0.247	A9 (+OH)
−8.698	A15 (+H)	−0.572	A4 (+H_2O)	−0.021	A7 (+CH_2=CHCHO)
−10.466	A11	−0.678	A9 (+OH)	−0.609	A7 + A14
−11.007	A5 (+H)	−0.728	A7 (+CH_2=CHCHO)	−2.595	A11

[a]Rate constants provided are from 300 K. [b]Rate constants provided are from 1000 K. [c]Rate constants provided are from 1500 K.

Table 5. Favorable Species of RB1* Chemical Activation Reactions Based on Their Calculated Rate Constants (cm^3 mol^{-1} s^{-1}) at a Pressure of 1 atm

<500 K[a]		500−1000 K[b]		>1000 K[c]	
log(k)	species	log(k)	species	log(k)	species
7.489	RB1	4.664	B1 (+H)	3.884	B10 (+CH_2OH)
−0.572	B10 (+CH_2OH)	4.013	B10 (+CH_2OH)	2.592	*p*-CMA (+OH)
−0.650	RA1	4.009	B3 + B11	1.635	B3 + B11
−1.238	RB3	3.849	B13 (+H)	1.358	B1 (+H)
−1.678	*p*-CMA (+OH)	3.196	RB1	1.284	B13 (+H)
−3.270	B3 + B11	3.035	A7 (+CH_2=CHOH)	0.240	A4 (+H_2O)
−3.740	B9 (+CH_2O)	2.796	*p*-CMA (+OH)	0.057	A7 (+CH_2=CHOH)
−3.839	B1 (+CH_2OH)	1.715	B9 (+CH_2O)	−0.772	B8 (+OH)
−5.091	B13 (+H)	0.250	RA1	−3.144	B7 (+H)
−6.924	A4 (+H_2O)	−0.182	A4 (+H_2O)	−3.475	RB1
−7.576	RB2	−1.530	B8 (+OH)	−3.794	B5 (+H_2O)

[a]Rate constants provided are from 300 K. [b]Rate constants provided are from 1000 K. [c]Rate constants provided are from 1500 K.

Table 6. Favorable Species of RB1* Chemical Activation Reactions Based on Their Calculated Rate Constants (cm^3 mol^{-1} s^{-1}) at a Pressure of 100 atm

<500 K[a]		500−1000 K[b]		>1000 K[c]	
log(k)	species	log(k)	species	log(k)	species
7.489	RB1	3.945	RB1	3.884	B10 (+CH_2OH)
−2.572	B10 (+CH_2OH)	3.084	B10 (+CH_2OH)	2.592	*p*-CMA (+OH)
−2.650	RA1	1.893	*p*-CMA (+OH)	1.642	B3 + B11
−3.235	RB3	1.217	RA1	1.360	B1 (+H)
−3.678	*p*-CMA (+OH)	0.887	B3 + B11	1.284	B13 (+H)
−5.433	B3 + B11	0.764	B1 (+H)	0.239	A4 (+H_2O)
−6.018	B1 (+CH_2OH)	0.539	B13 (+H)	0.113	A7 (+CH_2=CHOH)
−6.572	RB2	−0.566	B9 (+CH_2O)	−0.775	B8 (+OH)
−7.731	B9 (+CH_2O)	−0.650	A7 (+CH_2=CHOH)	−1.387	RB1
−8.924	A4 (+H_2O)	−1.013	A4 (+H_2O)	−3.148	B7 (+H)
−9.081	B13 (+H)	−2.139	B8 (+OH)	−3.797	B5 (+H_2O)

[a]Rate constants provided are from 300 K. [b]Rate constants provided are from 1000 K. [c]Rate constants provided are from 1500 K.

1. The initially preferred species from RA1*-adduct are RA1, RB1, A13 (+OH), and *p*-CMA + OH for temperatures below 500 K at 1 and 100 atm. As the temperature increases from 500 K up past 1000 K at these pressures, RA1 and RB1 formation decreases while A13 and *p*-CMA + OH are still significant.

https://dx.doi.org/10.1021/acs.jpca.9b11894
J. Phys. Chem. A 2020, 124, 4875−4904

2. Channel III.

The formation of 4-(1-hydroxy-2-propenyl)phenol (**HPP**), HOPhCH(OH)CH=CH_2 (**A13**) + OH via β-scission of **RA1**, over a 25.26 kcal/mol barrier through **TSa16**, in *Ch*III is predicted to be one of, if not the most, important paths over the studied temperatures and pressures in the **RA1*** analysis. In Figure 6, it is seen that the rate constant gradually increases with temperature, which also occurs over the 300−2100 K range for the 0.001−100 atm pressures considered in our analysis. This pathway is the second lowest energy from **RA1** to **RB1** formation over **TSmig** (22.07 kcal/mol) and in direct comparison to reformation of **CR1** over **TSa0** (26.63 kcal/mol). This is the fastest process triggered from **RA1** with the only initial barrier to form a product, below the entrance level by 3.35 kcal/mol. Note that later in our **RA1** isomerization and dissociation analysis (Figure 9), it is shown that the preference of **A13** + OH and **RB1** formations are preferred as well over other pathways.

Figures 6−8 and Tables 3−6 illustrate data for similar important reactions of isomerization of (to **RB1**) and β-scission (**A13** + OH) that occur for **RB1** conversion to **RA1** and **B10** + CH_2OH. It is seen, and discussed fully later, that these are important competing reactions for **RB1*** below. The rate constant patterns of isomerization to **RA1**/**RB1** are optimal between roughly 500 and 1200 K, while β-scission to **A13**/**B10** increases with temperature. The low-energy **TSmig** barrier at lower temperatures is important as a competing reaction for β-scission.

We note that the product **A13** per se is not identified in both fractional and conventional experiments with *p*-CMA at 400 °C and above, this could be related to its higher reactivity. Some uncertainty in identification of complex mixtures is inevitable, as it occurs with disputed identification of pyrolytic **BF** versus 4-vinyl phenol with close GC−MS characteristics (*vide infra*), one could expect the overlap of the **A13** spectra with that from its isomers, particularly from recovered *p*-CMA. Intriguingly, 2,3-dihydro-2-methyl-benzofuran product identified in fractional pyrolysis (8.1% at 350 °C)[21] could also represent 4-(1-hydroxy-2-propenyl)phenol—product **A13** with similar structural features.

We note that a keto-derivative (HOPhC(=O)CH=CH_2, **HPP**) of product **A13** and another α-hydroxy derivative (HOPhCH(OH)CH_2CH_2OH, **HPPD**) are among the key products of lignin pyrolysis.[14,43,47] There is another **HPP** precursor, **A8**, as well on the PES of *p*-CMA + OH (Figure 2) generated via **TSa7**, which will be discussed below.

3. Channels Ia, IIc, and XIV″b.

Aldehydes are the major products in pyrolysis of lignin, its model compounds, and monomers under various conditions.[13,23,24] Hydroxy-benzaldehyde (**A2**) observed in pyrolysis of *p*-CMA[23,24] can be formed via several reaction pathways (*Ch*Ia, *Ch*IIc, and *Ch*XIV″b) involving isomerization through **TSa4**, **TSa2**, and **TSa9** transition states followed by various transformations.

A simple way to create an aldehyde group from *p*-CMA attached to the benzene ring at the C4-position is OH addition to the α-C atom of the side chain to form **RA1**, which further dissociates via *Ch*Ia (eqs 1 and 1a).

$$\text{HOPhCH(OH)CH}^{\bullet}\text{CH}_2\text{OH (RA1)} \rightarrow \text{HOPhCH(O}^{\bullet}\text{)CH}_2\text{CH}_2\text{OH (RA3)} \quad (1)$$

$$\text{RA3} \rightarrow \text{HOPhHCO (A2)} + \text{CH}_2\text{CH}_2\text{OH} \quad (1a)$$

The formation of **A2** + CH_2CH_2OH also becomes more favorable as temperature and pressure are increased. This product formation occurs in two steps (see, Section 3.1.1): first involves the 1,3-hydrogen atom shift of **RA1** to **RA3** over the 31.69 kcal/mol energy barrier (**TSa3**) followed by a low-energy (7.71 kcal/mol **TSa4**) carbon−carbon bond breaking to the **A2** + CH_2CH_2OH products. These products are 18.35 kcal/mol below the initial entrance channel.

4-Hydroxylbenzaldehyde (**A2**) can also be formed via other less significant channels *Ch*IIc and *Ch*XIV″b only above 500 K in Tables 3 and 4. The losses of CH_2=CH from **A8** and CH_2=CHOH from **A1**, as seen in Figure 2 are above the entrance channel by 1.15 and 10.05 kcal/mol, respectively, and are slower processes as seen in the rate constants in Figure 6a,b.

Decomposition of **A8** (a precursor of **HPP**, *vide supra*) generated via **TSa7** (eq 8) can breakdown into **A2** as described above, as well as form phenolic radical (**A7**) and acrolein (CH_2=CHCHO) via **TSa8**. The barrier heights for these reactions, 14.90 and 19.17 kcal/mol, respectively, correlate to the calculated rate constants in Tables 3 and 4 with the lower energy barrier pathway favorable.

The kinetics for reactions *p*-CMA + OH show relatively slow formation of benzaldehyde (Figure 6) relative to **RA1**, **RB1**, and **A13** at temperatures below 500 K. This is in agreement with experiments, where the detected amount of pure hydroxybenzaldehyde in fractional pyrolysis, constitutes only 0.9%, in accord with literature data (0.34%).[25] However, larger amounts of other benzaldehyde derivatives are also formed during pyrolysis (e.g., 4.9% at 425 °C, Table 1, ref 21).

Channel II also involves the generation of the α-hydroxy derivative of coumaraldehyde (**A1**) and H atom through the loss of a H atom from the Cγ-position of **RA2**—*Ch*IIb. Note that it is another β-hydroxy isomer—(**B13**), that is formed from the **RB1** adduct.

4. Channel IVa.

One of the major focal points of Part I in our analysis involves OH roaming dehydration transition states and their ability to offer lower energy barriers for *p*-CMA + OH reactions.

Both the dehydration of α-OH (roaming) and dehydration of γ-OH (conventional) are important kinetic pathways for **RA1** as seen in Tables 3 and 4 below 500 K with 33.52 (**TSa5**) and 35.34 (**TSa7**) kcal/mol energy barriers, respectively.

$$\text{RA1} \rightarrow \text{TSa5 (roaming + 4.91 kcal/mol)} \rightarrow \text{A4} \rightarrow \text{A5}$$
$$(p\text{-CMA-aldehyde}) + \text{H} \qquad (5 \text{ and } 5a)$$

For comparison, the energy barrier for conventional dehydration from **RB1** to the same **A4** + H_2O products is about 10 kcal/mol higher than **RA1** over **TSb5** (46.38 kcal/mol).

A4 is a key radical intermediate identified in our earlier study on H + *p*-CMA [denoted as R(O9)].[21] Chemical activation shows that **A4** from **RA1*** is important below 500 K but decreases in importance with increasing temperature as seen in Tables 3 and 4. From **RB1***, the **A4** formation is among the lowest of the important intermediates, but the rate constants increase with increasing temperatures as seen in Tables 5 and 6.

The chemical activation analysis <500 K, Tables 3 and 4, does show slight preference toward **A4** formation versus **A8**, as well as subsequent **A5** + H as favorable product formation from **A4**. As temperature increases, **A4** and **A8** drop off in preference

https://dx.doi.org/10.1021/acs.jpca.9b11894
J. Phys. Chem. A 2020, 124, 4875−4904

in favor of A5/A6 and A2/A7 product formation with a preference for the former as seen in Figure 6a,b.

Intriguingly, no *p*-coumaraldehyde [A5, 3-(4-hydroxyphenyl)-2-propenal] was detected in our fractional pyrolysis experiments.[21] This is explained by its possible rapid secondary transformations typical for fractional pyrolysis (particularly surface-mediated reactions). It is noted that the same phenomenon has been observed by Akazawa at (400−600 °C) from conventional pyrolysis of *p*-CMA. Akazawa detected only small amounts of benzaldehyde (cf. Figure 3 and Table 1 of ref 24, where *p*-CMA is labeled as M2). This suggests a possible rapid degradation of the generated *p*-coumaraldehyde in conventional pyrolysis conditions.[24,25] Notably, the *p*-coumaraldehyde was not detected also from the lignin pyrolysis itself, unlike some other vastly present monomer-aldehydes such as CFA-aldehyde, SPA-aldehyde, and substituted benzaldehydes.[11] This is also in contrast to our conventional CnA-pyrolysis results,[22] where cinnamaldehyde constitutes a major product, spanning the large temperature range of 400−800 °C.

A priori, the presence of a phenolic OH group sterically hindered by a proximal methoxy substituent could be the reason for such a striking difference in reactivity of *p*-CMA-aldehyde versus CFA- and SPA-aldehydes. These aldehydes involve strong H-bonding between OH and methoxy groups to prevent the QM formation and a bare CnA-aldehyde, lacking a phenolic OH. The reactivity of an aldehyde could be increased when it contains a sterically not hindered phenolic OH group. Thus, CFA-aldehyde and SPA-aldehyde consistently constitute major products, whereas *p*-CMA-aldehyde is consistently absent in both our[21−23] and others' experiments (Kawamoto[18] 200−350 °C; Akazawa;[24] Harman-Ware[29] at 650 °C; Masuku[109] at 200−275 °C). The *p*-CMA-aldehyde formation is, however, feasible as predicted by theory[22] with no rate constants being reported (*vide infra*).

The high reactivity of aldehydes with species such as OH radicals is well known, even at low temperatures, and well-studied on simple models (primarily for reactions OH + CH_2O and acetaldehyde[96−98,164−167]). The preferred reaction here is the abstraction of aldehydic H atom, leading to negative activation energy (NTC phenomenon), as opposed to the OH + olefins reactions,[117−119] whereas the addition-barrier to C═O bond is considerable (5−15 kcal/mol).

Note also that *p*-CMA-aldehyde can hardly be formed at low temperatures via often postulated concerted molecular dehydrogenation because of the high barrier of activation; the calculated barrier for cinnamaldehyde dehydrogenation, for instance, is as high as 79 kcal/mol.[22]

The R(O9)−A4 radical, the precursor of *p*-CMA-aldehyde radical A5, can be generated via bimolecular H-abstraction by a pool radical (a detailed account will be reported elsewhere).

5. Channels IIa, IVb, and X.

Another typical product of the *p*-CMA pyrolysis is 4-vinylphenol (A9, 4-hydroxystyrene, 4VP) and its derivatives are produced here via *Ch*IIa and *Ch*IVb, as well as *Ch*X from activated RB1* channels—*vide infra*. Direct production of A9 (+OH) from *Ch*IIa via A3 + CH_2O (eqs 2a and 2b) becomes more important at higher temperatures as seen in Tables 3 and 4.

In addition direct production, 4VP can also be formed from pathways generated by OH + *p*-CMA, such as dehydration of the RA1-adduct via direct H-abstraction or addition−elimination reaction involving a roaming channel *Ch*IVb via TSa5 and decomposition of A4 (Figure 2), albeit to a lesser amount. A similar increasing production of A6 (+CH_2O) from *Ch*IVb via A4 + H_2O (eq 5b) and A4 + H_2O from RB1 in *Ch*X serve as precursors to A9 production as was outlined in Sections 3.1.1 and 3.1.2.

4-Vinylphenol can also be formed from A6 precursor with the addition of an H atom from a donor where a competing dissociation requires higher energy of 44.0 kcal/mol energy (eq 5c) in Figure 2.

The modest reaction rates for the formation of A5/A6 via these channels suggests dominant production of 4-vinylphenol at higher temperatures, as observed in the fractional pyrolysis experiments.[21] A significant amount of unsubstituted styrene was observed at 900 °C along with BTX components benzene and toluene, suggesting the effective truncation of 4VP during pyrolysis.[21] Although no 4-vinylphenol was identified in fractional pyrolysis below 500 °C temperatures,[21] it is the most abundant product of the conventional pyrolysis of *p*-CMA even at lower temperatures (400 °C)[24] probably because of the condensation processes and surface-mediated conversions attributed to the fractional pyrolysis.[21] Notably, the OH + styrene product set is fairly fast ($k = 5.8 \times 10^{11}$ cm^3 $molecule^{-1}$ s^{-1} at 298 K) where the addition of OH occurs to the vinyl carbons of the styrene molecule,[95] to account for such reactions.

The formation of significant amounts of 4-vinylphenol in conventional conditions[24] can be explained by faster H + *p*-CMA reactions as suggested in ref 21 based on PES cross sections and confirmed by corresponding rate constant calculations by Furutani et al.[26]

6. Channel Ib.

3,4′-Dihydroxypropiophenone HOPh(C═O)CH_2CH_2OH (A15) is another species which chemical activation has predicted to be consistent across all temperatures and pressures in Tables 3 and 4. A15 is also a key product in pyrolysis of lignin and other models.,[14,26,47] known as 3-hydroxy-1-(4-hydroxyphenyl)propan-1-one, HHPP. This product formation shows rate-constant trends similar to other H atom elimination products, A5, A16, and A17, where increasing temperature correlates to increasing rate constants and importance for RA1* chemical activation.

As seen in Figure 2, the formation of A15 can occur in the *Ch*I pathway according to eq 1b where the H atom is eliminated from RA3, over a 15.23 kcal/mol TSa20 transition state.

$$\text{RA3} \rightarrow \text{HO-PhC(=O)CH}_2\text{CH}_2\text{OH (A15)} + \text{H} \qquad (1b)$$

Related to A15 products with C═O group in the α-position (Figure S2a in ref 21) are derivatives of acetophenone, PhC(═O)CH_3, observed in fractional pyrolysis experiments—described as ethenone-derivatives in Table 1 ref 21. At 500 °C, some 4-hydroxy-2-methyl-acetophenone is also formed, whether originated from 2,3-dihydro-BF present at 350 °C or via a separate channel.

7. Channels Ic, VI, XIV′, and XIV″.

Phenol (B4) is a major and most common product of lignin-monomer pyrolysis. 19.2 and 10.5% unsubstituted phenol was enumerated in fractional pyrolysis of *p*-CMA at 325 and 425 °C, respectively.[24] B4, along with its *para*-hydroxyphenyl radical A7 (*p*-HOPh$^\bullet$). It is formed via several, typically higher energy, channels *Ch*XIV′, *Ch*XIV″, and *Ch*VI.

https://dx.doi.org/10.1021/acs.jpca.9b11894
J. Phys. Chem. A 2020, 124, 4875−4904

The *Ch*Ic channel is a kinetically important pathway involving A7 precursor radical (*p*-HOPh$^{\bullet}$) formation through C6−C7 bond dissociation. It involves a hydrogen shift in **RA1** to **RA3** over **TSa3** (31.69 kcal/mol) and then to a carbon−carbon bond dissociation over **TSa19** (25.27 kcal/mol) to form **A7** + **A14** which, overall, is less than 1 kcal/mol below the *p*-CMA + OH entrance channel.

$$\mathbf{RA3} \rightarrow \mathrm{HOPh}^{\bullet}\ (\mathbf{A7}) + \mathrm{CHOCH_2CH_2OH}\ (\mathbf{A14}) \qquad (1c)$$

The aforementioned *p*-CMA conventional dehydration *Ch*VI channel over **TSa7** (35.34 kcal/mol) followed by bond C1−C7 breaking over **TSa8** (19.17 kcal/mol) is an added pathway to form **A7** + CH_2=CHCHO (eq 8a) as well.

New alternative pathways have also been considered for **A7** formation in our analysis, including a *β*-scission side-chain reaction *Ch*XIV′, where **RA1** undergoes *β*-scission of C*α*, creating phenol radical (**A7**) and CH(OH)=$CHCH_2OH$ (**A12**) over **TSa15** with a barrier height of +39.05 kcal/mol. Although this is a relatively high-energy process with an overall energy of +10.44 kcal/mol above the entrance channel, chemical activation predicts this to be a very significant path across all temperatures and pressures analyzed, as seen in Figure 6a,b. Above 500 K, **A7** + **A12** formation is near the top of the lists in Tables 3 and 4. It is important to note also that the overall energy of +10.44 kcal/mol is similar to the **A7** + CH_2=CHCHO product formation from **A8** at +8.41 kcal/mol in *Ch*XIV″. Finally, as will be seen in the **RB1*** analysis, **A7** + CH_2=CHOH (*Ch*VI) can be formed at a much higher overall energy of +26.48 kcal/mol above the entrance channel over **TSb15**. This pathway is shown to be important at temperatures about 500 K for **RB1***.

A competitive reaction could also occur via *Ch*IV through the further loss of C_2H_4 from **A6**.[21] The oxygen-centered radical **A4**−R(O9) is an alternative source of the phenol precursor radicals **A7** because of its achievable defragmentation to form 4-hydroxyphenylvinyl radical **A6** ($\Delta E^{\#}$=24.5 kcal/mol) and subsequent acetylene elimination ($\Delta E^{\#}$=44.0 kcal/mol).[21]

The overall reaction from dehydrated *p*-CMA would be **A4** → **A6** + CH_2O → HOPh$^{\bullet}$ (**A7**) + C_2H_4.

Thus, the *stepwise* pathway through two consecutive barriers of 24.5 and 44.0 heights, respectively, is preferred energetically over the direct **A4** → **A7** process, which encounters a significantly higher barrier of 68.6 kcal/mol.[21]

This variety of **A7** formation pathways is of significant importance. Nevertheless, the simple phenol is a major product of *p*-CMA pyrolysis, which can also be formed from further decomposition of substituted primary products. Its production is easier from the *p*-CMA + H reactions.[21] The **A7** (HOPh$^{\bullet}$) radical with an open (free radical) para-position will obviously also serve as a precursor to form mixed phenolic compounds substituted at C4-position observed in experiments, such as *para*-hydroxybiphenyls (1.7%) and various dimerization products (∼5%).[21]

8. Channels IIb, II′, XIII, and XII.

Nontypical product formation channels include the formation of *α*-hydroxy-derivative of *p*-CMA-aldehyde (**A1**) via *Ch*IIb and *Ch*II′ and H-replacement products **A16** and **A17** from channels *Ch*XII and *Ch*XIII, respectively.

These are mostly oxygenated products, which can serve as intermediates to produce simpler homologues. Channels XII and XIII are direct decomposition channels involving energized **RA1*** adduct to provide formation mechanisms for (**A16**) and (**A17**) unsaturated 1,3-diols.

The formation mechanisms are challenging for a significant amount of other understudied products also identified in experiments—among others, a variety of oxygenated species such as 2,3-dihydrodibenzofuran (8.1% at 325 °C), ethanone, 2-(2-hydroxyphenoxy)-1-(3-methylphenyl) (3.6%), acetophenone derivative ethanone, 1-(2,5-dimethylphenyl) (0.7%), and substituted benzopyren (1.2%), PES analysis of OH + *p*-CMA reaction could explain the formation of diverse oxygenates.

Additional experiments are underway to determine gas-phase elementary reaction mechanisms and identify actual reaction intermediates using shorter residence times and *vaporized* reagent pyrolysis approach.

*3.2.2. Chemically Activated Processes Involving the **RB1*** **Adduct.** As described above, the well depth for the **RB1***-activated adduct radical is significantly deeper than that for **RA1***, meaning it can be formed with significantly more excessive energy to react further. However, the isomerization barriers are somewhat higher than those originating from **RA1***. In contrast to **RA1***, the PES for **RB1*** in Figure 3 depicts several barriers located below the entrance level, suggesting access to higher energy for fast processes comparatively speaking.

Chemical activation rate constants versus pressure (1 and 100 atm) and temperature (300 and 1000 K) for generation, isomerization, and dissociation of the stabilized **RB1***-activated adduct are illustrated in Figures 7 and 8. As was done with the **RA1*** analysis, several less favorable species (relatively higher energy barriers as seen in Figure 3) including **B1** + HCO, **B2** + CO, **B4** + CH_2=C=O, **B5** + H_2O, **B6** + H, **B7** + H, **B12** + H_2, and **A7** + CH_2=CHOH were removed for clarity. The Supporting Information includes the rate constants versus pressure and temperature for all chemical activation **RB1*** species.

A similar chemical activation analysis was completed for **RB1*** but with a smaller number of reported species in Tables 5 and 6 because of a large range in variety of the calculated rate constants, under the same temperature ranges. The dominating product formation across all temperature and pressure ranges are *p*-CMA (+OH), **RB1**, **B3** + **B11**, **B10** (+CH_2OH), **B13** (+H), and **A4** (+H_2O). As was seen with **RA1***, *p*-CMA + OH increases in preference with increasing temperatures, increasing more at 100 atm compared to 1 atm, where it drops slightly in the 500−1000 K range.

The highest rate process over the entire temperature and pressure range, relating to the most important species formed, are the *β*-scission of **RB1** forming **B10** (+CH_2OH) and the eventual formation of **B3** + **B11** via **RB2**. **B13** formed from the loss of a hydrogen from C9 of **RB3** is also an important product, which increases with temperature. **A4** (+H_2O) formed from the dehydration of **RB1** is one of the lesser of the important species formed but does slightly increase over this temperature range. Finally, as was also seen in **RA1**, the formation of **RB1** decreases over these temperature ranges because of increasingly important subsequent reaction steps of the **RB1** formed.

As was noted for **RA1***, there are various conditions where additional species are important. The **RB1** isomers, **RB2**, **RB3**, and **RA1**, as well as **B1** (+CH_2OH) are important species, primarily below 500 K, in addition to the above preferred products. As the temperature increases, their formation decreases as the other pathways from these primary products increase in importance. These four species have consistent rate

https://dx.doi.org/10.1021/acs.jpca.9b11894
J. Phys. Chem. A 2020, 124, 4875−4904

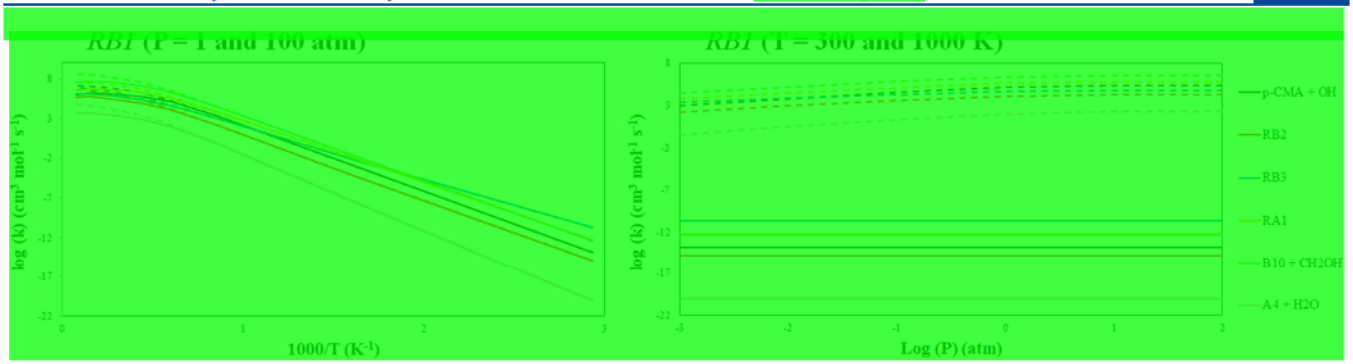

Figure 10. Rate constants vs pressure (1 and 100 atm, solid and dashed lines, respectively) and vs temperature (300 and 1000 K, solid and dashed lines respectively) for RB1 isomerization and dissociation reactions.

constants from 300 K up to about 1000 K at which point they fall off. Also, as the temperature increases, **B9** ($+CH_2O$) formation is important below 1000 K, but not above this temperature as shown in Figures 7 and 8. **B1** (+H), **B8** (+OH), and **A7** ($+CH_2$=CHOH) are shown not to be important below 500 K but are increasingly important as the temperature increases. **B1** (+H) is the most preferred species between 500 and 1000 K at 1 atm as well as one of the most preferred above 1000 K at 100 atm. Finally, **B5** ($+H_2O$) and **B7** (+H) occupy the lower range of the more important species list above 1000 K at both 1 and 100 atm.

3.2.2.1. Chemical Activation Channels (Product Distribution).

1. The initially preferred species from the **RB1*** adduct are *p*-CMA + OH, **RB1**, **RB3**, **RA1**, and **B10** + CH_2OH for temperatures <500 K at 1 and 100 atm. As the temperature increases, the rate constants for **RB1** and **RA1** are consistently large up to about 1000 K while **RB3** drops quickly. On the other hand, the rate constants for *p*-CMA + OH and **B10** + CH_2OH are consistently the highest in the **RB1*** analysis. Like **RA1**, the isomerization and dissociation analysis of **RB1** shows preferred formation of **B10**, **A4** (via roaming and conventional dehydrations), and **RB2** (leading to **B3** + **B11** and **B1** + CH_2OH) as seen in Figure 10.

2. Channel IX.

The β-scission reaction of **RB1** over **TSb13** to form 4-hydroxyethenyl phenol, HOPhCH=CH−OH (**B10**) + CH_2OH is the fastest, or second highest process, process as seen in Tables 5 and 6. It is within 2 kcal/mol of the barrier energy to that of **RA1** formation over **TSmig**, which is also an important pathway. However, as seen in Figure 8, the formation of **RA1** is optimal between 500 and 1200 K where, in contrast, **B10** formation increases with the temperature. The preference for **RB1** formation over **TSmig** is also seen in comparing these rate constants.

The isomerization and dissociation of **RB1** in Figure 10 shows that the rate constants for **B10** formation are preferred over the temperatures 500−2100 K for 1 and 100 atm as well as at 1000 K from 0.001 to 100 atm. For the β-scission **RB1** → **B10** + CH_2OH reaction over **TSb13**, which is 4.89 kcal/mol below the entrance channel, this helps to explain why this pathway is important to **RB1***.

The β-scission of **RB1** between the Cβ−Cγ bond has a barrier height of 36.31 kcal/mol over **TSb13** to create 2-(4-hydroxyphenyl)ethenol HOPhCH=CHOH (**B10**) and a reactive CH_2OH radical. Chemical activation analysis predicts that this is the fastest reaction initiated from **RB1** to products with the barrier 4.89 kcal/mol below the entrance level, which would trigger further chain reactions. Across all temperatures and pressures in Tables 5 and 6, this formation is paramount.

Intriguingly, the simple structure of the (**B10**), HOPhCH=CH−OH, is not listed in the NIST database among compounds with molecular formula $C_8H_8O_2$. The product **B10** has also not been identified in pyrolysis experiments, rather its structural varieties are highlighted. Perhaps, it could be converted at applied temperatures and resident times to form **BF**, acetophenone derivatives, or other compounds observed in experiments; some mechanistic analysis for such reactions are provided later on.

3. Channel X.

As a typical product, *p*-CMA-aldehyde (**A5**) can be formed also via Channel X from **RB1** via dissociation of **A4**-intermediate. As was seen with **RA1**, dehydration reactions are kinetically important to the *p*-CMA + OH reaction scheme presented. In contrast to **RA1** involving a roaming-like **TSa5**, dehydration of **RB1** to form **A4** + H_2O via **TSb5** includes only a conventional dehydration barrier located 5.18 kcal/mol above the entrance level (**TSb5**, 46.38 kcal/mol). Subsequent further decomposition of **A4** over an energy barrier of 16.09 kcal/mol to the **A5** molecule and H atom, as seen in **RA1** dehydration (Figure 2), could then occur. There is an increasing importance of these **RA1** and **RB1** pathways at 1000 K and increasing pressures as shown in Figures 7 and 8. Note that the conventional dehydration via **TSb5** has an energy barrier (5.18 kcal/mol) similar to the transition state corresponding to bimolecular H-abstraction via OH radical.

The energy difference for the **TSa5** and **TSb5**/H-abstraction TST's can be explained by the formation of a strained five-membered ring transition state in both cases, leading to increasing activation energy. By comparison, the 1,3-dehydration of **RA1** involves a more relaxed six-membered ring, **TSa5**, making the activation energy lower at 33.52 versus 46.38 kcal/mol similar to what is seen in the simpler OH + AA model reaction.[24]

4. Channel VIIb.

Isomerization of **RB1*** to form **RB2** over the 39.66 kcal/mol energy barrier for **TSb3** is another preferred reaction pathway via *Ch*VIIb to form the radical precursor of *p*-cresol (**B3**) which is one of the most abundant pyrolysis products. There are two barriers from **RB2**, almost identical in energy, involving the bond dissociations, **TSb4** and **TSb14**, eqs 10a and 10b.

$$\mathbf{RB2} \rightarrow \mathrm{HOPhCH_2CHO}\ (\mathbf{B1}) + {}^{\bullet}\mathrm{CH_2OH} \qquad (10a)$$

https://dx.doi.org/10.1021/acs.jpca.9b11894
J. Phys. Chem. A 2020, 124, 4875−4904

$$\mathbf{RB2} \rightarrow \mathrm{HOPhCH_2^{\bullet}}\ (\mathbf{B3}) + \mathrm{CHOCH_2OH}\ (\mathbf{B11}) \qquad (10b)$$

These competing reactions are both favorable, but chemical activation analysis depicts the reaction through **TSb14** barrier to form **B3** + **B11** (eq 10b) to be slightly preferable at 500 K. This is also seen in **RB2** isomerization and dissociation reactions provided in the Supporting Information. The preference here can be attributed to the approximately 10 kcal/mol energy difference in forming the lower energy products **B3** + **B11** ($CHOCH_2OH$) which are located 28.02 kcal/mol below the entrance channel.

5. Channels VIII and VIa.

The formation of 4-hydroxyphenylacetaldehyde (**B1**), the isomer of **B10**, is detailed as a product in three different pathways in Figure 3. The more feasible, lowest energy, pathway to **B1** is from **RB2**, which is formed directly from **RB1** via **TSb3** (eq 10a). Then, **RB2** can undergo carbon−carbon bond dissociation over **TSb4** at 7.32 kcal/mol to form $HOPhCH_2CHO$ (**B1**) and CH_2OH radical—*Ch*VIII. Because **B1** can be produced via a feasible channel involving low-energy **TSb3** and **TSb4**, it is shown in Tables 5 and 6 to be one of the most favorable products; its formation is initiated by energized **RB1*** to serve as a main source of **B1** and/or a product of its conversion—possibly **BF** or **4VP**?

RB2 can also be formed in an alternative to the above pathway, via **RB3** instead of directly from **RB1**, as seen in eq 12a.

$$\mathbf{RB1} \rightarrow \mathbf{RB3} \rightarrow \mathbf{RB2} \rightarrow \mathrm{HOPhCH_2CHO}\ (\mathbf{B1}) + {}^{\bullet}\mathrm{CH_2OH} \qquad (12a)$$

This pathway involves three steps, transition states of decreasing barrier energy, **TSb1** (32.94 kcal/mol), **TSb2** (15.75 kcal/mol), and **TSb4** (7.32 kcal/mol), all of which are 8−18 kcal/mol below the entrance channel. Chemical activation analysis shows that **RB3** is preferred to **RB2** at < 500 K which can be due to the preference of **B3** + **B11** and **B1** + CH_2OH paths. As seen in Figure 10, **RB1** isomerization and dissociation reactions result in **RB3** being preferred over **RB2**. Reaction **RB3** shows almost equivalent rate constants for the reverse reaction back to **RB1** and **RB2** which is consistent with barrier heights of 15.15 and 15.75 kcal/mol, respectively. Data on **RB2** and **RB3** isomerization and dissociation in the Supporting Information show that the rate constants for **B3** + **B11** and **B1** + CH_2OH are larger than those from **RB1** and **RB2** formation from **RB3** which can conclude that these products can be formed quickly and are in direct competition.

A secondary pathway to **B1** formation is an additional multistep process identified in Part II here, *Ch*VIa, involving the elimination of an H atom from **RB3** according to eq 9b. The Cβ−Cγ bond in **RB3** is broken during this first step over **TSb9** at an energy cost of 16.70 kcal/mol. This creates formaldehyde and $HOPhCH_2CHOH$ (**B9**), which then further react over a larger 34.82 kcal/mol energy barrier, representing the loss of the H atom from the terminal hydroxyl group creating **B1**.

$$\mathbf{RB3} \rightarrow \mathrm{HOPhCH_2CHOH}\ (\mathbf{B9}) + \mathrm{CH_2O} \rightarrow \mathrm{HOPhCH_2CHO}\ (\mathbf{B1}) + \mathrm{H}\ (+\mathrm{CH_2O}) \qquad (9b)$$

B9 can also undergo β-scission to form *para*-hydroxyphenyl radical (**A7**) and vinyl alcohol (CH_2=CHOH) over **TSb15** with an energy requirement of 40.67 kcal/mol depicted in eq 9e. Chemical activation of **RB1*** shows that this pathway is not favorable below 500 K, but an increase in preference with increasing temperature is seen in Tables 5 and 6.

The last pathway for **B1** formation is from **RB2** but involves H atom abstraction of a C9 H atom by the terminal hydroxyl H atom, creating **B12** + H_2 over **TSb8**. The calculated energy barrier is 106.00 kcal/mol (81.39 kcal/mol above the entrance channel) followed by subsequent loss of HCO from **B12** to yield **B1**. As seen in the Supporting Information, this pathway, although theoretically possible, is unfavorable across all temperatures and pressures studied here.

Neither **B1** nor **B10** are observed experimentally despite being the most possible pathways from theory. They both are reactive species, especially **B1** containing a labile benzylic α-proton. They most likely undergo further transformations, primarily, condensation to end up in char residues or converted to other products such as **BF**. **B1** is an important (and most intriguing) product because it can be converted to **BF**, which is observed both in fractional and *vaporized* experiments under different experimental conditions. The possible conversion paths to **BF** will be discussed below.

Another less stable isomer of **B1**, apart from **B10**, is styrene oxide (**StO**, aka hydroxyphenyl oxirane), which is higher in energy than two others by about ca. 20 kcal/mol above **B1**. It is known to be reactive and accompanied by polystyrene oxide polymer. Styrene oxide can be formed from both **B1** (phenylacetaldehyde) and **B10** isomers involving a biradical intermediate.

6. Note that the formation of oxirane and oxetane derivatives in this reaction system encounter much higher barriers involving **TSb11**, **TSb12**, **TSa13**, and **TSa14** in Figures 2 and 3; thus, they are directly formed in negligible amounts. They are not observed experimentally even at high temperatures where the formation of simpler BTX-compounds is preferred.[21]

7. Channel XI.

Another nontypical oxygenated product is the β-hydroxy-derivative of *p*-CMA-aldehyde (**B13**) formed via *Ch*XI, which is the isomer of a product (**A1**) described above. The formation of **B13** via loss of a hydrogen from the Cγ atom of **RB3** occurs over a 19.87 kcal/mol energy barrier (**TSb17**) as seen in eq 9d. Data in Tables 5 and 6 show that this product is at the lower end at temperatures <500 K. This product is at the lower end of the list, but quickly increases with temperature.

$$\mathbf{RB3} \rightarrow \mathrm{HOPhCH_2CH(OH)CHO}\ (\mathbf{B13}) + \mathrm{H} \qquad (9d)$$

8. The least significant reaction pathway for **RB1*** at mild conditions (>500 K) is loss of the γ-OH over **TSb6** with an energy barrier of 53.79 kcal/mol to form **B8** with a cyclopropane side chain. Forming a three-membered ring is the reason for the high energy barrier, but in comparison to the three- and four-membered oxygen-containing rings formed in **TSb11** and **TSb12** with an accompanying 15 kcal/mol energy increase, this is feasible. **B7** + H is predicted to become increasing possible at >1000 K, as seen in Tables 5 and 6.

9. Alkyl and alkenyl phenols are also major products in *p*-CMA fractional pyrolysis. H atom addition to the double bond (instead of OH addition) can contribute to the low temperature formation of products with hydrogenated side chains, such as 4-ethyphenol, 4-propylphenol, 4(2-)propenyl phenol, and dihydro-*p*-CMA, as is detailed in ref 21.

https://dx.doi.org/10.1021/acs.jpca.9b11894
J. Phys. Chem. A 2020, 124, 4875−4904

10. Several important low-molecular weight "byproducts", along with the reactive radicals H, OH, and CH_2OH, are also formed in the frame of OH + *p*-CMA reaction schemes developed in this study. Apart from well-recognized products CH_2O, water, vinyl alcohol, and acrolein, some other important compounds such as hydroxypropionaldehyde (known as antibiotic *reuterin*), and glycolaldehyde, which is a key biomass pyrolysis product commonly considered to be originated from cellulose, are also formed. Intriguingly, glycolaldehyde, the coproduct of (**B11**)—*Ch*VIIb, is remarkably easy to form via eq 10b. This suggests an alternative contribution of glycolaldehyde generated from lignin counterpart in biomass pyrolysis, especially if one considers the possible abundance of OH radicals during thermal destruction of biomass.
11. It is important to note that the most reactive species (primarily radicals OH, CH_2OH and H atoms) are chain-propagation and chain-branching agents generated via the fastest elementary reactions to support the above discussion on the radical mechanisms.

A rapid formation of OH via channel *Ch*III is accompanied by the formation of the **A13** product (eq 4). This process is a remarkably effective regeneration channel for OH radicals/reagents.

$$\mathbf{RA1} \rightarrow \mathrm{HOPhCH(OH)CH{=}CH_2}\ (\mathbf{A13}) + \mathrm{OH} \qquad (4)$$

The exchange of H atom with the phenolic OH group in *p*-CMA can also be a source of hydroxyl radicals at higher temperatures (eq 13), as it occurs with phenols (see Introduction).

$$\mathrm{H} + p\text{-CMA} \rightarrow \mathrm{OH} + {}^{\bullet}\mathrm{OPhCH{=}CHCH_2OH} \qquad (13)$$

Furthermore, the removal of phenolic hydrogen (analogous to breaking a β-O-4 linkage in lignin) forms a resonance-stabilized quinoidal radical O=Ph=CH−CH$^{\bullet}$−CH_2OH, which decomposes into conjugated char component O=Ph=CH−CH=CH_2 and an OH radical.

$$\mathrm{O{=}Ph{=}CH - CH^{\bullet} - CH_2OH} \rightarrow \mathrm{O{=}Ph{=}CH - CH{=}CH_2} + \mathrm{OH} \qquad (13a)$$

The active CH_2OH radical is produced via two *Ch*VIII and *Ch*IX main channels to form **B1**/**B10** species—(eqs 9a, 9b, 10a, 10c, and 11). It further decomposes to generate H atoms and formaldehyde.

3.3. Possible Mechanism for BF Formation. BF is one of the most intriguing products identified by GC−MS analysis in experiments on pyrolysis of monomers and other lignin models in various conditions,[11d,21,44,168] including our currently in-progress experiments utilizing vapor-phase monolignols. Some of these are formed at remarkably low temperatures, raising questions. BF-derivatives are also observed in pyrolysis of lignins, albeit at higher temperatures.[116,155,166,170]

The reduced BF derivative, 2,3-dihydrobenzofuran (**DHBF**), resembles some of the cyclic ethers found in lignin and is therefore studied as a model compound to particularly represent the β-5 linkage (see the data-compiled in ref 9 data—Scheme 4 and Table 4). A significant amount of **DHBF** is also identified in our fractional pyrolysis experiments on *p*-CMA at 350 °C (8.1%, Table S2a in ref 21) based on the standard GC−MS analysis, plus a small amount of 4,7-dimethyl-BF detected at 500 °C.[21] Perhaps, one could suggest that 4,7-dimethyl-BF simply originates from higher temperature conversions of **DHBF**. However, such a conversion is not straightforward and involves concomitant hydrogenation and symmetric methylation processes. Therefore, it is also reasonable to expect that these two compounds originate from different sources, via different mechanisms.

There exists controversy in the identification of **DHBF** in lignin pyrolysis.[28,171] Qu et al.[171] and later Kato at al.[28] have particularly found that GC/MS procedures can be misleading because of the closely resembling mass-spectroscopic spectra of **DHBF** and 4-vinylphenol (**4VP**). Furthermore, the isolation and reanalysis of this very major product using NMR and other methods allowed its identification as 4-vinylphenol.

Gas-phase cyclization processes are typically energy-demanding, and one could a priori expect that the formation of **BF** also occurs at higher temperatures similar to what occurs with dibenzofuran (see, e.g., our mechanistic study on generation of DBFs[110]). Thus, the noted above misinterpretation could also concern our experiments with *p*-CMA; therefore, we invoked theoretical calculations to elucidate the possibility of the **BF** formation from the product set of the title reaction. Some additional experiments are also underway, involving vaporized reagents.

The unimolecular concerted pathways for side-chain ring closure to form **BF** proposed in Part I[27] are much too high in energy to account for observed **DHBF** in fractional pyrolysis of *p*-CMA.[21] Similarly, the unimolecular conversion pathways involving the most prevalent products from PES analysis here (Figures 2 and 3) can also be ruled out. Therefore, we focused on the possibility of the lower energy radical pathway to generate **BF** and performed additional B3LYP/6-31g(d,p) level calculations to evaluate the energetics of such processes (an extended report on possible mechanisms will be provided elsewhere).

Our analysis shows that the BF core can be conveniently formed via a common radical of 4-hydroxyphenylacetaldehyde (**B1**) and its higher-energy vinyl-alcohol-type isomer **B10** (Figure 4a) generated via a hydrogen loss from C7- and terminal O-centers, respectively.

$$\mathrm{HOPhCH_2CHO}\ (+\mathrm{R}^{\bullet}) \rightarrow \mathrm{HOPhCH^{\bullet}CHO}\ (\mathbf{B1} - \mathbf{C7j}/\mathbf{B10} - \mathbf{Oj}) + \mathrm{H}\ (\mathrm{RH}) \qquad (14)$$

B1 and **B10** are the dominant products predicted by theory—see, *Ch*IX, *Ch*VII, and *Ch*VIa above, and can principally account for the formation of **BF** (Figure 11).

Dissociation of the labile benzylic H atom (or its abstraction by a radical) in **B1** and the O-bound H atom in **B10** generates a common oxygen-linked radical HOPhCH$^{\bullet}$CHO, referred to as **B1**−**C7j**/**B10**−**Oj** radical, which is technically well suited to undergo a second ring-closure to produce **BF**.

Obviously, the direct dissociation of C−H and O−H bonds of the gas-phase products **B10** and **B1** (BDE = 69.4 and 76.3 kcal/mol at B3LYP/6-31g(d,p) level, respectively) is still too energy-demanding, and the H-abstraction process by a radical is much preferred. Notably, the energy difference between two isomers at B3LYP and CBS-QB3 levels are fairly close to each other (6.93 and 6.02 kcal/mol, respectively) to justify the method choice.

Analysis of the spin distribution in **B1**−**C7j**/**B10**−**Oj** radical confirms its delocalization over the side chain and phenolic ring

https://dx.doi.org/10.1021/acs.jpca.9b11894
J. Phys. Chem. A 2020, 124, 4875−4904

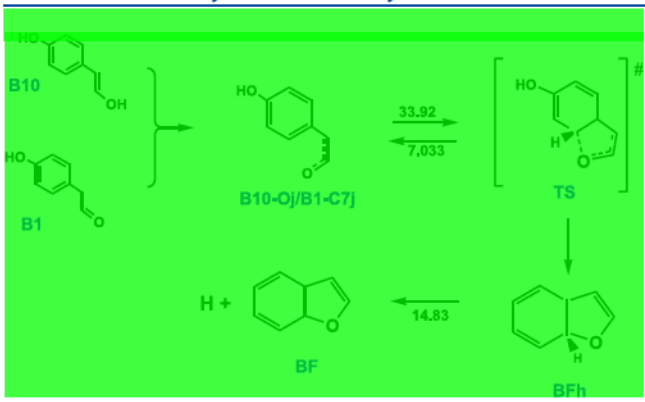

Figure 11. Pathway to BF formation from common radical HOPhCH•CHO of favored products B1 and B10.

to support cyclization. An attack of the terminal O atom of **B1−C7j/B10−Oj** radical (ρO = 0.3e) to orthoring atom (ρC2 = 0.2e) produces an H-capped DB radical **BFh** (Figure 11). The cyclization barrier is 33.72 kcal/mol, which is relatively low, with the reverse reaction barrier being lower at 7.03 kcal/mol. Further decomposition of **BFh** is more feasible at 14.83 kcal/mol at the asymptotic level.

The process can occur more rapidly if the radical **B1−C7j/B10−Oj** is formed via H-abstraction by OH radical to form water, which is exothermic by 42.37 and 35.44 kcal/mol for **B1** and **B10**, respectively. Hence, the theory does not rule out formation of DB depending on conditions.

4. CONCLUSIONS

Currently available kinetic models of lignin pyrolysis—the most complex component of biomass pyrolysis, are lacking decomposition kinetics of monolignols, which are precursor units, early intermediates, and primary products of lignin pyrolysis. The kinetic data provided in this paper suggests a fundamentally based set of reactions and low-temperature product-formation channels for interaction of OH radicals with basic monolignols bearing a typical propanoid side chain—AA moiety (such as *p*-CMA).

Monolignols can interact with various pyrolytic radical species (e.g., H, OH, CH_3) as well as larger chain-carrying radicals to trigger chain reactions. The reactions of OH radicals, however, seem to be the only processes to account for the formation of diverse oxygenated species in oxygen-deficit pyrolytic environments. The reactions with H atoms instead can dominantly generate hydrogen-rich products, such as dihydro-*p*-CMA, dihydro-*p*-CMA-aldehyde, alkyl phenols, as well as account for a feasible formation of a major product 4-vinylphenol, as we have shown previously.[11]

A fundamentally based kinetic analysis is performed, and (p,T)-dependent rate constants are derived from QRRK/master equation analysis on the basis of PES data calculated at the composite CBS-QB3 level.

A significant difference between well depths for the chemically activated adduct radicals **RA1*** and **RB1*** is found (*ca.* 29 and 41 kcal/mol below the OH + *p*-CMA reactants, respectively, at CBS-QB3 composite level) for the α- and β-carbon addition reactions to generate 1,3- and 1,2-diol radicals, respectively, which diversifies the product formation.

Results of the chemically activated kinetic calculations for **RA1*** suggest several favored product formation channels. The calculated rate constants at representative temperatures of 300, 1000, and 1500 K are provided to gauge which products are most important. Particularly, **A2** (benzaldehyde) + CH_2CH_2OH, **A5** (*p*-CMA-aldehyde) + H, **A7** (phenol precursor *para*-hydroxyphenyl radical) + **A12** ($HOCH_2CH_2CHO$, antibiotic reuterin), **A13** (4-(1-hydroxy-2-propenyl)phenol, HPP) + OH, **A15** (acetophenone derivative) + H, **A16** (3-hydroxyphenyl-2-propen-1 2-diol) + H, and **A17** (3-hydroxyphenyl-1-propen-1 2-diol) + H are important products, regardless of temperature and pressure conditions analyzed.

A similar chemical activation analysis was performed for **RB1*** but with a smaller number of species because of a large range in variety of the calculated rate constants. The dominating product formation across all temperature and pressure ranges are *p*-CMA (+OH), **RB1**, **B3** (*para*-hydroxybenzyl radical—precursor of *p*-cresol) + **B11** ($CHO-CH_2OH$, glycolaldehyde), **B10** (4-hydroxyphenyl-vinylalcohol, HOPhCH=CHOH) + CH_2OH, **B13** (β-hydroxy-coumaraldehyde) + H, and **A4** (oxygen-linked radical of *p*-CMA) + H_2O.

The highest-rate processes over the entire temperature and pressure range, relating to the most important species formed are the β-scission of **RB1** forming **B10** + CH_2OH and the eventual formation of **B3** + **B11** via **RB2**. Loss of a hydrogen from C9 and the terminal CH_2OH group of **RB3** forms **B13** (3-hydroxyphenyl-2-hydroxypropionaldehyde) and **B10** (4-hydroxyphenylacetaldehyde, $HOPhCH_2CHO$, **B1**), respectively, that are also important product formations, which increase with temperature. In addition, **B10** and its lowest energy isomer **B1** can suggest a feasible pathway for BF formation.

The results from this comprehensive kinetic analysis can be utilized in detailed kinetics models for biomass pyrolysis, as well as in pyrolysis modeling of substituted aromatic compounds.

Future research assumes the integration of elementary reaction kinetics from this work with previously reported results on H + *p*-CMA, as well as a variety of established unimolecular decomposition and bimolecular H-abstraction reactions into a detailed chemical mechanism to provide a complete (p,T)-dependent kinetic module of monolignols' pyrolysis for modeling of biomass pyrolysis.

■ ASSOCIATED CONTENT

Supporting Information

The Supporting Information is available free of charge at https://pubs.acs.org/doi/10.1021/acs.jpca.9b11894.

Optimized structures, vibrational frequencies, moments of inertia, calculated thermochemical properties, rate constants, CHEMASTER input parameters, chemical activation analysis, isomerization and dissociation analysis, heat capacity ratios, and complete references (PDF)

■ AUTHOR INFORMATION

Corresponding Author

Rubik Asatryan − *Department of Chemical and Biological Engineering, University at Buffalo, The State University of New York, Buffalo, New York 14226, United States;* orcid.org/0000-0003-1200-2727; Email: rubikasa@buffalo.edu

Authors

Jason M. Hudzik − *Department of Chemistry and Environmental Science, New Jersey Institute of Technology,*

Newark, New Jersey 07102, United States; orcid.org/0000-0002-6550-3675

Mohamad Barekati-Goudarzi — *Department of Chemistry, Louisiana State University, Baton Rouge, Louisiana 70803, United States*

Lavrent Khachatryan — *Department of Chemistry, Louisiana State University, Baton Rouge, Louisiana 70803, United States;* orcid.org/0000-0002-8067-7964

Joseph W. Bozzelli — *Department of Chemistry and Environmental Science, New Jersey Institute of Technology, Newark, New Jersey 07102, United States;* orcid.org/0000-0003-4822-150X

Eli Ruckenstein — *Department of Chemical and Biological Engineering, University at Buffalo, The State University of New York, Buffalo, New York 14226, United States;* orcid.org/0000-0001-5192-4922

Complete contact information is available at: https://pubs.acs.org/10.1021/acs.jpca.9b11894

Notes

The authors declare no competing financial interest.

See ref 27 for Part I of this paper including a detailed PES analysis.

■ ACKNOWLEDGMENTS

This work is partly funded by National Science Foundation under Grant CBET 1330311. L.K. acknowledges a partial support from NSF USA grant 1805677. R.A. acknowledges the Ruckenstein Fund at the University at Buffalo (UB) for the continuous support. The computing time on the high-performance computing infrastructure "Rush" was provided by the UB Center for Computational Research and by the NJIT Advanced Research Computing (ARC) center.

■ REFERENCES

(1) van Parijs, F. R. D.; Morreel, K.; Ralph, J.; Boerjan, W.; Merks, R. M. H. Modeling Lignin Polymerization. I. Simulation Model of Dehydrogenation Polymers. *Plant Physiol.* **2010**, *153*, 1332−1344.

(2) Zhou, X.; Broadbelt, L. J.; Vinu, R. Mechanistic Understanding of Thermochemical Conversion of Polymers and Lignocellulosic Biomass In *Advances in Chemical Engineering*; Van Geem, K. M., Ed.; Academic Press, 2016; Vol. *49*, p 95−198.

(3) Kim, K. H.; Bai, X.; Cady, S.; Gable, P.; Brown, R. C. Quantitative Investigation of Free Radicals in Bio-Oil and their Potential Role in Condensed-Phase Polymerization. *ChemSusChem* **2015**, *8*, 894−900.

(4) Sluiter, J. B.; Ruiz, R. O.; Scarlata, C. J.; Sluiter, A. D.; Templeton, D. W. Compositional Analysis of Lignocellulosic Feedstocks. 1. Review and Description of Methods. *J. Agric. Food Chem.* **2010**, *58*, 9043−9053.

(5) Ragauskas, A. J.; Beckham, G. T.; Biddy, M. J.; Chandra, R.; Chen, F.; Davis, M. F.; Davison, B. H.; Dixon, R. A.; Gilna, P.; Keller, M.; et al. Lignin Valorization: Improving Lignin Processing in the Biorefinery. *Science* **2014**, *344*, 1246843.

(6) Carstensen, H. H.; Dean, A. M. Development of Detailed Kinetic Models for the Thermal Conversion of Biomass via First Principle Methods and Rate Estimation Rules. *Computational Modeling in Lignocellulosic Biofuel Production*; ACS Symposium Series; American Chemical Society, 2010; Vol. *1052*, Chapter 10, pp 201−243.

(7) Heitner, C.; Dimmel, D. R.; Schmidt, J. A. *Lignin and Lignans: Advances in Chemistry*; CRC Press, 2010.

(8) Huber, G. W.; Iborra, S.; Corma, A. Synthesis of Transportation Fuels from Biomass: Chemistry, Catalysts, and Engineering. *Chem. Rev.* **2006**, *106*, 4044−4098.

(9) Zakzeski, J.; Bruijnincx, P. C. A.; Jongerius, A. L.; Weckhuysen, B. M. The Catalytic Valorization of Lignin for the Production of Renewable Chemicals. *Chem. Rev.* **2010**, *110*, 3552−3599.

(10) Azadi, P.; Inderwildi, O. R.; Farnood, R.; King, D. A. Liquid Fuels, Hydrogen and Chemicals from Lignin: A Critical Review. *Renewable Sustainable Energy Rev.* **2013**, *21*, 506−523.

(11) Kibet, J.; Khachatryan, L.; Dellinger, B. Molecular Products and Radicals from Pyrolysis of Lignin. *Environ. Sci. Technol.* **2012**, *46*, 12994−13001.

(12) Pelucchi, M.; Cavallotti, C.; Cuoci, A.; Faravelli, T.; Frassoldati, A.; Ranzi, E. Detailed Kinetics of Substituted Phenolic Species in Pyrolysis Bio-Oils. *React. Chem. Eng.* **2019**, *4*, 490−506.

(13) SriBala, G.; Carstensen, H. H.; Van Geem, K. M.; Marin, G. B. Measuring Biomass Fast Pyrolysis Kinetics: State of the Art. *Wiley Interdiscip. Rev.: Energy Environ.* **2019**, *8*, No. e326.

(14) Patwardhan, P. R.; Brown, R. C.; Shanks, B. H. Understanding the Fast Pyrolysis of Lignin. *ChemSusChem* **2011**, *4*, 1629−1636.

(15) Kawamoto, H. Lignin Pyrolysis Reactions. *J. Wood Sci.* **2017**, *63*, 117−132.

(16) Evans, R. J.; Milne, T. A. Molecular Characterization of the Pyrolysis of Biomass. *Energy Fuels* **1987**, *1*, 123−137.

(17) Saiz-Jimenez, C.; De Leeuw, J. W. Lignin Pyrolysis Products: Their Structures and Their Significance as Biomarkers. *Org. Geochem.* **1986**, *10*, 869−876.

(18) Kotake, T.; Kawamoto, H.; Saka, S. Pyrolysis Reactions of Coniferyl Alcohol as a Model of the Primary Structure Formed During Lignin Pyrolysis. *J. Anal. Appl. Pyrolysis* **2013**, *104*, 573−584.

(19) Kotake, T.; Kawamoto, H.; Saka, S. Mechanisms for the Formation of Monomers and Oligomers During the Pyrolysis of a Softwood Lignin. *J. Anal. Appl. Pyrolysis* **2014**, *105*, 309−316.

(20) Kotake, T.; Kawamoto, H.; Saka, S. Pyrolytic Formation of Monomers from Hardwood Lignin as Studied from the Reactivities of the Primary Products. *J. Anal. Appl. Pyrolysis* **2015**, *113*, 57−64.

(21) Asatryan, R.; Bennadji, H.; Bozzelli, J. W.; Ruckenstein, E.; Khachatryan, L. Molecular Products and Fundamentally Based Reaction Pathways in the Gas-Phase Pyrolysis of the Lignin Model Compound p-Coumaryl Alcohol. *J. Phys. Chem. A* **2017**, *121*, 3352−3371.

(22) Khachatryan, L.; Xu, M.-x.; Wu, A.-j.; Pechagin, M.; Asatryan, R. Radicals and Molecular Products from the Gas-Phase Pyrolysis of Lignin Model Compounds. Cinnamyl Alcohol. *J. Anal. Appl. Pyrolysis* **2016**, *121*, 75−83.

(23) Xu, M.-x.; Khachatryan, L.; Baev, A.; Asatryan, R. Radicals from the Gas-Phase Pyrolysis of a Lignin Model Compound: p-Coumaryl Alcohol. *RSC Adv.* **2016**, *6*, 62399−62405.

(24) Akazawa, M.; Kojima, Y.; Kato, Y. Pyrolysate Formation from Four Different Phenyl Propanols and Classification of the Initial Reaction Pathways. *Int. J. Renew. Energy Technol.* **2015**, *4*, 1−14.

(25) Akazawa, M.; Kojima, Y.; Kato, Y. Reaction Mechanisms of Pyrolysis of Four Different Phenylpropanoids. *Pyrol. Technol. J.* **2015**, *1*, 1−12.

(26) Furutani, Y.; Dohara, Y.; Kudo, S.; Hayashi, J.-I.; Norinaga, K. Computational Study on the Thermal Decomposition of Phenol-Type Monolignols. *Int. J. Chem. Kinet.* **2018**, *50*, 304−316.

(27) Asatryan, R.; Hudzik, J. M.; Bozzelli, J. W.; Khachatryan, L.; Ruckenstein, E. OH-Initiated Reactions of *p*-Coumaryl Alcohol Relevant to the Lignin Pyrolysis. Part I. Potential Energy Surface Analysis. *J. Phys. Chem. A* **2019**, *123*, 2570−2585.

(28) Kato, Y.; Kohnosu, T.; Enomoto, R.; Akazawa, M.; Yoon, S.-L.; Kojima, Y. Chemical Properties of Bio-Oils Produced by Fast Pyrolysis of Bamboo. *Trans. Mat. Res. Soc. Japan* **2014**, *39*, 491−498.

(29) Harman-Ware, A. E.; Crocker, M.; Kaur, A. P.; Meier, M. S.; Kato, D.; Lynn, B. Pyrolysis-GC/MS of Sinapyl and Coniferyl Alcohol. *J. Anal. Appl. Pyrolysis* **2013**, *99*, 161−169.

(30) Domburg, G. E.; Sergeeva, V. N.; Zheibe, G. A. Thermal Analysis of Some Lignin Model Compounds. *J. Therm. Anal.* **1970**, *2*, 419−428.

(31) Kuroda, K.-i.; Ashitani, T.; Fujita, K.; Hattori, T. Thermal Behavior of β-1 Subunits in Lignin: Pyrolysis of 1,2-Diarylpropane-1,3-

Diol-Type Lignin Model Compounds. *J. Agric. Food Chem.* **2007**, *55*, 2770−2778.
(32) Shigematsu, M.; Kobayashi, T.; Taguchi, H.; Tanahashi, M. Transition State Leading to β-O′ Quinonemethide Intermediate of p-Coumaryl Alcohol Analyzed by Semi-Empirical Molecular Orbital Calculation. *J. Wood Sci.* **2006**, *52*, 128−133.
(33) Kawamoto, H.; Horigoshi, S.; Saka, S. Pyrolysis Reactions of Various Lignin Model Dimers. *J. Wood Sci.* **2007**, *53*, 168−174.
(34) Westmoreland, P. R.; Fahey, P. J. Dehydration and Dehydrogenation Kinetics of OH Groups in Biomass Pyrolysis. *Chem. Eng. Trans.* **2016**, *50*, 73−78.
(35) Lin, Y.-C.; Cho, J.; Tompsett, G. A.; Westmoreland, P. R.; Huber, G. W. Kinetics and Mechanism of Cellulose Pyrolysis. *J. Phys. Chem. C* **2009**, *113*, 20097−20107.
(36) Wang, S.; Ru, B.; Lin, H.; Dai, G.; Wang, Y.; Luo, Z. Kinetic Study on Pyrolysis of Biomass Components: A Critical Review. *Curr. Org. Chem.* **2016**, *20*, 2489−2513.
(37) Klein, M. T.; Virk, P. S. Model Pathways in Lignin Thermolysis. I. Phenethyl Phenyl Ether. *Ind. Eng. Chem. Fund.* **1983**, *22*, 35−45.
(38) Faravelli, T.; Frassoldati, A.; Migliavacca, G.; Ranzi, E. Detailed Kinetic Modeling of the Thermal Degradation of Lignins. *Biomass Bioenergy* **2010**, *34*, 290−301.
(39) Yang, H.-M.; Appari, S.; Kudo, S.; Hayashi, J.-i.; Norinaga, K. Detailed Chemical Kinetic Modeling of Vapor-Phase Reactions of Volatiles Derived from Fast Pyrolysis of Lignin. *Ind. Eng. Chem. Res.* **2015**, *54*, 6855−6864.
(40) Hough, B. R.; Schwartz, D. T.; Pfaendtner, J. Detailed Kinetic Modeling of Lignin Pyrolysis for Process Optimization. *Ind. Eng. Chem. Res.* **2016**, *55*, 9147−9153.
(41) Furutani, Y.; Kudo, S.; Hayashi, J.-i.; Norinaga, K. Predicting Molecular Composition of Primary Product Derived from Fast Pyrolysis of Lignin with Semi-Detailed Kinetic Model. *Fuel* **2018**, *212*, 515−522.
(42) Zhou, S.; Garcia-Perez, M.; Pecha, B.; McDonald, A. G.; Kersten, S. R. A.; Westerhof, R. J. M. Secondary Vapor Phase Reactions of Lignin-Derived Oligomers Obtained by Fast Pyrolysis of Pine Wood. *Energy Fuels* **2013**, *27*, 1428−1438.
(43) Caballero, J. A.; Font, R.; Marcilla, A. Kinetic Study of the Secondary Thermal Decomposition of Kraft Lignin. *J. Anal. Appl. Pyrolysis* **1996**, *38*, 131−152.
(44) Evans, R. J.; Milne, T. A.; Soltys, M. N. Direct Mass-Spectrometric Studies of the Pyrolysis of Carbonaceous Fuels. III. Primary Pyrolysis of Lignin. *J. Anal. Appl. Pyrolysis* **1986**, *9*, 207−236.
(45) Piskorz, J.; Majerski, P.; Radlein, D. Pyrolysis of Biomass—Aerosol Generation: Properties, Applications, and Significance for Process Engineers. *4th, Biomass Conference of the Americas*; Elsevier Science: Oakland, CA, 1999; Vol. 2, pp 1153−1160.
(46) Khachatryan, L.; Barekati-Goudarzi, M.; Kekejian, D.; Aguilar, G.; Asatryan, R.; Stanley, G. G.; Boldor, D. Pyrolysis of Lignin in Gas-Phase Isothermal and cw-CO_2 Laser Powered Non-Isothermal Reactors. *Energy Fuels* **2018**, *32*, 12597−12606.
(47) Amen-Chen, C.; Pakdel, H.; Roy, C. Production of Monomeric Phenols by Thermochemical Conversion of Biomass: A Review. *Bioresour. Technol.* **2001**, *79*, 277−299.
(48) Bährle, C.; Custodis, V.; Jeschke, G.; van Bokhoven, J. A.; Vogel, F. In Situ Observation of Radicals and Molecular Products During Lignin Pyrolysis. *ChemSusChem* **2014**, *7*, 2022−2029.
(49) Brežný, R.; Mihalov, V.; Kováčik, V. Low Temperature Thermolysis of Lignins. I. Reactions of β-O-4 Model Compounds. *Holzforschung* **1983**, *37*, 199−204.
(50) Elder, T.; Beste, A. Density Functional Theory Study of the Concerted Pyrolysis Mechanism for Lignin Models. *Energy Fuels* **2014**, *28*, 5229−5235.
(51) Kim, K. H.; Bai, X.; Brown, R. C. Pyrolysis Mechanisms of Methoxy Substituted α-O-4 Lignin Dimeric Model Compounds and Detection of Free Radicals Using Electron Paramagnetic Resonance Analysis. *J. Anal. Appl. Pyrolysis* **2014**, *110*, 254−263.
(52) Pandey, M. P.; Kim, C. S. Lignin Depolymerization and Conversion: A Review of Thermochemical Methods. *Chem. Eng. Technol.* **2011**, *34*, 29−41.
(53) Sazanov, Y. N.; Gribanov, A. V. Thermochemistry of Lignin. *Russ. J. Appl. Chem.* **2010**, *83*, 175−194.
(54) Kleinert, M.; Barth, T. Phenols from Lignin. *Chem. Eng. Technol.* **2008**, *31*, 736−745.
(55) Simon, J. P.; Eriksson, K.-E. L. The Significance of Intramolecular Hydrogen Bonding in the β-O-4 Linkage of Lignin. *J. Mol. Struct.* **1996**, *384*, 1−7.
(56) Daniel, D.; Khachatryan, L.; Astete, C.; Asatryan, R.; Marculescu, C.; Boldor, D. Sulfur Contaminations Inhibit Depolymerization of Kraft Lignin. *Bioresour. Technol. Rep.* **2019**, *8*, 100341.
(57) Britt, P. F.; Buchanan, A. C. I., III; Malcolm, E. A. Thermolysis of Phenethyl Phenyl Ether: A Model for Ether Linkages in Lignin and Low Rank Coal. *J. Org. Chem.* **1995**, *60*, 6523−6536.
(58) Britt, P. F.; Buchanan, A. C., III; Cooney, M. J.; Martineau, D. R. Flash Vacuum Pyrolysis of Methoxy-Substituted Lignin Model Compounds. *J. Org. Chem.* **2000**, *65*, 1376−1389.
(59) Chu, S.; Subrahmanyam, A. V.; Huber, G. W. The Pyrolysis Chemistry of a β-O-4 Type Oligomeric Lignin Model Compound. *Green Chem.* **2013**, *15*, 125−136.
(60) Jarvis, M. W.; Daily, J. W.; Carstensen, H.-H.; Dean, A. M.; Sharma, S.; Dayton, D. C.; Robichaud, D. J.; Nimlos, M. R. Direct Detection of Products from the Pyrolysis of 2-Phenethyl Phenyl Ether. *J. Phys. Chem. A* **2011**, *115*, 428−438.
(61) Chen, L.; Ye, X.; Luo, F.; Shao, J.; Lu, Q.; Fang, Y.; Wang, X.; Chen, H. Pyrolysis Mechanism of β-O-4 Type Lignin Model Dimer. *J. Anal. Appl. Pyrolysis* **2015**, *115*, 103−111.
(62) Huang, X.; Liu, C.; Huang, J.; Li, H. Theory Studies on Pyrolysis Mechanism of Phenethyl Phenyl Ether. *Comput. Theor. Chem.* **2011**, *976*, 51−59.
(63) Hu, J.; Shen, D.; Xiao, R.; Wu, S.; Zhang, H. Free-Radical Analysis on Thermochemical Transformation of Lignin to Phenolic Compounds. *Energy Fuels* **2013**, *27*, 285−293.
(64) Beste, A.; Buchanan, A. C., III Challenges in the Computation of Rate Constants for Lignin Model Compounds In *Rate Constant Calculation for Thermal Reactions: Methods and Applications*; DaCosta, H., Fan, M., Eds.; John Wiley & Sons, Inc.: New Jersey, 2011; pp 191−238.
(65) Huang, J.; Liu, C.; Wu, D.; Tong, H.; Ren, L. Density Functional Theory Studies on Pyrolysis Mechanism of β-O-4 Type Lignin Dimer Model Compound. *J. Anal. Appl. Pyrolysis* **2014**, *109*, 98−108.
(66) Jiang, W.; Wu, S.; Lucia, L. A.; Chu, J. A Comparison of the Pyrolysis Behavior of Selected β-O-4 Type Lignin Model Compounds. *J. Anal. Appl. Pyrolysis* **2017**, *125*, 185−192.
(67) Brandrup, J.; Immergut, E. H. *Polymer Handbook*, 3rd ed.; John Wiley & Sons, Ltd., 1990.
(68) Durbeej, B.; Eriksson, L. A. A Density Functional Theory Study of Coniferyl Alcohol Intermonomeric Cross Linkages in Lignin - Three-Dimensional Structures, Stabilities and the Thermodynamic Control Hypothesis. *Holzforschung* **2003**, *57*, 150−164.
(69) Durbeej, B.; Eriksson, L. A. Formation of β-O-4 Lignin Models—A Theoretical Study. *Holzforschung* **2003**, *57*, 466−478.
(70) Martinez, C.; Rivera, J. L.; Herrera, R.; Rico, J. L.; Flores, N.; Rutiaga, J. G.; López, P. Evaluation of the Chemical Reactivity in Lignin Precursors using the Fukui Function. *J. Mol. Model.* **2008**, *14*, 77−81.
(71) Sangha, A. K.; Parks, J. M.; Standaert, R. F.; Ziebell, A.; Davis, M.; Smith, J. C. Radical Coupling Reactions in Lignin Synthesis: A Density Functional Theory Study. *J. Phys. Chem. B* **2012**, *116*, 4760−4768.
(72) Shigematsu, M.; Masamoto, H. Solvent Effects on the Electronic State of Monolignol Radicals as Predicted by Molecular Orbital Calculations. *J. Wood Sci.* **2008**, *54*, 308−311.
(73) Ponomarev, D. A. Formation of Quinone Methides: An Alternative Pathway of Thermal Degradation of Some β-O-4-Ethers as Compounds Modeling Lignin. *Russ. J. Appl. Chem.* **1997**, *70*, 824−826.

https://dx.doi.org/10.1021/acs.jpca.9b11894
J. Phys. Chem. A 2020, 124, 4875−4904

(74) Britt, P. F.; Buchanan, A. C., III; Thomas, K. B.; Lee, S.-K. Pyrolysis Mechanisms of Lignin: Surface-Immobilized Model Compound Investigation of Acid-Catalyzed and Free-Radical Reaction Pathways. *J. Anal. Appl. Pyrolysis* **1995**, *33*, 1−19.
(75) Akazawa, M.; Kojima, Y.; Kato, Y. Effect of Pyrolysis Temperature on the Pyrolytic Degradation Mechanism of β-Aryl Ether Linkages. *J. Anal. Appl. Pyrolysis* **2016**, *118*, 164−174.
(76) Beste, A.; Buchanan, A. C., III Computational Investigation of the Pyrolysis Product Selectivity for α-Hydroxy Phenethyl Phenyl Ether and Phenethyl Phenyl Ether: Analysis of Substituent Effects and Reactant Conformer Selection. *J. Phys. Chem. A* **2013**, *117*, 3235−3242.
(77) Kuroda, K.-i. Analytical Pyrolysis Products Derived from Cinnamyl Alcohol-End Groups in Lignins. *J. Anal. Appl. Pyrolysis* **2000**, *53*, 123−134.
(78) Korobkov, V. Y.; Grigorieva, E. N.; Bykov, V. I.; Kalechitz, I. V. Effect of the Structure of Coal-Related Model Ethers on the Rate and Mechanism of Their Thermolysis. 2. Effect of Substituents in the $C_6H_5CH_2OC_6H_4X$ structure. *Fuel* **1988**, *67*, 663−665.
(79) Korobkov, V. Y.; Grigorieva, E. N.; Bykov, V. I.; Senko, O. V.; Kalechitz, I. V. Effect of the Structure of Coal-Related Model Ethers on the Rate and Mechanism of Their Thermolysis. 1. Effect of the Number of Methylene Groups in the $R(CH_2)_nO(CH_2)_mR$ Structure. *Fuel* **1988**, *67*, 657−662.
(80) Da Silva, G.; Bozzelli, J. W. Quantum Chemical Study of the Thermal Decomposition of *o*-Quinone Methide (6-Methylene-2,4-cyclohexadien-1-one). *J. Phys. Chem. A* **2007**, *111*, 7987−7994.
(81) Dorrestijn, E.; Epema, O. J.; Van Scheppingen, W. B.; Mulder, P. *o*-Quinone Methide as a Common Intermediate in the Pyrolysis of *o*-Hydroxybenzyl Alcohol, Chroman and 1,4-Benzodioxin. *J. Chem. Soc., Perkin Trans. 2* **1998**, 1173−1178.
(82) Nowakowska, M.; Herbinet, O.; Dufour, A.; Glaude, P.-A. Detailed Kinetic Study of Anisole Pyrolysis and Oxidation to Understand Tar Formation During Biomass Combustion and Gasification. *Combust. Flame* **2014**, *161*, 1474−1488.
(83) Khachatryan, L.; Adounkpe, J.; Maskos, Z.; Dellinger, B. Formation of Cyclopentadienyl Radical from the Gas-Phase Pyrolysis of Hydroquinone, Catechol, and Phenol. *Environ. Sci. Technol.* **2006**, *40*, 5071−5076.
(84) Lomnicki, S.; Truong, H.; Dellinger, B. Mechanisms of Product Formation from the Pyrolytic Thermal Degradation of Catechol. *Chemosphere* **2008**, *73*, 629−633.
(85) Khachatryan, L.; Adounkpe, J.; Asatryan, R.; Dellinger, B. *11th International Congress on Combustion By-Products and Their Health Effects, Research Triangle Park, NC*, May 31, 2009.
(86) Altarawneh, M.; Dlugogorski, B. Z.; Kennedy, E. M.; Mackie, J. C. Theoretical Study of Unimolecular Decomposition of Catechol. *J. Phys. Chem. A* **2010**, *114*, 1060−1067.
(87) Khachatryan, L.; Adounkpe, J.; Asatryan, R.; Dellinger, B. Radicals from the Gas-Phase Pyrolysis of Catechol: 1. *o*-Semiquinone and *ipso*-Catechol Radicals. *J. Phys. Chem. A* **2010**, *114*, 2306−2312.
(88) Khachatryan, L.; Asatryan, R.; McFerrin, C.; Adounkpe, J.; Dellinger, B. Radicals from the Gas-Phase Pyrolysis of Catechol. 2. Comparison of the Pyrolysis of Catechol and Hydroquinone. *J. Phys. Chem. A* **2010**, *114*, 10110−10116.
(89) Kamarchik, E.; Koziol, L.; Reisler, H.; Bowman, J. M.; Krylov, A. I. Roaming Pathway Leading to Unexpected Water + Vinyl Products in C_2H_4OH Dissociation. *J. Phys. Chem. Lett.* **2010**, *1*, 3058−3065.
(90) Greenwald, E. E.; North, S. W.; Georgievskii, Y.; Klippenstein, S. J. A Two Transition State Model for Radical-Molecule Reactions: A Case Study of the Addition of OH to C_2H_4. *J. Phys. Chem. A* **2005**, *109*, 6031−6044.
(91) Yamada, T.; Bozzelli, J. W.; Lay, T. Kinetic and Thermodynamic Analysis on OH Addition to Ethylene: Adduct Formation, Isomerization, and Isomer Dissociations. *J. Phys. Chem. A* **1999**, *103*, 7646−7655.
(92) Asatryan, R.; Da Silva, G.; Bozzelli, J. W. Quantum Chemical Study of the Acrolein (CH_2CHCHO) + OH + O_2 Reactions. *J. Phys. Chem. A* **2010**, *114*, 8302−8311.
(93) So, S.; Wille, U.; Da Silva, G. Atmospheric chemistry of enols: A theoretical study of the vinyl alcohol + OH + O2 reaction mechanism. *Environ. Sci. Technol.* **2014**, *48*, 6694−6701.
(94) Lei, X.; Wang, W.; Cai, J.; Wang, C.; Liu, F.; Wang, W. Atmospheric Chemistry of Enols: Vinyl Alcohol + OH + O2 Reaction Revisited. *J. Phys. Chem. A* **2019**, *123*, 3205−3213.
(95) Cho, J.; Roueintan, M.; Li, Z. Kinetic and Dynamic Investigations of OH Reaction with Styrene. *J. Phys. Chem. A* **2014**, *118*, 9460−9470.
(96) Dupuis, M.; Lester, W. A., Jr. Hydrogen Atom Abstraction from Aldehydes: $OH+H_2CO$ and $O+H_2CO$. *J. Chem. Phys.* **1984**, *81*, 847−850.
(97) Taylor, P. H.; Rahman, M. S.; Arif, M.; Dellinger, B.; Marshall, P. Kinetic and Mechanistic Studies of the Reaction of Hydroxyl Radicals with Acetaldehyde over an Extended Temperature Range. *Symp. (Int.) Combust.* **1996**, *26*, 497−504.
(98) Yetter, R. A.; Rabitz, H.; Dryer, F. L.; Maki, R. G.; Klemm, R. B. Evaluation of the Rate Constant for the Reaction $OH+H_2CO$: Application of Modeling and Sensitivity Analysis Techniques for Determination of the Product Branching Ratio. *J. Chem. Phys.* **1989**, *91*, 4088−4097.
(99) Davis, M. E.; Burkholder, J. B. Rate Coefficients for the Gas-Phase Reaction of OH with (Z)-3-Hexen-1-ol, 1-Penten-3-ol, (E)-2-Penten-1-ol, and (E)-2-Hexen-1-ol Between 243 and 404 K. *Atmos. Chem. Phys.* **2011**, *11*, 3347−3358.
(100) De Bruycker, R.; Herbinet, O.; Carstensen, H.-H.; Battin-Leclerc, F.; Van Geem, K. M. Understanding the Reactivity of Unsaturated Alcohols: Experimental and Kinetic Modeling Study of the Pyrolysis and Oxidation of 3-Methyl-2-Butenol and 3-Methyl-3-Butenol. *Combust. Flame* **2016**, *171*, 237−251.
(101) Zhang, Y.; Chao, K.; Sun, J.; Su, Z.; Pan, X.; Zhang, J.; Wang, R. Theoretical Study on the Gas Phase Reaction of Allyl Alcohol with Hydroxyl Radical. *J. Phys. Chem. A* **2013**, *117*, 6629−6640.
(102) Asatryan, R.; Pal, Y.; Hachmann, J.; Ruckenstein, E. Roaming-Like Mechanism for Dehydration of Diol Radicals. *J. Phys. Chem. A* **2018**, *122*, 9738−9754.
(103) Upadhyaya, H. P.; Kumar, A.; Naik, P. D.; Sapre, A. V.; Mittal, J. P. Kinetics of OH Radical Reaction with Allyl Alcohol ($H_2C=CHCH_2OH$) and Propargyl Alcohol ($HCCCH_2OH$) Studied by LIF. *Chem. Phys. Lett.* **2001**, *349*, 279−285.
(104) Papagni, C.; Arey, J.; Atkinson, R. Rate Constants for the Gas-Phase Reactions of OH Radicals with a Series of Unsaturated Alcohols. *Int. J. Chem. Kinet.* **2001**, *33*, 142−147.
(105) Kawamoto, H.; Ryoritani, M.; Saka, S. Different Pyrolytic Cleavage Mechanisms of β-Ether Bond Depending on the Side-Chain Structure of Lignin Dimers. *J. Anal. Appl. Pyrolysis* **2008**, *81*, 88−94.
(106) Kawamoto, H.; Horigoshi, S.; Saka, S. Effects of Side-Chain Hydroxyl Groups on Pyrolytic β-Ether Cleavage of Phenolic Lignin Model Dimer. *J. Wood Sci.* **2007**, *53*, 268−271.
(107) Nakamura, T.; Kawamoto, H.; Saka, S. Condensation Reactions of Some Lignin Related Compounds at Relatively Low Pyrolysis Temperature. *J. Wood Chem. Technol.* **2007**, *27*, 121−133.
(108) Asatryan, R.; Davtyan, A.; Khachatryan, L.; Dellinger, B. Theoretical Study of Open-Shell *ipso*-Addition and bis-Keto Dimer Interconversion Reactions Related to Gas-Phase Formation of PCDD/FS from Chlorinated Phenols. *Organohalogen Compd.* **2002**, *56*, 277−280.
(109) Masuku, C. P. Thermolytic Decomposition of Coniferyl Alcohol. *J. Anal. Appl. Pyrolysis* **1992**, *23*, 195−208.
(110) Asatryan, R.; Davtyan, A.; Khachatryan, L.; Dellinger, B. Molecular Modeling Studies of the Reactions of Phenoxy Radical Dimers: Pathways to Dibenzofurans. *J. Phys. Chem. A* **2005**, *109*, 11198−11205.
(111) Manion, J. A.; Louw, R. Rates and Mechanisms of Gas-Phase Desubstitution of Hexadeuteriobenzene and Benzene Derivatives C_6H_5X, X = CH_3, CF_3, OH, Cl, and F, by H Atoms Between 898 and 1039 K. *J. Phys. Chem.* **1990**, *94*, 4127−4134.

https://dx.doi.org/10.1021/acs.jpca.9b11894
J. Phys. Chem. A 2020, 124, 4875−4904

(112) Seta, T.; Nakajima, M.; Miyoshi, A. High-Temperature Reactions of OH Radicals with Benzene and Toluene. *J. Phys. Chem. A* **2006**, *110*, 5081−5090.
(113) Nakamura, T.; Kawamoto, H.; Saka, S. Pyrolysis Behavior of Japanese Cedar Wood Lignin Studied with Various Model Dimers. *J. Anal. Appl. Pyrolysis* **2008**, *81*, 173−182.
(114) Nimlos, M. R.; Blanksby, S. J.; Qian, X.; Himmel, M. E.; Johnson, D. K. Mechanisms of Glycerol Dehydration. *J. Phys. Chem. A* **2006**, *110*, 6145−6156.
(115) Laino, T.; Tuma, C.; Curioni, A.; Jochnowitz, E.; Stolz, S. A Revisited Picture of the Mechanism of Glycerol Dehydration. *J. Phys. Chem. A* **2011**, *115*, 3592−3595.
(116) Moc, J.; Simmie, J. M.; Curran, H. J. The Elimination of Water from a Conformationally Complex Alcohol: A Computational Study of the Gas Phase Dehydration of *n*-Butanol. *J. Mol. Struct.* **2009**, *928*, 149−157.
(117) Zádor, J.; Jasper, A. W.; Miller, J. A. The Reaction Between Propene and Hydroxyl. *Phys. Chem. Chem. Phys.* **2009**, *11*, 11040−11053.
(118) Daranlot, J.; Bergeat, A.; Caralp, F.; Caubet, P.; Costes, M.; Forst, W.; Loison, J. C.; Hickson, K. M. Gas-phase Kinetics of Hydroxyl Radical Reactions with Alkenes: Experiment and Theory. *ChemPhysChem* **2010**, *11*, 4002−4010.
(119) Daranlot, J.; Hickson, K. M.; Loison, J.-C.; Méreau, R.; Caralp, F.; Forst, W.; Bergeat, A. Gas-Phase Kinetics of the Hydroxyl Radical Reaction with Allene: Absolute Rate Measurements at Low Temperature, Product Determinations, and Calculations. *J. Phys. Chem. A* **2012**, *116*, 10871−10881.
(120) Da Silva, G.; Bozzelli, J. W.; Asatryan, R. Hydroxyl Radical Initiated Oxidation of *s*-Triazine: Hydrogen Abstraction is Faster than Hydroxyl Addition. *J. Phys. Chem. A* **2009**, *113*, 8596−8606.
(121) Hosoya, T.; Kawamoto, H.; Saka, S. Role of Methoxyl Group in Char Formation from Lignin-Related Compounds. *J. Anal. Appl. Pyrolysis* **2009**, *84*, 79−83.
(122) Chai, J.-D.; Head-Gordon, M. Long-Range Corrected Hybrid Density Functionals with Damped Atom-Atom Dispersion Corrections. *Phys. Chem. Chem. Phys.* **2008**, *10*, 6615−6620.
(123) Zheng, J.; Xu, X.; Truhlar, D. G. Minimally Augmented Karlsruhe Basis Sets. *Theor. Chem. Acc.* **2011**, *128*, 295−305.
(124) Binkley, J. S.; Pople, J. A.; Hehre, W. J. Self-Consistent Molecular Orbital Methods. 21. Small Split-Valence Basis Sets for First-Row Elements. *J. Am. Chem. Soc.* **1980**, *102*, 939−947.
(125) Weigend, F.; Ahlrichs, R. Balanced Basis Sets of Split Valence, Triple Zeta Valence and Quadruple Zeta Valence Quality for H to Rn: Design and Assessment of Accuracy. *Phys. Chem. Chem. Phys.* **2005**, *7*, 3297−3305.
(126) Montgomery, J. A., Jr.; Frisch, M. J.; Ochterski, J. W.; Petersson, G. A. A Complete Basis Set Model Chemistry. VI. Use of Density Functional Geometries and Frequencies. *J. Chem. Phys.* **1999**, *110*, 2822−2827.
(127) Montgomery, J. A., Jr.; Frisch, M. J.; Ochterski, J. W.; Petersson, G. A. A Complete Basis Set Model Chemistry. VII. Use of the Minimum Population Localization Method. *J. Chem. Phys.* **2000**, *112*, 6532−6542.
(128) Simmie, J. M.; Somers, K. P. Benchmarking Compound Methods (CBS-QB3, CBS-APNO, G3, G4, W1BD) against the Active Thermochemical Tables: A Litmus Test for Cost-Effective Molecular Formation Enthalpies. *J. Phys. Chem. A* **2015**, *119*, 7235−7246.
(129) Somers, K. P.; Simmie, J. M. Benchmarking Compound Methods (CBS-QB3, CBS-APNO, G3, G4, W1BD) Against the Active Thermochemical Tables: Formation Enthalpies of Radicals. *J. Phys. Chem. A* **2015**, *119*, 8922−8933.
(130) Frisch, M. J.; Trucks, G. W.; Schlegel, H. B.; Scuseria, G. E.; Robb, M. A.; Cheeseman, J. R.; Scalmani, G.; Barone, V.; Petersson, G. A.; Nakatsuji, H.; et al. *Gaussian 16*, Revision A.03; Gaussian, Inc.: Wallingford, CT, 2016.
(131) Asatryan, R.; Bozzelli, J. W.; Simmie, J. M. Thermochemistry of Methyl and Ethyl Nitro, RNO2, and Nitrite, RONO, Organic Compounds. *J. Phys. Chem. A* **2008**, *112*, 3172−3185.
(132) Cox, J. D.; Wagman, D. D.; Medvedev, V. A. *CODATA Key Values for Thermodynamics*; Hemisphere Publishing, Corp.: New York, NY, 1989.
(133) Ruscic, B. Active Thermochemical Tables: Sequential Bond Dissociation Enthalpies of Methane, Ethane, and Methanol and the Related Thermochemistry. *J. Phys. Chem. A* **2015**, *119*, 7810−7837.
(134) Asatryan, R.; Bozzelli, J. W. Chain Branching and Termination in the Low-Temperature Combustion of *n*-Alkanes: 2-Pentyl Radical + O_2, Isomerization and Association of the Second O_2. *J. Phys. Chem. A* **2010**, *114*, 7693−7708.
(135) Asatryan, R.; Bozzelli, J. W.; Ruckenstein, E. Dihydrogen Catalysis: A Degradation Mechanism for N_2-Fixation Intermediates. *J. Phys. Chem. A* **2012**, *116*, 11618−11642.
(136) Matsugi, A. Roaming Dissociation of Ethyl Radicals. *J. Phys. Chem. Lett.* **2013**, *4*, 4237−4240.
(137) Asatryan, R.; Ruckenstein, E. Dihydrogen Catalysis: A Remarkable Avenue in the Reactivity of Molecular Hydrogen. *Catal. Rev. Sci. Eng.* **2014**, *56*, 403−475.
(138) Kohl, I. E.; Asatryan, R.; Bao, H. No Oxygen Isotope Exchange Between Water and APS-Sulfate at Surface Temperature: Evidence from Quantum Chemical Modeling and Triple-Oxygen Isotope Experiments. *Geochim. Cosmochim. Acta* **2012**, *95*, 106−118.
(139) Zhao, Y.; Truhlar, D. G. The M06 Suite of Density Functionals for Main Group Thermochemistry, Thermochemical Kinetics, Noncovalent Interactions, Excited States, and Transition Elements: Two New Functionals and Systematic Testing of Four M06-Class Functionals and 12 Other Functionals. *Theor. Chem. Accounts* **2008**, *120*, 215−241.
(140) Zhao, Y.; Truhlar, D. G. Density Functionals with Broad Applicability in Chemistry. *Acc. Chem. Res.* **2008**, *41*, 157−167.
(141) Becke, A. D. Density-Functional Thermochemistry. III. The Role of Exact Exchange. *J. Chem. Phys.* **1993**, *98*, 5648−5652.
(142) Lee, C.; Yang, W.; Parr, R. G. Development of the Colle-Salvetti Correlation-Energy Formula into a Functional of the Electron Density. *Phys. Rev. B: Condens. Matter Mater. Phys.* **1988**, *37*, 785−789.
(143) Sheng, C. Elementary, Pressure Dependent Model for Combustion of C1, C2 and Nitrogen Containing Hydrocarbons: Operation of a Pilot Scale Incinerator and Model Comparison. Ph.D. Dissertation, Department of Chemical Engineering, New Jersey Institute of Technology, Newark, NJ, 2002.
(144) Alecu, I. M.; Zheng, J.; Zhao, Y.; Truhlar, D. G. Computational Thermochemistry: Scale Factor Databases and Scale Factors for Vibrational Frequencies Obtained from Electronic Model Chemistries. *J. Chem. Theory Comput.* **2010**, *6*, 2872−2887.
(145) Lay, T. H.; Krasnoperov, L. N.; Venanzi, C. A.; Bozzelli, J. W.; Shokhirev, N. V. Ab Initio Study of α-Chlorinated Ethyl Hydroperoxides CH_3CH_2OOH, $CH_3CHClOOH$, and CH_3CCl_2OOH: Conformational Analysis, Internal Rotation Barriers, Vibrational Frequencies, and Thermodynamic Properties. *J. Phys. Chem.* **1996**, *100*, 8240−8249.
(146) Eckart, C. The Penetration of a Potential Barrier by Electrons. *Phys. Rev.* **1930**, *35*, 1303−1309.
(147) Johnston, H. S. *Gas Phase Reaction Rate Theory*; Ronald Press Co., 1966.
(148) Johnston, H. S.; Heicklen, J. Tunnelling Corrections for Unsymmetrical Eckart Potential Energy Barriers. *J. Phys. Chem.* **1962**, *66*, 532−533.
(149) Sheng, C. Y.; Bozzelli, J. W.; Dean, A. M.; Chang, A. Y. Detailed Kinetics and Thermochemistry of $C_2H_5 + O_2$: Reaction Kinetics of the Chemically-Activated and Stabilized CH_3CH_2OO. Adduct. *J. Phys. Chem. A* **2002**, *106*, 7276−7293.
(150) Chang, A. Y.; Bozzelli, J. W.; Dean, A. M. Kinetic Analysis of Complex Chemical Activation and Unimolecular Dissociation Reactions Using QRRK Theory and the Modified Strong Collision Approximation. *Z. Phys. Chem.* **2000**, *214*, 1533−1568.
(151) Goldsmith, C. F.; Magoon, G. R.; Green, W. H. Database of Small Molecule Thermochemistry for Combustion. *J. Phys. Chem. A* **2012**, *116*, 9033−9057.

https://dx.doi.org/10.1021/acs.jpca.9b11894
J. Phys. Chem. A 2020, 124, 4875−4904

(152) Chase, M. W., Jr. NIST-JANAF Thermochemical Tables. *J. Phys. Chem. Ref. Data, Monogr.* **1998**, *9*, 1−1951.
(153) Ruscic, B.; Bross, D. H. Active Thermochemical Tables (ATcT) Values based on ver. 1.122g of the Thermochemical Network. https://ATcT.anl.gov (accessed 2019-09-20).
(154) Alvarez-Idaboy, J. R.; Mora-Diez, N.; Boyd, R. J.; Vivier-Bunge, A. On the Importance of Prereactive Complexes in Molecule-Radical Reactions: Hydrogen Abstraction from Aldehydes by OH. *J. Am. Chem. Soc.* **2001**, *123*, 2018−2024.
(155) Alvarez-Idaboy, J. R.; Mora-Diez, N.; Vivier-Bunge, A. A Quantum Chemical and Classical Transition State Theory Explanation of Negative Activation Energies in OH Addition to Substituted Ethenes. *J. Am. Chem. Soc.* **2000**, *122*, 3715−3720.
(156) Sekušak, S.; Liedl, K. R.; Sabljić, A. Reactivity and Regioselectivity of Hydroxyl Radical Addition to Halogenated Ethenes. *J. Phys. Chem. A* **1998**, *102*, 1583−1594.
(157) Singleton, D. L.; Cvetanovic, R. J. Temperature Dependence of the Reaction of Oxygen Atoms with Olefins. *J. Am. Chem. Soc.* **1976**, *98*, 6812−6819.
(158) Safaei, Z.; Shiroudi, A.; Zahedi, E.; Sillanpää, M. Atmospheric Oxidation Reactions of Imidazole Initiated by Hydroxyl Radicals: Kinetics and Mechanism of Reactions and Atmospheric Implications. *Phys. Chem. Chem. Phys.* **2019**, *21*, 8445−8456.
(159) Du, B.; Zhang, W. Atmospheric Oxidation Chemistry of 1−Methoxy 2−Propyl Acetate Initiated by OH Radicals: Kinetics and Mechanisms. *Mol. Phys.* **2019**, *118*, No. e1601786.
(160) Hudzik, J. M.; Bozzelli, J. W.; Asatryan, R.; Ruckenstein, E. OH-Initiated Reactions of *para*-Coumaryl Alcohol Relevant to the Lignin Pyrolysis. Part III. Kinetics of H-Abstraction by H, OH, and CH_3 Radicals. *J. Phys. Chem. A* **2020**, DOI: 10.1021/acs.jpca.9b11898, , Accepted.
(161) Sun, Z.; Bottari, G.; Afanasenko, A.; Stuart, M. C. A.; Deuss, P. J.; Fridrich, B.; Barta, K. Complete Lignocellulose Conversion with Integrated Catalyst Recycling Yielding Valuable Aromatics and Fuels. *Nat. Catal.* **2018**, *1*, 82−92.
(162) Head-Gordon, M.; Pople, J. A.; Frisch, M. J. MP2 Energy Evaluation by Direct Methods. *Chem. Phys. Lett.* **1988**, *153*, 503−506.
(163) Bozzelli, J. W.; Chang, A. Y.; Dean, A. M. Molecular Density of States from Estimated Vapor Phase Heat Capacities. *Int. J. Chem. Kinet.* **1997**, *29*, 161−170.
(164) D'Anna, B.; Bakken, V.; Are Beukes, J.; Nielsen, C. J.; Brudnik, K.; Jodkowski, J. T. Experimental and Theoretical Studies of Gas Phase NO_3 and OH Radical Reactions with Formaldehyde, Acetaldehyde and Their Isotopomers. *Phys. Chem. Chem. Phys.* **2003**, *5*, 1790−1805.
(165) Atkinson, R.; Pitts, J. N., Jr. Kinetics of the Reactions of the OH Radical with HCHO and CH_3CHO over the Temperature Range 299-426°K. *J. Chem. Phys.* **1977**, *68*, 3581−3584.
(166) Francisco, J. S. An Examination of Substituent Effects on the Reaction of OH Radicals with HXCO (where X=H, F, and Cl). *J. Chem. Phys.* **1992**, *96*, 7597−7602.
(167) Niki, H.; Maker, P. D.; Savage, C. M.; Breitenbach, L. P. Relative Rate Constants for the Reaction of Hydroxyl Radical with Aldehydes. *J. Phys. Chem.* **1978**, *82*, 132−134.
(168) Lin, X.; Sui, S.; Tan, S.; Pittman, C.; Sun, J.; Zhang, Z. Fast Pyrolysis of Four Lignins from Different Isolation Processes Using Py-GC/MS. *Energies* **2015**, *8*, 5107−5121.
(169) Lou, R.; Wu, S. B.; Lv, G. J. Fast Pyrolysis of Enzymatic/Mild Acidolysis Lignin From Moso Bamboo. *BioResources* **2010**, *5*, 11.
(170) Shin, E.-J.; Nimlos, M. R.; Evans, R. J. A Study of the Mechanisms of Vanillin Pyrolysis by Mass Spectrometry and Multivariate Analysis. *Fuel* **2001**, *80*, 1689−1696.
(171) Qu, Y.-C.; Wang, Z.; Lu, Q.; Zhang, Y. Selective Production of 4-Vinylphenol by Fast Pyrolysis of Herbaceous Biomass. *Ind. Eng. Chem. Res.* **2013**, *52*, 12771−12776.